Exploration of novel topological lasing modes: their robustness and dynamics

Stephan Wong

A thesis submitted for the degree of

Doctor of Philosophy

School of Physics and Astronomy

Cardiff University

June 2022

Under the supervision of:

- Dr. Sang Soon Oh

- Prof. Anthony Bennett

Abstract

Recently, topological photonics has been proven to be an attractive framework for manipulating the light in an extraordinary way. For instance, photonic topological insulators can exhibit modes that are robust against some defects such as fabrication imperfections, deformations and sharp bendings in waveguides. This thesis extends previous works on topological lasers by proposing new topological lasing modes, analysing the dynamic behaviours of those modes and adopting new topological classification methods with the aim to realise high-performance laser devices. In particular, I will cover some of my recent contributions in the research field, especially on topological edge modes in kagome photonic crystals, semiconductor topological laser cavities, and non-Hermitian topological bulk modes, as well as on a proposed data-driven approach for topological classification in topological insulator lasers. I will start with an all-dielectric reciprocal topological insulator based on the geometry of a kagome lattice, where I demonstrated broadband and highly efficient unidirectional photonic edge mode propagation for sharp bendings conserving the local symmetry. These topological edge modes working at telecommunication wavelengths will be used to construct semiconductor laser cavities insensitive to defects. In the topological cavity, I will show that two different regimes coexist where additional Fabry-Pérot modes are present in addition to the topological lasing modes. Finally, I will show how non-Hermiticity can give rise to new topological states. In particular, I will look at so-called topological bulk modes that arise from asymmetric couplings. In contrast to the topological edge modes, they are delocalised over the bulk while still being topologically protected. The topological bulk modes have been achieved in a two-dimensional kagome lattice, with rhombus geometry, by introducing an imaginary gauge field. I will show the possibility to achieve temporally stable, phase-locked broad area topological lasers in two-dimensional lattices. Further, I will propose a data-driven method in order to find new topological phases via reverse engineering.

Acknowledgements

First and foremost, I would like to express my deepest gratitude to my main supervisor Dr. Sang Soon Oh for giving me the opportunity to pursue a PhD in this exciting research field of topological photonics. I am deeply grateful for his kindness, his help and his guidance throughout my PhD allowing me to pursue various projects and to meet other research groups. I am also thankful to my second supervisor Prof. Anthony Bennett for his insights into the experimental aspect of my work.

I would like to extend my thanks to my colleague Dr. Yongkang Gong for the insightful discussions and for helping me get started on my PhD. I am also thankful to my colleagues Zeeshan Ahmad, Ghada Alharbi, and Dr. Haedong Park for the support and the interesting discussions.

Many thanks also to my colleagues in the Sêr Cymru group for being patient enough for attending my presentations which surely helped me to talk about the theoretical aspect of my research to experimentalists. Special thanks should also go to my PhD colleagues Reza Hekmati, Dominic Kwan, Sam Bishop, Dhafer Alshahrani, Jamal Ahmed and Annie Mathew, for the nice and helpful discussions.

I am also grateful to Prof. Ortwin Hess and Dr. Matthias Saba for the fruitful collaborations and for having me started on this exciting research field of topological photonics. Special thanks should also go to Dr. Matthias Saba for sharing the open PhD position with Dr. Sang Soon Oh. I would also like to thank Prof. Doris Reiter and Jan Olthaus for the projects we did together, for getting me started in machine learning, and for organising my visit stay in Münster. Many thanks should also go to Yeongha Kim, Dr. Changwon Seo, Prof. Teun-Teun Kim and Prof. Gi-Ra Yi for their experimental collaborations.

I am extremely grateful to all my friends and family for supporting and helping me during my PhD journey.

Finally, I would like to thank all the people who read, helped or gave me feedback during the writing process of this thesis.

List of publications

Paper I S. Wong, M. Saba, O. Hess, and S. S. Oh, Gapless unidirectional photonic transport using all-dielectric kagome lattices, Phys. Rev. Res. 2, 012011 (2020).

Paper II M. Saba, S. Wong, M. Elman, S. S. Oh, and O. Hess, Nature of topological protection in photonic spin and valley Hall insulators, Phys. Rev. B 101, 054307 (2020).

Paper III Y. Gong, S. Wong, A. J. Bennett, D. L. Huffaker, and S. S. Oh, Topological insulator laser using valley-Hall photonic crystals, ACS Photonics 7, 2089 (2020).

Paper IV Y. Gong, L. Guo, S. Wong, A. J. Bennett, and S. S. Oh, Tailoring topological edge states with photonic crystal nanobeam cavities, Sci. Rep. 11, 1055 (2021).

Paper V H. Park, S. Wong, X. Zhang, and S. S. Oh, Non-Abelian charged nodal links in a dielectric photonic crystal, ACS Photonics 8, 2746 (2021).

Paper VI S. Wong and S. S. Oh, Topological bulk lasing modes using an imaginary gauge field, Phys. Rev. Res. 3, 033042 (2021).

Paper VII Y. Kim, S. Wong, C. Seo, J. H. Yoon, G. H. Choi, J. Olthaus, D. E. Reiter, J. Kim, P. J. Yoo, T.-T. Kim, S. S. Oh, and G.-R. Yi, Self-assembled honeycomb lattices of dielectric colloidal nanospheres featuring photonic Dirac cones, ACS Appl. Nano Mater. 5, 3386 (2022).

Paper VIII H. Park, S. Wong, A. Bouhon, R.-J. Slager, and S. S. Oh, Phase transitions of non-Abelian charged nodal links in a spring-mass system (accepted for Phys. Rev. B).

Paper IX S. Wong, J. Olthaus, T. K. Bracht, D. E. Reiter, and S. S. Oh, Data-driven classification of topological lasing modes (in preparation).

Paper X J. Olthaus, M. Sohr, S. Wong, S. S. Oh and D. E. Reiter, Modelling spatio-temporal dynamics of chiral coupling of quantum emitters to light fields in nanophotonic structures (in preparation).

My contributions

Here, I outline my contributions to each of the chapters in this thesis. The majority of my research has been done under the supervision of my main supervisor Sang Soon Oh, where I greatly benefit from his knowledge and insights.

Chapter 2 is based on **Paper I**. The kagome lattice used in the project has been originally proposed by Matthias Saba during my master's study with him and Ortwin Hess. The InGaAsP dielectric slab has been suggested by Anthony Bennett. I made the initial draft of the paper and produced all the figures. Besides, I proposed and performed all the calculations and numerical simulations.

Chapter 3 relies on **Paper III**. The main idea has been proposed by Sang Soon Oh and the main investigator was Yongkang Gong. I contributed in all the stages of the project and in the writing of the manuscript. The figures have been produced by Yongkang Gong but have been adapted and modified by me for the thesis. I helped in the core of the project by providing insights into the theory and simulations. In particular, I proposed the design of the cavity with its interior being made of negatively perturbed kagome lattices. I also contributed to the analysis of the band structure and the lasing dynamics. Although most of the simulation has been computed by Yongkang Gong, many of the simulation files have been provided by me and built upon them. This includes, for instance, the implementation of the triangular cavity.

Chapter 4 draws on **Paper VI**. I proposed the core idea of the project. I made the initial draft of the paper and produced all the figures. Moreover, I proposed and performed all the calculations and numerical simulations.

Chapter 5 is derived from **Paper IX** which is still in preparation at the moment of writing this thesis. This project is part of a collaboration with Doris Reiter on using machine learning for the study of topological insulators. I proposed the main idea of the project. In addition, I performed all the simulations and made all the figures.

Introduction

The control of the flow of light has been one of the main goals in photonics in the last decades. Photonic crystals (PhCs) have been a fundamental step toward this goal [1]. Because a PhC consists of periodic dielectric materials, the electromagnetic fields can be written in the Bloch form and one can define photonic band structures and photonic bandgaps, which tell us whether an incident wave can couple to a bulk mode or decays exponentially inside the PhCs. Thanks to crystal symmetry, one only needs to look at the first Brillouin zone to gain all the relevant information. PhCs are used for many applications ranging from simple filters to complex cavity structures for the integration of single-photon emitters on a chip [1]. However, inherent in every optical device and waveguide are the problem of back-reflection of the light propagation because of bendings, fabrication defects or environmental variations.

Pioneered by the seminal work by Raghu and Haldane [2], photonic topological insulators (PTIs) extend the notion of topological insulators (TIs) from condensed matter physics to photonic systems. One of the remarkable features of (photonic) topological insulators is the existence of robust topological edge modes at the interface between two topologically inequivalent (photonic) crystals. This is known as the bulk-edge correspondence. The robustness of the topological edge modes can be seen, for example, as an edge mode that propagates only in one direction without being back-reflected in presence of bendings or defects preserving the symmetries of the system [3, 4]. Photonic systems are topologically distinct if they are characterised by different topological invariants. Depending on the symmetry of the system, the "ten-fold way" classifies the topological insulators and gives access to a periodic table of topological invariants [5]. For example, such topological invariants are the

winding number and the Chern number which are mainly calculated from the Bloch eigenstates and the band structure.

A natural platform for PTIs is PhCs because of the possible extension of topological band theory to photonic band structures. Implementations of PTIs vary considerably and several schemes have been developed. For example, the photonic analogue of a quantum Hall topological insulator was first achieved in the microwave regime using gyromagnetic materials with a strong magnetic field applied to break the time-reversal symmetry [6]. Later, several proposals have been put forward to realise photonic topological transport free of external magnetic fields by temporal modulation of photonic crystals to mimic time-reversal-symmetry breaking [7–10]. A subwavelength-scale PTI approach via pseudo-time-reversal symmetry in all-dielectric photonic crystals was recently proposed [11] and experimentally verified from visible wavelengths to microwave regime [12–16]. Another elegant subwavelength-scale nontrivial topology strategy has been introduced by exploiting the optical valley Hall effect to break spatial-inversion symmetry to access the opposite Berry curvature near Brillouin zone corners [17–26]. This opens avenues to on-chip photonic devices for robust topologically protected light manipulation.

Extension of PTIs to non-Hermitian systems, especially to active systems, has recently gained attention due to the inherent loss of photonic systems, but also because of its promise to enhance laser device performances. Because of the non-Hermiticity of the system, the bulk-edge correspondence breaks down in some cases [27]. Therefore one needs to extend the ten-fold way to capture the non-Hermiticity and construct new topological invariants [28–30]. The first topological laser was realised experimentally using magneto-optical photonic crystals with an applied static magnetic field to break time-reversal symmetry [31]. The non-Hermitian, parity-time ($\mathcal{PT}$) symmetric, one-dimensional (1D) Su-Schrieffer-Heeger (SSH) model [32] has been studied to generate edge states and topological lasing devices [33–35]. A cavity made of topological distinct PTIs has been proposed to enhance the lasing efficiency by using the unidirectional topologically protected edge-mode lasing [31, 36, 37]. Moreover, a topological laser has been proposed by using extended topological modes to achieve broad-area emission in a two-dimensional (2D) hexagonal

cavity [38] based solely on the parity symmetry of the mode at the Γ-point or by using an imaginary gauge field in a 1D $\mathcal{PT}$-symmetric SSH lattice to delocalise the zero-energy boundary mode over the 1D-bulk [39].

However, the focus has been mainly on addressing the question of the spatial stability of those topologically protected modes, *i.e.* on the existence of topologically protected modes coming from (active) non-Hermitian PTIs. Non-linearity being intrinsic in active systems, studying the non-linear dynamics of active non-Hermitian PTIs seems to be a more natural framework and may lead to the discovery of richer physics [40, 41]. More than just a natural framework, temporal stability is an important characteristic since non-linear effect may give unstable or chaotic behaviours of the topologically protected modes [42] even though its frequency analysis may guarantee its spatial stability, *i.e.* no back-scattering at sharp edges and robustness against disorder. To fully understand the stability of topological modes, both spatial and temporal stabilities are required based on a frequency analysis and non-linear dynamic analysis. Nevertheless, standard linear stability analysis can be quite challenging [42] because of the high-dimensional phase and parameter space.

On the other hand, machine learning (ML) has been a fruitful tool in attacking complex problem directly. ML is a data-driven approach and has been proven successful for classification, or dimensionality reduction tasks of large sets of high-dimensional data. For example, the data-driven method has been used to draw topological phase diagrams [43], calculate topological invariants [44], or explore topological band structures [45]. In the field of PTIs, ML may be useful in attacking complex systems with a huge parameter space when analytical computation becomes difficult to handle. In particular, this can be used to study spatio-temporal dynamics and can provide new insight into the fundamental physics.

This thesis aims at designing topological insulator lasers which present clear advantages for lasing application compared to standard lasers. We explore the idea of using active materials on passive photonic topological insulators to have topological insulator lasers. The focus is made on designs that are simple enough to fabricate and compatible with current semiconductor

photonic integrated circuit technologies for an easy integration into other passive or active photonic devices. Moreover, the effect of non-Hermiticty in the system is also explored in order to take advantage of unique behaviours that do not exist in Hermitian systems.

To this end, we demonstrate in Chap. 2 the presence of topologically protected modes in waveguides made of opposite geometrically perturbed kagome lattices. These valley-dependent edge states, that emulate the optical valley Hall effect, exhibit broadband suppressed reflection in the presence of sharp corners and further show negligible vertical losses. In contrast to proposed PTI designs that require complicated structures or very strong magnetic fields, the proposed kagome lattice offers a simple all-dielectric nanophotonic strategy to achieve topological edge modes. Using conventional semiconductor device examples, we propose a realistic device composed of an InGaAsP free-standing photonic crystal working at telecommunication wavelengths. In Chap.3, we employ the topological waveguide obtained in Chap.2 to design an all-dielectric topological insulator laser working in the telecommunication region based on semiconductor cavities formed by topologically distinct kagome photonic crystals. The simplicity of the proposed PTI laser and the low vertical loss of the edge mode utilised for lasing present clear advantages compared to PTI lasers proposed in the literature. An interesting feature of the kagome lattice is that it supports two different types of valley Hall edge modes, which enables the coexistence of topological ring-resonator modes and trivial Fabry–Pérot resonator modes in the proposed topological cavities. The pumping and lasing dynamics of the topological cavities are studied by means of a four-level two-electron model and demonstrate that this model offers a powerful platform to investigate topological laser cavities with arbitrary geometry. On the other hand, Chapter 4 reports exciting results about a novel topological phase in non-Hermitian photonic topological insulator lasers. Here we propose a procedure to realise topologically protected modes extended over a d-dimensional bulk by introducing an imaginary gauge field. This generalises the idea of zero-energy extended modes in the one-dimensional SSH lattice into higher dimensional lattices allowing a d-dimensional bulk mode that is topologically protected. Furthermore, we numerically demonstrate, using an optical gain

modelled by a two-level model, that the topological bulk lasing mode can facilitate high temporal stability superior to topological edge mode lasers. Using an exemplified topological extended mode in the kagome lattice made of active ring resonators, we show that large regions of stability exist in its parameter space. Finally, we propose in Chap. 5 a data-driven method to draw the phase diagram in topological insulator lasers. The classification is based on the temporal behaviour of the topological mode obtained via numerical integration of the rate equation. A semi-supervised learning method is used and an adaptive library is constructed in order to distinguish the different topological modes present in the generated parameter space. The proposed method has been proven successful in distinguishing the different topological phases in the SSH lattice with saturable gain and is promising for consideration of more complicated laser models or systems. This demonstrates the possibility to classify the topological phases without the need for expert knowledge of the system and may give some insight into the fundamental physics of topological insulator lasers via reverse engineering.

Acronyms

$\mathcal{PT}$ Parity-time.

1D One-dimensional.

2D Two-dimensional.

3D Three-dimensional.

BZ Brillouin zone.

DFT Discrete Fourier transform.

DMD Dynamical mode decomposition.

FDTD Finite-difference time-domain.

FFT Fast Fourier transform.

FP Fabry-Pérot.

FSR Free-spectral-range.

KVP Kagome valley-Hall photonic.

MEEP *MIT Electromagnetic Equation Propagation*.

ML Machine learning.

MPB *MIT Photonic Bands*.

OBC Open boundary condition.

PBC Periodic boundary condition.

PCA Principal component analysis.

PhC Photonic crystal.

PML Perfect matching layer.

POD Proper orthogonal decomposition.

PTI Photonic topological insulator.

QSHE Quantum spin Hall effect.

QVHE Quantum valley Hall effect.

SOI Silicon-on-insulator.

SSH Su-Schrieffer-Heeger.

SVD Singular value decomposition.

TB Tight-binding.

TE Transverse electric.

TI Topological insulator.

TM Transverse magnetic.

TMM Transfer matrix method.

Contents

Chapter 1

Theoretical background

At the core of (photonic) topological insulators are the bulk-boundary correspondence and the calculation of topological invariants [5,46–49]. This guarantees the spatial stability of the obtained topologically protected modes, namely its robustness against a certain class of defects. However, the temporal stability of those topologically protected modes may not be guaranteed in active non-Hermitian topological insulators. Non-linearity being intrinsic to active systems, this can give rise to temporal instabilities [42] but also to novel topological phases [40, 41].

This preliminary chapter will be dedicated to introducing the main concepts used throughout the thesis while focusing on the aspects that are relevant to the content of the thesis. We will start with a brief introduction to what a topological insulator is, focusing mainly on gapped topological insulators. As a toy model, we will study the SSH lattice in order to familiarise us with the main concepts used in the thesis. This includes the calculation of a topological invariant that does not change under continuous deformations as long as the gap remains open, and the bulk-boundary correspondence which accompanies a change of topological invariant across some interface. In the next section, we will look at how non-Hermiticity, in particular gain, can be introduced into the Hermitian SSH lattice and consider a gain and loss distribution that satisfies the well-known $\mathcal{PT}$ symmetry. The active system is then studied in the frequency domain in order to see the change of spectrum and thus possible topological phase change, as well as in the time domain to explore the

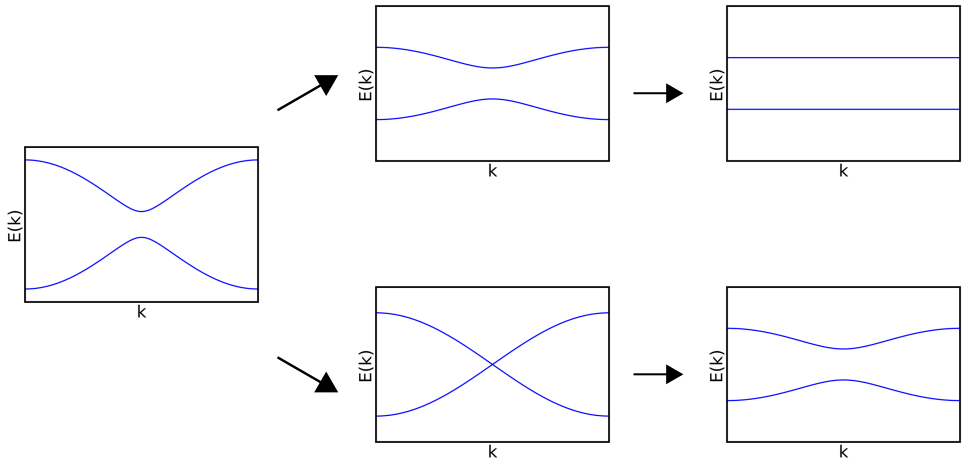

Figure 1.1: Example of continuous (top) and discontinuous (bottom) deformation for the example of a two-band model.

dynamics of the topological mode in the active system.

1.1 Topological insulator: The SSH lattice

TIs have attracted a lot of attention due to their remarkable feature of having topologically protected edge states that are robust against symmetry-preserving disorder. This remarkable feature of TIs relies on topological invariants which are quantities that do not change under continuous deformations. Physically, a continuous deformation can be seen as a parametrisation of, say, a two-band model that deforms the bands without closing the present gap as illustrated in Fig. 1.1(top). On the other hand, a discontinuous deformation is shown in Fig. 1.1(bottom) and is characterised by a gap closing in the deformation process. Systems having different topological invariants are said to belong to different topological phases. An interesting aspect of TIs appears when we have a system composed of two topologically distinct phases that are interfacing with each other. The topological invariant must therefore change at the interface between the topologically distinct systems via some band gap closing and gives rise to the presence of edge states that are topologically protected. This is known as the bulk-edge (or bulk-boundary) correspondence: one can infer information at the edge of a sample from solely the bulk information via the calculation of topological invariants. Importantly, these topological modes feature robust behaviour for local perturbation disorders at

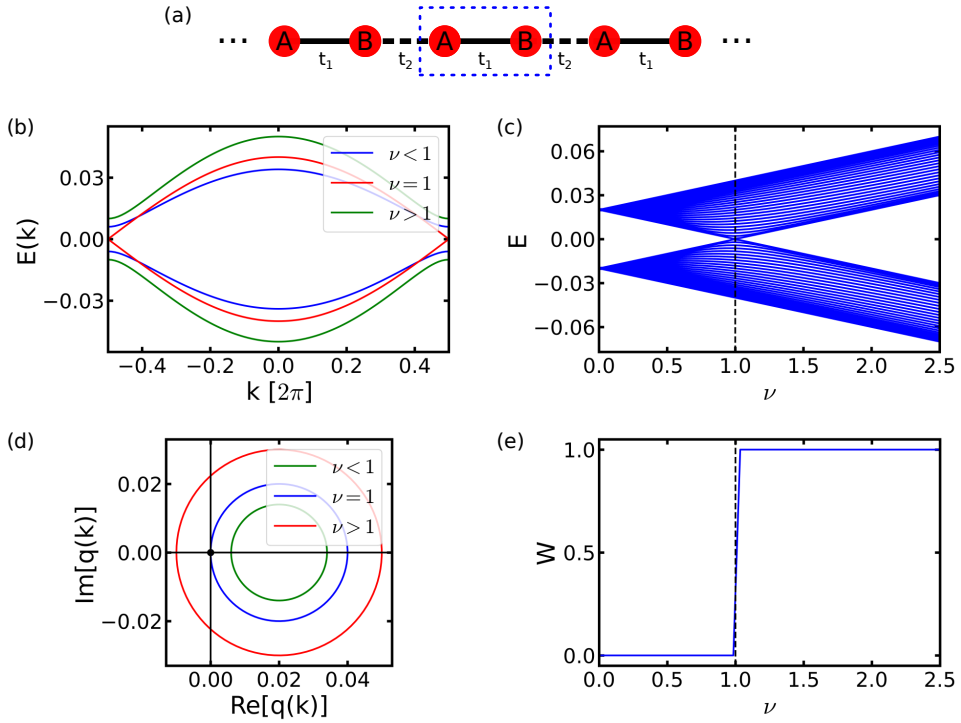

Figure 1.2: (a) Schematic of the SSH lattice with intra- and inter-unit cell couplings t_1 and t_2, respectively. The unit cell is composed of two sites A and B, and is represented by the blue dotted box. (b) Band structure of the SSH lattice with different couplings strength ratio: $\nu < 1$, $\nu = 1$ and $\nu > 1$. (c) Projected band structure against the coupling strength ratio ν. (d) Evolution of $q(k)$ in the complex plane, with respect to the wave vector k, for $\nu < 1$, $\nu = 1$ and $\nu > 1$. (e) Winding number W against the coupling ratio ν. The coupling parameters are $t_1 = 0.02$ for all the panels, and $\nu = 0.7, 1, 1.5$ in (a),(c).

the interface since the origin of these modes comes from the bulk of the system.

As a first example of TI, we will consider the SSH lattice in order to illustrate the notion of topological invariants and the bulk-edge correspondence.

1.1.1 Bulk analysis

The SSH lattice is characterised by a one-dimensional lattice with two sites per unit cell, A and B, and with intra- and inter-unit cell coupling t_1 and t_2 respectively, as depicted in Fig. 1.2(a).

Using a tight-binding formalism with the nearest neighbour approximation,

the evolution of the state ψ of the SSH lattice is governed by:

$$i\frac{d\psi}{dt} = H_{\mathrm{SSH}}\psi \tag{1.1}$$

where H_{SSH} is the Hamiltonian that describes the couplings between the sites in the tight binding formalism. Explicitly, we have $\psi = (\ldots, a_n, b_n, \ldots)^T$ and the coupled-mode equations [Eq. 1.1] read:

$$i\frac{da_n}{dt} = E_A a_n + t_1 b_n + t_2 b_{n-1}, \tag{1.2}$$

$$i\frac{db_n}{dt} = E_B b_n + t_1 a_n + t_2 a_{n+1}, \tag{1.3}$$

where a_n and b_n are the amplitudes of the sites A and B, respectively, on the n-th unit cell, and E_σ the on-site energy on the site σ. Thanks to translation symmetry, the Bloch Hamiltonian in momentum space can be obtained, from the Fourier transform of Eqs. 1.2 and 1.3:

$$H_{\mathrm{SSH}}(k) = \begin{pmatrix} E_A & t_1 + t_2 e^{-ik} \\ t_1 + t_2 e^{ik} & E_B \end{pmatrix}. \tag{1.4}$$

Provided $E_A = E_B = 0$, the eigenvalues of $H_{\mathrm{SSH}}(k)$ are given by $E(k) = \pm|q(k)|$, where $q(k) := t_1 + t_2 e^{-ik}$. Depending on the coupling strength ratio $\nu := t_2/t_1$, the spectrum of the SSH lattice is either gapped or gapless and thus is in an insulating or metallic phase, respectively. Figure 1.2(b) shows the bandstructure $E(k)$ obtained for three different coupling strengths: $\nu < 1$, $\nu = 1$ and $\nu > 1$. Interestingly, by sweeping the coupling strength ratio, the gap closes at the particular point $\nu = 1$ ($t_2 = t_1$)[1] , whereas the spectrum is gapped whenever $\nu \neq 1$ ($t_2 \neq t_1$) as plotted in Fig. 1.2(c). The degenerate configuration $\nu = 1$ is the critical configuration where a topological phase transition can occur, *i.e.* where the topological invariants can change as we will see in the next section.

Topological band theory allows us to classify the bands according to their

[1] For simplicity, only positive couplings are considered in this example. Otherwise, the spectrum is gapless (gapped) whenever $|\nu| = 1$ ($|\nu| \neq 1$).

corresponding topological invariant [5, 46–49]. Which topological invariant to use depends on the symmetry of the system [5]. Here we are interested in the case where $E_A = E_B = 0$ in which chiral symmetry is satisfied, $CH(k)C = -H(k)$ with $C = \sigma_z$, and from which the winding number can be used as a topological invariant.

Intuitively, the winding number W can be found by looking at the evolution of $q(k)$ with respect to the wave vector k in the first Brillouin zone (BZ). Figure 1.2(d) shows the evolution of $q(k)$ in the complex plane for three configurations: $\nu < 1$, $\nu = 1$ and $\nu > 1$ as in Fig. 1.2(b). In the complex plane, the origin $|q| = 0$ corresponds to the degenerate point. We observe that $q(k)$ does not encircle the origin for $\nu < 1$, whereas $q(k)$ winds around the origin once for $\nu > 1$. The winding number W is then the number of times $q(k)$ winds around the origin. The topological origin of this winding number can be demonstrated via homotopy theory where, for example, a loop that winds around the origin once cannot be deformed from the configuration $\nu > 1$ to $\nu < 1$ without closing the bandgap at $\nu = 1$.

Rigorously, the winding number W can be calculated directly from the bulk Hamiltonian. In the basis of the chiral symmetry operator, $H_{\mathrm{SSH}}(k)$ is off-diagonal:

$$H_{\mathrm{SSH}}(k) = \begin{pmatrix} 0 & q(k) \\ q^*(k) & 0 \end{pmatrix} \tag{1.5}$$

and the winding number W is given by:

$$W = \frac{1}{2\pi i} \int_{-\pi}^{\pi} dk \frac{d}{dk} \ln(q(k)). \tag{1.6}$$

We can see in Fig. 1.2(e) that the winding number is $W = 0$ for $\nu < 1$ and $W = 1$ for $\nu > 1$. Therefore we can say the SSH lattices with $\nu < 1$ and $\nu > 1$ are topologically distinct. Consistent with the explanation given above, the winding number changes only when a gap closes. This is an example showing the topological invariant remains unchanged as long as there is no gap closing.

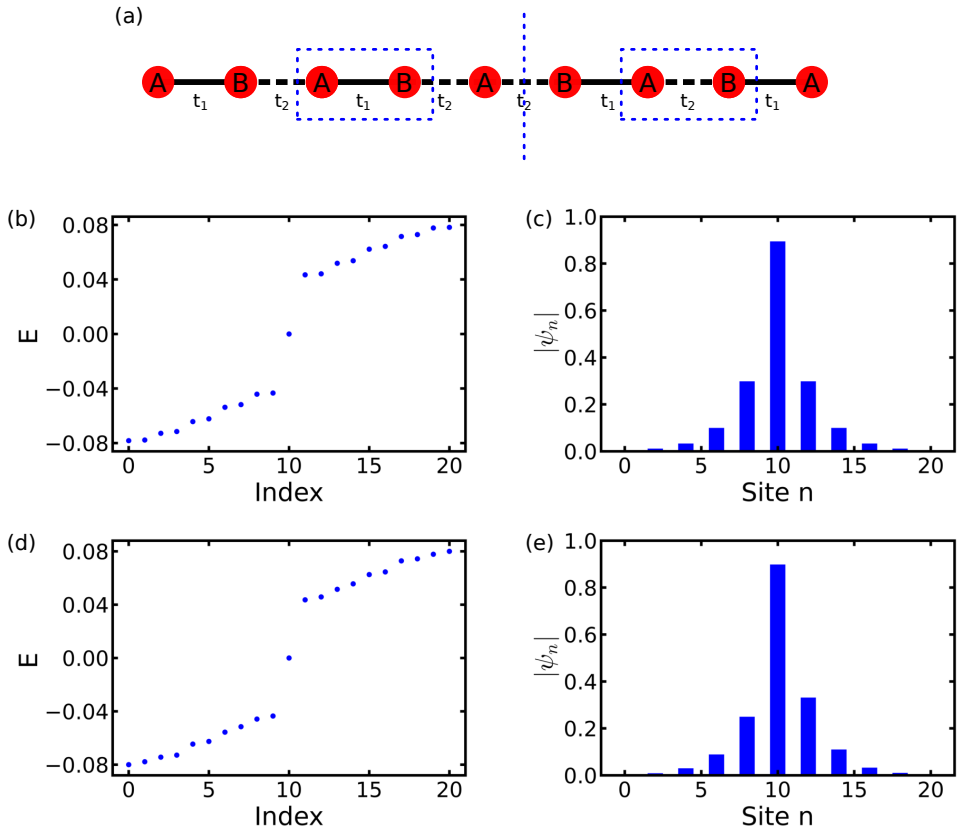

Figure 1.3: (a) Schematic of the lattice with a domain wall composed of SSH lattices . On the left (right) side of the domain wall, we have $\nu < 1$ ($\nu > 1$). (b) Spectrum of the lattice in (a). (c) Field profile of the zero-energy mode in (b). (d),(e) Spectrum of the lattice and field profile of the zero-energy mode in presence of perturbations in coupling strength. The couplings are perturbed by a random uniform distribution $\delta t_i \in [-0.005, 0.005]$. The lattice is made of $N_s = 21$ sites. The coupling parameters for the left (right) side of the interface are $t_1 = 0.06$ and $\nu = 1/3$ ($t_1 = 0.02$ and $\nu = 3$).

1.1.2 Boundary analysis

So far in this section, we have analysed the SSH lattice with periodic boundary conditions (PBCs). It turns out that interesting physics happens once boundaries are considered on the lattice.

In particular, one can consider the boundary between two topologically distinct SSH lattices, *i.e.* between an SSH lattice with $\nu < 1$ on one side, and $\nu > 1$ on the other side as illustrated in Fig. 1.3(a). This lattice configuration, therefore, creates a domain wall between topologically distinct SSH lattices. Knowing that the SSH lattice with $\nu < 1$ and $\nu > 1$ have different topological

invariants, it is expected, from the bulk-edge correspondence, to have topological edge states that arise at the interface between the two lattices. Because of chiral symmetry, there is necessarily a zero-energy mode when considering an odd number of sites[2] . This zero-energy mode corresponds to the topological edge mode. Figures 1.3(b) and 1.3(c) indeed show the zero-energy mode present in the spectrum of the lattice and the field profile of the topological zero-energy mode that is exponentially decaying away from the boundary interface. This edge mode is topologically protected, namely, it is robust against perturbations as long as the perturbations do not break chiral symmetry or close the bandgap. This is demonstrated in Figs. 1.3(d) and 1.3(e) where the spectrum of the lattice with perturbations in the couplings is plotted, as well as the field profile of the corresponding zero-energy mode of the lattice. The zero-energy mode and the topological mode remain present even though we have perturbations in the couplings.

An alternative analysis to study topological insulators can be realised from the study of the continuum Dirac Hamiltonian of the system. The interface states are efficiently captured by the Hamiltonian of a single gapped Dirac cone with mass M on one side of the interface, and mass $-M$ on the other side. The Dirac Hamiltonian of the SSH lattice can be obtained by Taylor expanding the Bloch Hamiltonian around its band extrema, here $k_0 = \pi$:

$$H(k_0 + \delta k) \approx M\sigma_x - t_2 \delta k \sigma_y \tag{1.7}$$

where $|\delta k| \ll 2\pi$ is assumed to be small, and $M = t_1 - t_2$ is the mass term that opens a bandgap. The system with a domain wall is given by a mass term that changes signs over the interface. For example, we can consider the following interface:

$$M(x) = \begin{cases} M_0 & \text{if } x \geq 0 \\ -M_0 & \text{if } x < 0 \end{cases}, \tag{1.8}$$

where $M_0 = t_1 - t_2$ for fixed t_1 and t_2. Therefore the interface between

[2] When an odd number of sites is considered, chiral symmetry constrains the eigen-energies to come in pairs, *i.e.* to have energies E and $-E$. Therefore for an odd number of sites, the zero-energy mode $E = 0$ is necessarily present. On the other hand, for an even number of sites, the zero-energy mode split into two energy modes exponentially close to $E = 0$.

two topologically distinct phases happens, here, at $x = 0$. The continuum Hamiltonian is then obtained by replacing the wave vector δk with $-i\partial_x$ since there is no translation symmetry along the x-direction anymore. The localised state $\varphi(x)$ with energy E at the interface is obtained by solving:

$$H_{\text{continuum}}\varphi(x) = E\varphi(x) \tag{1.9}$$

Starting with the ansatz of the boundary state on the left and right side of the interface written as:

$$\varphi(x) = \begin{pmatrix} a_i \\ b_i \end{pmatrix} e^{\pm\kappa x} \tag{1.10}$$

where κ is the penetration depth, we can show that the solution to Eq. 1.9 is given by $E = 0$ with $a_i = 0$, $b_i = 1$ and $\kappa = M_0/t_2$. More generally, one can show that an edge state with energy $E = 0$ exists as long as the mass term changes sign at the interface, independently of the interface details $M(x)$, and is given by:

$$\varphi(x) = \begin{pmatrix} 0 \\ 1 \end{pmatrix} Ce^{-\frac{1}{t_2}\int_0^x dx' M(x')}, \tag{1.11}$$

where C is a constant scalar.

As another type of boundary in the lattice, it is also interesting to look at the finite-size SSH lattice with an odd number of sites as illustrated in Fig. 1.4(a). This finite size system corresponds to the system with open boundary conditions (OBCs). We find the presence of a single zero-energy mode and that a change in the bulk topological invariant is accompanied by a change in the localisation of the zero-energy mode: this is another example of the bulk-edge correspondence. This topological transition point is again characterised by a bulk band touching. Figure 1.4(b) shows the spectrum of the SSH lattice with an odd number of sites and demonstrates the presence of the zero-energy mode. A similar spectrum can be obtained whether $\nu < 1$ or $\nu > 1$. However, as expected from the Bloch Hamiltonian, we observe in Fig. 1.4(c) that the gap closes when $\nu = 1$ and remains open as long as $\nu \neq 1$.

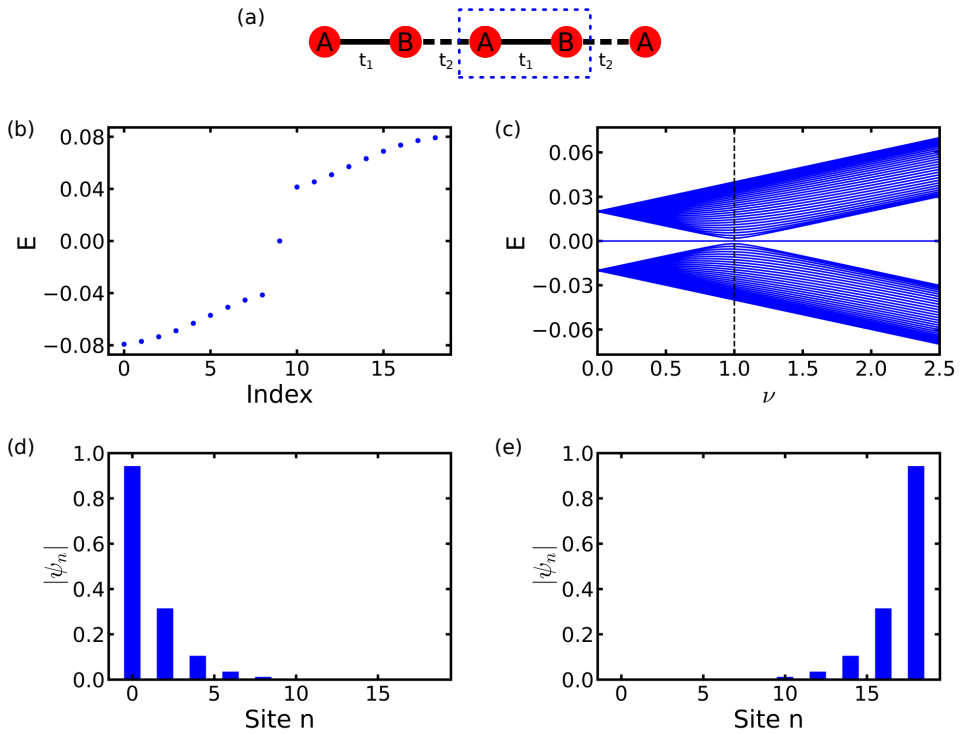

Figure 1.4: (a) Schematic of a finite-size SSH lattice with broken unit cell. Here the lattice starts and ends with an A site. (b) Spectrum of the lattice in (a). (c) Projected energy spectrum against the coupling ratio ν. (d),(e) Field profile of the zero-energy mode of a finite-size SSH lattice with $\nu > 1$ and $\nu < 1$, respectively. The lattice is made of $N_s = 19$ sites in (a),(d),(e) and $N_s = 67$ sites in (c). The coupling parameters for panel (d) and (e) are $t_1 = 0.02$ with $\nu = 3$ and $t_1 = 0.06$ with $\nu = 1/3$, respectively.

As shown in the previous section, the topological transition at $\nu = 1$ is accompanied by a change in the winding number defined for the bulk (with PBCs). Along with the change of the winding number, Figs. 1.4(d) and 1.4(e) show that the topological mode is localised either on the left for $W = 0$ ($\nu < 1$) or on the right for $W = 1$ ($\nu < 1$) of the lattice.

1.2 Topological insulator laser: The $\mathcal{PT}$-symmetric SSH lattice

Extension of TIs to non-Hermitian and non-linear systems has been studied recently due to its possibility to have richer physics and new topological phases that have no counterpart in the Hermitian setting [28, 40, 41]. In particular, for PTIs, a lot of attention has been drawn to introducing gain and loss into

the system in order to have topological insulator lasers that show better laser performances [31, 36, 37].

In this section, we will introduce gain and loss into the previous finite-size Hermitian SSH lattice [Fig. 1.4], with $\nu > 1$ as the coupling configuration. We will especially focus on using the topologically protected mode obtained in the Hermitian setting to have a topologically lasing mode. As a physical system for the active material, we here consider an array of active ring resonators coupled through their overlapping evanescent fields [50–52].

For a mode to lase, one would favour a strong overlap of the mode with the gain. By looking at the field profile of the zero-energy mode of the Hermitian SSH lattice, we can see in Fig. 1.4(d) that the mode has non-vanishing amplitudes only on the A sites. One would therefore expect this mode to lase if we put gain on the A sites, and loss on the B sites so that the remaining modes will vanish over time. This configuration of gain and loss is known as the $\mathcal{PT}$-symmetry configuration. In the following, we will study the $\mathcal{PT}$-symmetric SSH lattice[3]. In particular, we will tackle the problem using both a frequency-domain approach and a time-domain approach.

1.2.1 Frequency-domain analysis

The gain and loss can be modelled in the tight-binding formalism by means of an imaginary on-site energy, namely by setting $E_\sigma = ig_\sigma$ where g_σ is the gain (loss) term in the site σ if $g_\sigma > 0$ ($g_\sigma < 0$). Therefore, the coupled-mode equations read:

$$i\frac{da_n}{dt} = ig_A a_n + t_1 b_n + t_2 b_{n-1}, \tag{1.12}$$

$$i\frac{db_n}{dt} = ig_B b_n + t_1 a_n + t_2 a_{n+1}. \tag{1.13}$$

[3] Although it is not rigorously correct, the wording "$\mathcal{PT}$-symmetric" will be used in the remainder of this chapter to describe this particular gain/loss configuration on the A/B sites. In fact, $\mathcal{PT}$-symmetry is only realised in the infinite lattice, for example in the SSH lattice with PBCs.

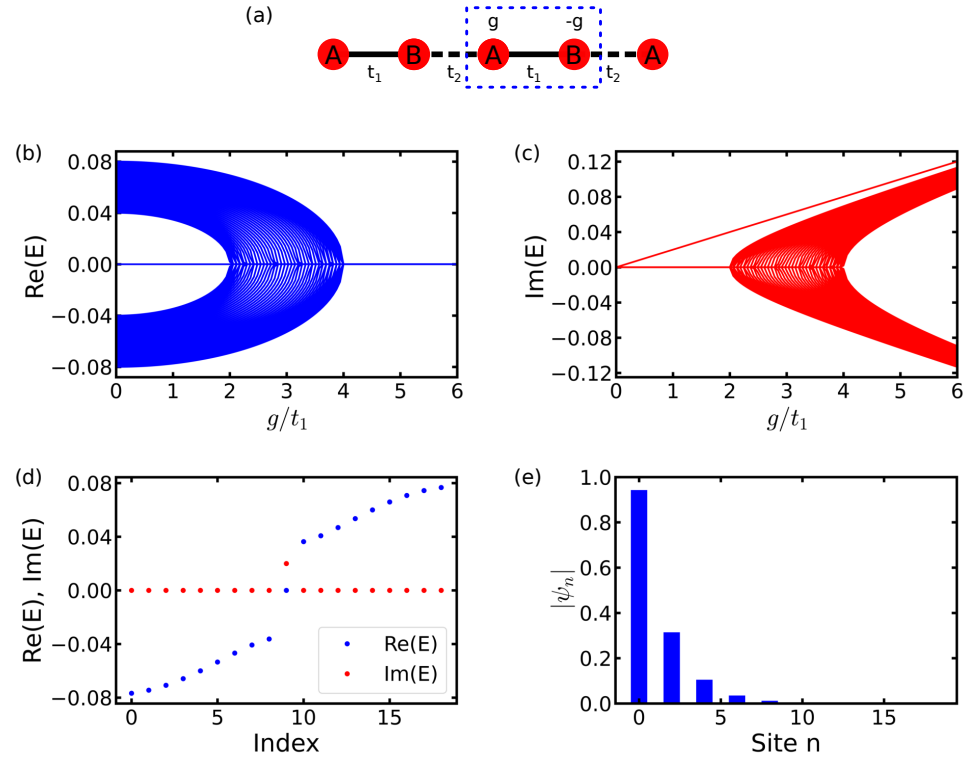

Figure 1.5: (a) Schematic of an active finite-size SSH lattice with broken unit cell in the $\mathcal{PT}$-symmetric configuration. Here the lattice starts and ends with an A site. (b),(c) Real and imaginary parts of the projected energy spectrum of the lattice in (a) against g/t_1, respectively. (d) Real and imaginary parts of the spectrum of the lattice presented in (a) for $g/t_1 = 1$. (e) Field profile of the zero-energy mode from the spectrum in (d). The lattice is made of $N_s = 115$ sites in(b),(c) and $N_s = 19$ sites in (d),(e). The coupling parameters are $t_1 = 0.02$ and $\nu = 3$.

Adding gain and loss in a $\mathcal{PT}$-symmetric way can be realised if

$$g_A = g, \tag{1.14}$$

$$g_B = -g, \tag{1.15}$$

where g is the linear gain [Fig. 1.5(a)]. The spectrum obtained from the $\mathcal{PT}$-symmetric SSH lattice with $g/t_1 = 1$ is plotted in Fig. 1.5(d). The plot reveals that only the zero-energy mode has a non-zero positive imaginary part, while the real part of the spectrum did not change. This demonstrates that the topological zero-energy mode survives after the introduction of non-Hermiticity, here gain and loss: this is the topological lasing mode. In this ring resonator system, the zero-energy $E = 0$ corresponds to the resonant frequency of the

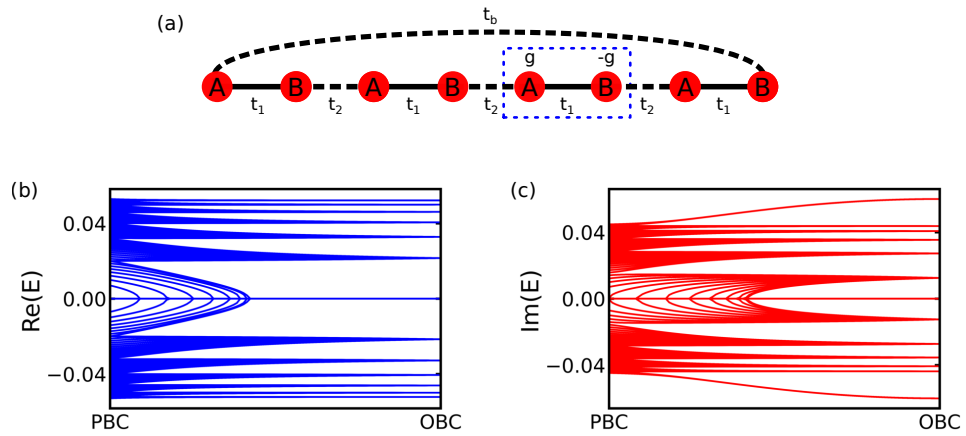

Figure 1.6: (a) Schematic of a finite-size SSH lattice with a non-broken unit cell with periodic boundary conditions and with the inter-unit cell boundary coupling t_b that couples the left and right edge of the lattice. (b),(c) Evolution of the real and imaginary parts of the projected energy spectrum of the lattice in (a) from periodic ($t_b = t_2$) to open ($t_b = 0$) boundary conditions. The lattice is made of $N_s = 24$ sites. The coupling parameters are $t_1 = 0.02$, $\nu = 3$ and $g/t_1 = 3$.

individual ring resonators.

However, one needs to be careful in calculating the topological invariant in the non-Hermitian systems [27]. Indeed, if we look at the system with PBCs and gradually switch off the boundary coupling t_b to end up with a lattice with OBCs as illustrated in Fig. 1.6(a), then we can see in Figs. 1.6(b) and 1.6(c) that the gap closes along the way from PBCs to OBCs. This gap closing is a typical feature in non-Hermitian systems: when going from periodic to open boundary conditions, several exceptional points must be passed through and the topology of the bands has been changed [27].

It is therefore advantageous to work directly in the open boundary conditions in non-Hermitian systems. Indeed, for a finite-size SSH lattice starting and terminating in site A, we observe in Figs. 1.5(b) and 1.5(c) that if we start from the passive system ($g = 0$) and gradually increase the gain and loss, then the spectrum does not have a bandgap closing in the process, at least up to the gain chosen in Figs. 1.5(d) and 1.5(e) ($g = t_1$). Therefore, the topological protection of the zero-energy mode remains. Interestingly is that several gap closing occurs when increasing further the gain and loss strength,

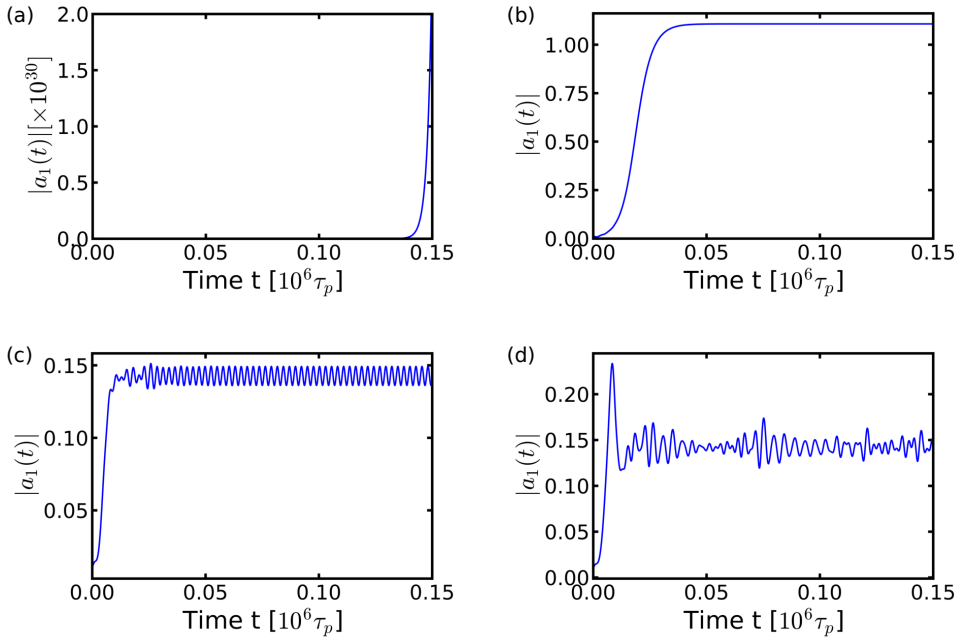

Figure 1.7: Time evolution of the first A site $|a_1(t)|$ where the gain is modelled using: (a) a linear gain ($g/t_1 = 1$) (b) a saturable gain ($g/t_1 = 1$, $\gamma_A = 0.01$) (c) the laser rate equation with $\tau_s/\tau_p = 0.2$ (class-A) (d) the laser rate equation with $\tau_s/\tau_p = 100$ (class-B) The lattice is made of $N_s = 19$ sites. The coupling parameters are $t_1 = 0.02$ and $\nu = 3$. The parameters for the linear and saturable gain are $g/t_1 = 1$ and $\gamma_A = 0.01$. The gain parameters for the laser rate equation are $\alpha_{\mathrm{H}} = 3$, $g_B = 0.02$, $p_A/t_1 = 1$, $\tau_p = 40\,\mathrm{ps}$, and $\tau_s/\tau_p = 0.2$ and $\tau_s/\tau_p = 100$ for the class-A and class-B laser, respectively.

and thus some topological changes happen. Figures 1.5(b) and 1.5(c) show that from low to high gain and loss strength g, the spectrum undergoes several gap closings via exceptional points. The system undergoes several mode splitting from the imaginary part of the spectrum: the extended (bulky) mode starts to acquire an imaginary on-site frequency until all of them have a non-zero imaginary part in energy, *i.e.* until all the of the modes start to lase. This is consistent with Ref. [34], from which the first gap closing happens at $g/t_1 = \nu - 1$, and the gap closings continue until $g/t_1 = \nu + 1$.

1.2.2 Time-domain analysis

The previous section focused on the frequency analysis. However, for lasing applications, it is also important to look at the temporal behaviour of the topological mode, especially when non-linear terms are considered.

Considering linear gain as in the previous section, Fig. 1.7(a) plots the time

evolution of the absolute value of the amplitude of the first A site, $|a_1(t)|$. As one would expect, this demonstrates the gain in the A sites makes the amplitude of the modes grow exponentially over time to reach an extremely high value. This is not physical and requires a finer description of the gain.

A common model for gain is to include a saturable term so that the mode does not grow exponentially. This reads as:

$$g_A(a_n) = \frac{g}{1 + 2|a_n|^2} - \gamma_A, \tag{1.16}$$

$$g_B = -g, \tag{1.17}$$

where g is the linear gain or loss strength, γ_A is the linear loss on the A sites. For simplicity, we have changed the linear gain on the A sites to a saturable gain, while keeping the linear loss on the B sites. The gain is now a local quantity and depends on the intensity in each A sites, $|a_n|^2$. Figure 1.7(b) shows the time evolution of $|a_1(t)|$ when using a saturable gain. The lasing mode is now converging and it reaches, for the parameter chosen, a steady-state corresponding to the topological lasing mode. Importantly, here the dynamics may have completely different behaviour depending on the parameter chosen for the system, as studied in Ref. [40, 41].

Finally, the laser rate equation can also be considered by modelling the gain using a two-level system. This includes the dynamics of the carrier densities in the semiconductor laser as well as the dynamics of the induced polarisation given by the dipole moment in the two-level system. The introduction of the carrier and polarisation dynamics into the rate equation can be realised within the semi-classical laser theory [53], where the medium response is governed by the induced polarisation of the optical field. However, in most semiconductor lasers the dynamics of the polarisation can be neglected and thus be adiabatically removed from the equations. Recalling that our system is made of an array of coupled active ring resonators, the evolution of the mode amplitudes (a_n, b_n) in the rings and the population (Z_n) in the gain ring in the A sites is governed by:

$$i\frac{da_n}{dt} = i\frac{1}{2}\left(g(Z_n) - \frac{1}{\tau_p}\right)(1 - i\alpha_{\mathrm{H}})a_n + t_1 b_n + t_2 b_{n-1}, \tag{1.18}$$

$$i\frac{db_n}{dt} = -ig_B b_n + t_1 a_n + t_2 a_{n-1}, \tag{1.19}$$

$$\frac{dZ_n}{dt} = p_A - \frac{Z_n}{\tau_s} - g(Z_n)|a_n|^2, \tag{1.20}$$

where $g(Z_n)$ is the carrier-density-dependent dynamical gain, τ_p and τ_s are the photon and carrier lifetime, respectively, p_A is pump rate and $\alpha_{\rm H}$ is the linewidth-enhancement factor in semiconductor lasers that takes into account the dependence of the refractive index on the carrier density [54]. Again, for simplicity, the carrier dynamics are only considered on the gain sites (A sites). In the absence of couplings, each ring resonator operates in a single longitudinal and transverse mode, and is assumed to be the same for all the rings. The convention[4] used here for the electric field a_n, b_n of the guided modes in the ring resonators is taken as $a_n \propto e^{-i\omega t}$, where ω is the oscillating (angular) frequency of the modes, and is equivalent to the eigen-energies of the tight-binding Hamiltonian. For laser operations not too far from the lasing threshold in the individual rings, we have:

$$g(Z_n) = g(Z_{\rm th}) + \sigma(Z_n - Z_{\rm th}) \tag{1.21}$$

where $\sigma = \partial g/\partial Z$ is the differential gain, $g(Z_{\rm th}) = 1/\tau_p$ and $Z_{\rm th}$ is the carrier density at the laser threshold.

It is convenient to normalise the above equations into dimensionless forms which read:

$$i\frac{d\tilde{a}_n}{dt} = i\frac{1}{\tau_p}(1 - i\alpha_{\rm H})\tilde{Z}_n\tilde{a}_n + t_1\tilde{b}_n + t_2\tilde{b}_{n-1}, \tag{1.22}$$

$$i\frac{d\tilde{b}_n}{dt} = -ig_B\tilde{b}_n + t_1\tilde{a}_n + t_2\tilde{a}_{n-1}, \tag{1.23}$$

$$\tau_s\frac{d\tilde{Z}_n}{dt} = \tilde{p}_A - \tilde{Z}_n - (1 + 2\tilde{Z}_n)|\tilde{a}_n|^2, \tag{1.24}$$

where the $\tilde{\bullet}$ quantities are normalised according to:

$$\tilde{a}_i = \sqrt{\frac{1}{2}\sigma\tau_s}a_i, \tag{1.25}$$

[4] If the convention used is $a_n \propto e^{+i\omega t}$, then the factor term $(1 - i\alpha_{\rm H})$ in Eq. 1.18 must be replaced by $(1 + i\alpha_{\rm H})$.

$$\tilde{b}_i = \sqrt{\frac{1}{2}\sigma\tau_s}\, b_i, \tag{1.26}$$

$$Z_i = \frac{1}{2}\sigma\tau_p Z_{th}\left(\frac{Z}{Z_{th}} - 1\right), \tag{1.27}$$

$$\tilde{p}_A = \frac{1}{2}\sigma\tau_p Z_{th}\left(\frac{p_A\tau_s}{Z_{th}} - 1\right) \tag{1.28}$$

For simplicity of notation, the tilde $\tilde{\bullet}$ is later dropped and the parameters for the time dynamics are chosen to be consistent with the linear and saturable gain.

The carrier dynamics' time-scale τ_s with respect to the photon dynamics' time-scale τ_p is important in the dynamical behaviour of the laser system. In the linearised regime, the linear gain is given by pump normalised intensity $g_A = g = p_A/\tau_p$. In so-called class-B lasers, the carrier dynamics are taken into account in the laser rate equation. On the other hand, in so-called class-A lasers, the carrier dynamics are adiabatically removed and the saturable gain [Eq. 1.16] is retrieved. As an example, Figs. 1.7(c) and 1.7(d) plot the time evolution of the amplitude of the first A site $|a_1(t)|$ in the class-A and the class-B laser regime, respectively, for specific parameters. This clearly shows that different dynamics happen when the carrier dynamics are taken into account. Besides, by comparing the class-A laser and saturable gain model, we can already see the effect of the carrier densities via the Henry factor α_{H} which shifts the frequency away from the zero-energy (resonant frequency). This, therefore, demonstrates the importance of studying the temporal dynamics in active non-Hermitian and non-linear topological insulators.

Chapter 2

Gapless unidirectional photonic transport using all-dielectric kagome lattices

2.1 Introduction

When propagating in a (structured) material or waveguide, not all of the light travels in the initial direction but parts of it experience back-reflection due to bending, fabrication defects or environmental variations. For most applications, back-propagation should be avoided and it is thus not surprising that the unique properties of PTIs [4, 55] have attracted widespread attention due to their promise to prohibit back-reflections. The basis of such back-reflection-free one-way waveguides lies at the interface of two topologically inequivalent PhCs which exhibit topological edge modes that propagate only in one direction and are at the same time robust against a certain type of perturbations. This is guaranteed by the bulk-boundary correspondence [56]. Not surprisingly, a plethora of possible topologically non-trivial photonic designs has been put forward, involving non-reciprocal systems [2], complex metamaterials [57], the Floquet topological insulator principle [7], and an artificial magnetic gauge [58, 59]. However, the aforementioned PTIs need strong magnetic fields, are complicated to fabricate, and/or are difficult if not impossible to scale to optical frequencies.

As an alternative, a deformed honeycomb-based topological PhC [11] which emulates the quantum spin Hall effect (QSHE) [11, 13, 60, 61] has recently gained interest, not least due to its simple fabrication as compared to other PTIs. Two-dimensional hexagonal symmetries, such as the honeycomb-based topological PhC, generally lead to linear degeneracy, called Dirac point, at the K and K′ points of the BZ. With a geometrical perturbation, it is possible to lift the point-like degeneracies in order to obtain a non-trivial topological and complete photonic bandgap [62] which leads to topological protection defined within the parameter space of a certain type of a deterministic geometrical perturbation. Nevertheless, there is an inherent problem. The pseudo-time-reversal anti-unitary operator $\mathcal{T}^2 = -\mathbb{1}$, introduced to have well-defined orthogonal spin up/down channels, is constructed based on the six-fold rotation (C_6) operator of the crystal. However, the C_6 symmetry of the crystal is broken in any finite, truncated, configuration and the spin up and spin down channels couple to each other. Consequently, while edge modes are guaranteed at the interface between the two topologically distinct deformed honeycomb PhCs, for most frequencies within the bandgap, there is an anti-crossing in their dispersion and they eventually do suffer from intrinsic back-reflection. Yet, starting from a C_{6v} symmetry with symmetry protected Dirac cones, it can be shown that there are two routes towards breaking the symmetry to open a topological bandgap without breaking optical reciprocity [62]: one related to the aforementioned QSHE [60], and the other to the quantum valley Hall effect (QVHE) [63]. The QVHE has been widely studied in photonic and mechanical systems with staggered honeycomb [18, 19, 25, 64–67] lattice, triangular rods [17, 23, 24] or multi-pod [20, 68, 69] structure.

In this chapter, we introduce an all-dielectric PTI based on a kagome lattice [70] that naturally lends itself to QVHE symmetry breaking [62] while being composed of monodisperse rods of a single dielectric material. The topology of the proposed kagome lattice is studied and the presence of robust topological edge modes is demonstrated at the interface between topologically distinct kagome lattices. In the last section, we present and model the predicted behaviour for an on-chip platform that can be readily fabricated with

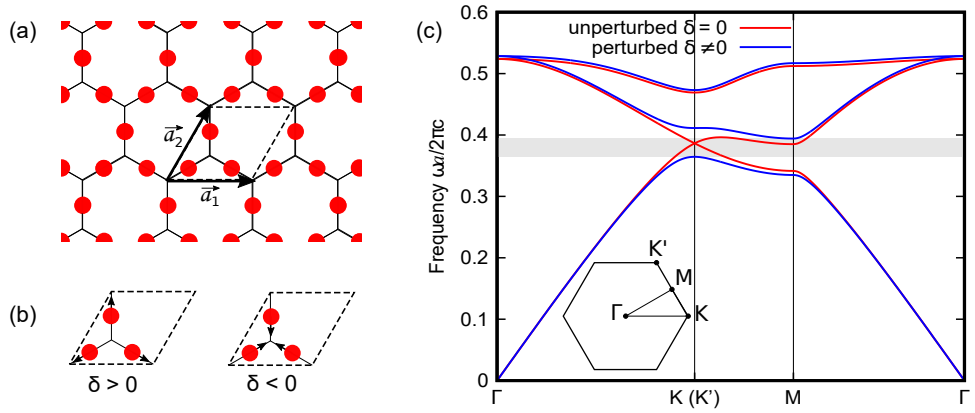

Figure 2.1: (a) Schematic of a kagome lattice. The solid line is a guide to the eye for the hexagonal symmetry. (b) Perturbations are considered by putting the rods further away (left) or closer (right) to each other, represented by the arrows. (c) Band structure of the kagome lattice for the unperturbed (solid red line) and perturbed (solid blue line) cases. The inset shows the first Brillouin zone.

state-of-the-art semiconductor growth techniques [71].

2.2 The 2D kagome lattice

The kagome lattice, named after a traditional Japanese basketweave pattern [70], has lattice sites at the midpoints of the edges in the regular hexagonal wallpaper tiling $\{6,3\}$, as illustrated in Fig. 2.1(a). The unit cell is here composed of three rods and the perturbation to lift the degeneracy can be introduced such that these rods get closer (negative perturbation $\delta<0$) or further away (positive perturbation $\delta>0$) from their shared corner of the hexagons [Fig. 2.1(b)]: $\boldsymbol{r}\mapsto\boldsymbol{r'}=(1\pm\delta)\boldsymbol{r}$ where $\boldsymbol{r}$ is a vector taken from the corner of a hexagon to the adjacent rod.

Importantly, the perturbation opens a bandgap by lifting the linear degeneracy at the K and K$'$ points which is symmetry-induced in the unperturbed case. This generic behaviour manifests itself in the photonic bandstructure for the E_z out-of-plane transverse magnetic (TM) polarisation [Fig. 2.1(c)] obtained with the open-source software *MIT Photonic Bands* (MPB) [72] for the unperturbed $\delta=0$ and perturbed $\delta=\pm0.15$ case. The kagome photonic crystal, with lattice constant a, is composed of rods with diameter $d=0.2a$ and permittivity $\varepsilon=12$ within a vacuum ($\varepsilon=1$) background. In contrast to

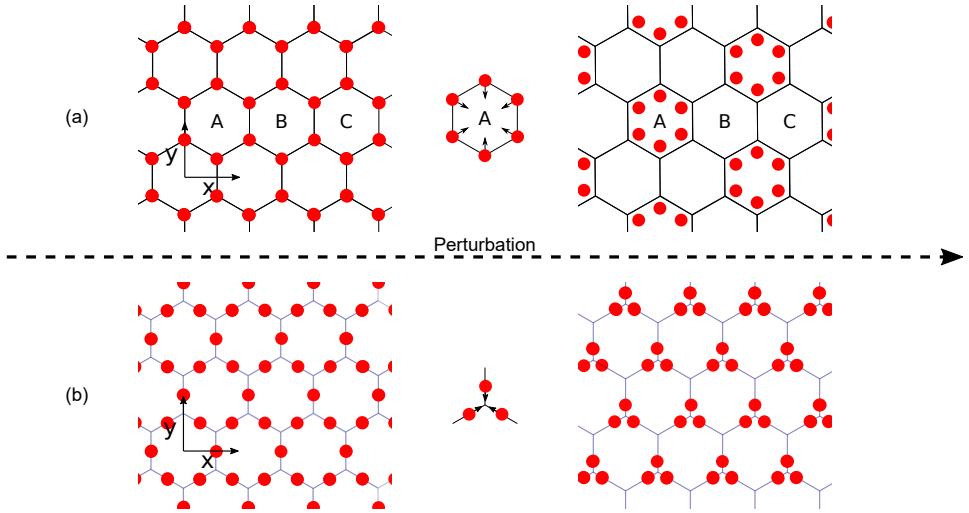

Figure 2.2: Schematic of two hexagonal lattice designs with broken C_{6v} symmetry. (a) QSHE honeycomb structure with sites at the corners of the hexagons. The design is perturbed by shrinking/expanding every third hexagon labelled A. (b) QVHE kagome structure with sites at the centre of the edges of the hexagons. The design is perturbed by moving the rods along the edges.

the perturbed honeycomb PhC [11], the translation symmetry is conserved after the perturbation as illustrated in Fig. 2.2, *i.e.* the primitive lattice vectors (albeit not unique) are themselves preserved. As a consequence, the reciprocal lattice vectors remain the same and therefore the K and K′ points remain distinct and do not map to the Γ point as in the case of the perturbed honeycomb lattice [11].

To describe the bandgap opening more rigorously, we adopt a perturbation-based group theoretical approach detailed in Ref. [62] to the hexagonal wallpaper group *p6mm (17)*. Then, an effective Hamiltonian is derived for a (small) geometrical perturbation, $\tilde{\delta}$, and close to K, $\delta\boldsymbol{k} = (\delta k_x, \delta k_y)$, in the canonical basis of the induced K irreducible representation (irrep) from the 2D little group irrep of $p6mm$ [73]:

$$\mathcal{H}_{\text{kagome}} = \delta k_x \gamma_1 - \delta k_y \gamma_2 + \tilde{\delta}\gamma_5 = \begin{pmatrix} \mathcal{W}_{\text{K}} & 0 \\ 0 & \mathcal{W}_{\text{K}'} \end{pmatrix} \tag{2.1}$$

where $\gamma_1 := \sigma_3 \otimes \sigma_3$, $\gamma_2 := \sigma_3 \otimes \sigma_1$, $\gamma_3 := \sigma_1 \otimes \mathbb{1}_2$, $\gamma_4 := \sigma_2 \otimes \mathbb{1}_2$, $\gamma_5 := \sigma_3 \otimes \sigma_2$ are matrices satisfying a Clifford algebra generated by the vector field spanned by the γ_i, with the associated anti-commutation relation $\{\gamma_i, \gamma_j\} = 2\delta_{ij}\mathbb{1}_4$.

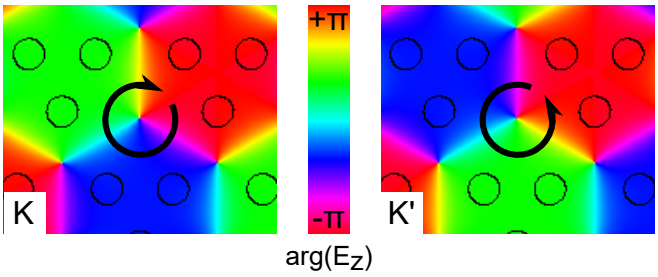

Figure 2.3: Phases of the z-component of the electric field E_z for the first band in Fig. 2.1 at K and K' points.

$\mathcal{W}_{\mathrm{K/K'}} = \pm\, \boldsymbol{h}\cdot\boldsymbol{\sigma}$ represent Weyl Hamiltonians of opposite chirality in the vicinity of K/K′ with $\boldsymbol{h} = (-\delta k_y, \tilde{\delta}, \delta k_x)$ and $\boldsymbol{\sigma} = (\sigma_1, \sigma_2, \sigma_3)$ the Pauli matrix vector. In Eq. 2.1, $\tilde{\delta}$ models the geometrical perturbation and therefore is proportional to the displacement of the rods δ away from the original ones in the unperturbed lattice. The eigenvalues E of the Weyl Hamiltonian at the K/K′ point are $E = \pm\sqrt{\delta k_x^2 + \delta k_y^2 + \tilde{\delta}^2}$ confirming that we obtain a linear degeneracy (Dirac point) in the 2D BZ for $\tilde{\delta} = 0$, *i.e.* for the unperturbed kagome lattice, and have a bandgap for $\tilde{\delta} \neq 0$. The proposed geometrical perturbations essentially break the inversion symmetry and introduce a mass term $\tilde{\delta}$ to the Weyl Hamiltonians $\mathcal{W}_{\mathrm{K/K'}}$.

Additionally, from Eq. 2.1 it is clear that the effective Hamiltonian $\mathcal{H}_{\mathrm{kagome}}$ is necessarily block-diagonalised [73] in its canonical basis as in the case with the QSHE Kane-Mele Hamiltonian [60] because translation symmetry is not broken with the perturbation. It does not mix the K/K′ irrep of the invariant translation group. The K/K′ points thus play the role of two orthogonal pseudo-spin channels, known as the valley degree of freedom, with the generating unitary pseudo-time-reversal operator $\tilde{\mathcal{T}} = \sigma_3 \otimes \mathbb{1}_2$ with $[\tilde{\mathcal{T}}, \mathcal{H}_{\mathrm{kagome}}] = 0$, invariant under rotational symmetry breaking. This valley degree of freedom can be seen in Fig. 2.3 showing the phase of the z-component of the electric field (E_z) going clockwise or anti-clockwise, around the original C_{6v} points, at the K and K' points for the first band.

One should note that the results obtained above rely only on the symmetry of the system and similar results are obtained for H_z out-of-plane transverse electric (TE) polarisation.

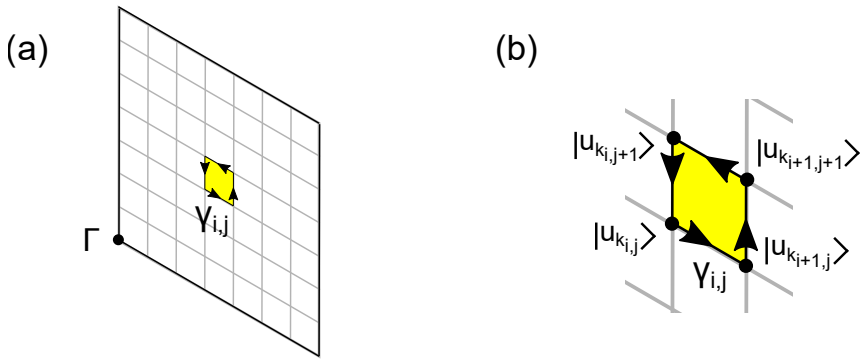

Figure 2.4: (a) Sketch of a closed path inside the (discretised) primitive unit cell in the reciprocal space. Γ is the origin of the BZ: $\boldsymbol{k} = (0, 0)$. $\gamma_{i,j}$ is the Berry phase defined along the drawn loop and the yellow shaded area is the surface S generated by this latter closed contour. (b) Zoom-in on the closed path. $|\boldsymbol{u}_{\boldsymbol{k}_{i,j}}\rangle$ are the eigenvectors at point $\boldsymbol{k}_{i,j}$ in the reciprocal space.

2.3 Topological characterisation

In valley Hall systems, the topological characterisation is different from other 2D topological phases such as the quantum Hall phase or QSHE phase [60, 74, 75]. To show how the proposed kagome design emulates the QVHE emerging from the non-trivial Dirac points in the 2D BZ, one can use the valley Chern number defined at the K and K′ points [17–20, 23–25, 64–66, 68, 69]:

$$C_{\mathrm{K/K'}} = \frac{1}{2\pi} \int_{S_{\mathrm{K/K'}}} \boldsymbol{\mathcal{F}}(\boldsymbol{k})\, d^2\boldsymbol{k}, \tag{2.2}$$

where the integrand is the Berry curvature [76] $\boldsymbol{\mathcal{F}}(\boldsymbol{k}) = \nabla \times i\langle \boldsymbol{u}_{\boldsymbol{k}} | \nabla_{\boldsymbol{k}} \boldsymbol{u}_{\boldsymbol{k}} \rangle$, and the integration is performed near the two valley domains $S_{\mathrm{K/K'}}$,

Numerically, calculating the Chern number, or more generally the Berry curvature, is complicated if we do not have an easy closed-form analytical expression of the corresponding Hermitian operator. Indeed, for each $\boldsymbol{k}$ point, the eigenvectors carry a random phase $e^{i\phi(\boldsymbol{k})}|\boldsymbol{u}_{\boldsymbol{k}}\rangle$ which is a numerical problem because of the derivative with respect to $\boldsymbol{k}$ appearing in the Berry curvature $\boldsymbol{\mathcal{F}}(\boldsymbol{k}) = \nabla_{\boldsymbol{k}} \times i\langle \boldsymbol{u}_{\boldsymbol{k}} | \nabla_{\boldsymbol{k}} \boldsymbol{u}_{\boldsymbol{k}} \rangle$.

One solution is to start with the Berry phase $\gamma_{i,j}$ over a loop defined as in Fig. 2.4(a). Assuming the Berry connection is behaving well enough, one can

apply Stokes' theorem which yields:

$$\gamma_{i,j} = \int_S \boldsymbol{\mathcal{F}}(\boldsymbol{k}) \cdot d^2\boldsymbol{k} = \mathcal{F}_{i,j}\, S \tag{2.3}$$

where S is the surface generated by the closed path and $\mathcal{F}_{i,j}$ is the Berry curvature defined at the $\boldsymbol{k}_{i,j}$ point [Fig. 2.4(b)] and assumed to be constant in the surface S. Therefore, the Berry curvature can be seen as a Berry phase per unit area:

$$\mathcal{F}_{i,j} = \frac{\gamma_{i,j}}{S}. \tag{2.4}$$

The problem is then reduced to calculating the Berry phase instead of the Berry curvature. By definition, the Berry phase is the geometric phase that the eigenvector acquires after doing a loop in the parameter space. The phase difference $\Delta\phi_{\boldsymbol{k}}$ between two eigenvectors $|\boldsymbol{u}_{\boldsymbol{k}}\rangle$ and $|\boldsymbol{u}_{\boldsymbol{k'}}\rangle$ is:

$$\Delta\phi_{\boldsymbol{k}} = \mathrm{Im}\left[\ln(e^{i\Delta\phi_{\boldsymbol{k}}})\right] \tag{2.5}$$

with

$$e^{i\Delta\phi_{\boldsymbol{k}}} = \frac{\langle \boldsymbol{u}_{\boldsymbol{k}} | \boldsymbol{u}_{\boldsymbol{k'}} \rangle}{\left| \langle \boldsymbol{u}_{\boldsymbol{k}} | \boldsymbol{u}_{\boldsymbol{k'}} \rangle \right|}. \tag{2.6}$$

This means that, in this case [Fig. 2.4(b)]:

$$\gamma_{i,j} = \mathrm{Im}\Big[\ln\Big(\langle \boldsymbol{u}_{\boldsymbol{k}_{i,j}} | \boldsymbol{u}_{\boldsymbol{k}_{i+1,j}} \rangle \langle \boldsymbol{u}_{\boldsymbol{k}_{i+1,j}} | \boldsymbol{u}_{\boldsymbol{k}_{i+1,j+1}} \rangle \langle \boldsymbol{u}_{\boldsymbol{k}_{i+1,j+1}} | \boldsymbol{u}_{\boldsymbol{k}_{i,j+1}} \rangle \langle \boldsymbol{u}_{\boldsymbol{k}_{i,j+1}} | \boldsymbol{u}_{\boldsymbol{k}_{i,j}} \rangle \Big)\Big] \tag{2.7}$$

where the inner product[1] for the electric field is defined as [1]:

$$\langle \boldsymbol{u}_{\boldsymbol{k}} | \boldsymbol{u}_{\boldsymbol{k'}} \rangle = \int \boldsymbol{u}^*_{\boldsymbol{k}}(\boldsymbol{r}) \cdot \epsilon(\boldsymbol{r}) \boldsymbol{u}_{\boldsymbol{k'}}(\boldsymbol{r})\, d\boldsymbol{r} \tag{2.8}$$

such that the photonic operator for the eigenvalue problem is Hermitian [1]. One can note that the expression for the Berry curvature $\mathcal{F}_{i,j}$ [Eqs. 2.4 and 2.7] is now gauge-independent since the randomly k-dependent phases cancel each other in the $|\boldsymbol{u}_{\boldsymbol{k}}\rangle\langle\boldsymbol{u}_{\boldsymbol{k}}|$ term. Moreover, $\mathcal{F}_{i,j}$ converges to the continuous form when the spacing between neighbouring k-points approaches zero.

Figure 2.5 shows the Berry curvatures calculated for a positively ($\delta = +0.15$)

[1] The inner product for the magnetic field is given by $\langle \boldsymbol{u}_{\boldsymbol{k}} | \boldsymbol{u}_{\boldsymbol{k'}} \rangle = \int \boldsymbol{u}^*_{\boldsymbol{k}}(\boldsymbol{r}) \cdot \boldsymbol{u}_{\boldsymbol{k'}}(\boldsymbol{r})\, d\boldsymbol{r}$.

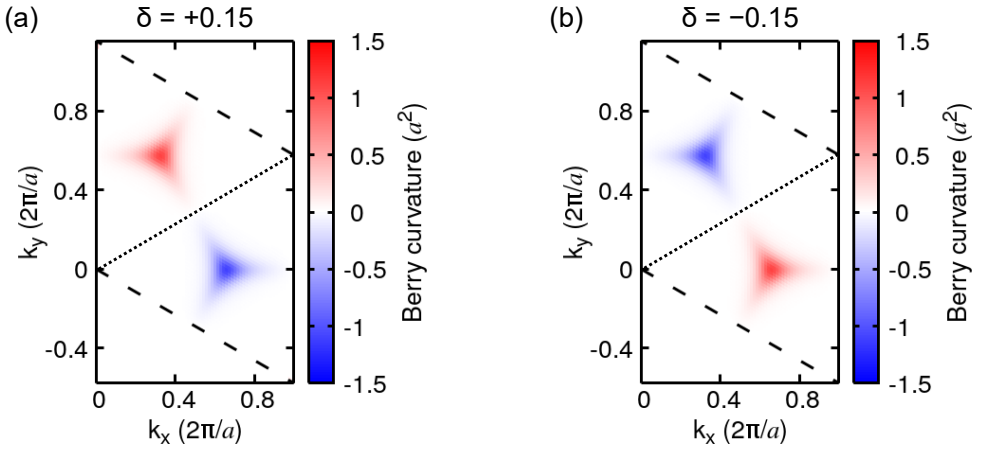

Figure 2.5: Calculated Berry curvatures in the reciprocal primitive unit cell for (a) positively and (b) negatively perturbed kagome lattices. The dashed line represents the limit of the reciprocal primitive unit cell and the dotted black line defines the boundary for the regions of integration $S_{\mathrm{K/K'}}$.

and negatively ($\delta = -0.15$) deformed kagome lattice, for $\boldsymbol{k}$-points in the reciprocal primitive unit cell. The electric field distribution of the Bloch states has been obtained from the calculation of the band structure using MPB. Because of inversion symmetry breaking, the Berry curvature need not vanish everywhere in the BZ. In fact, the Berry curvature has a non-zero and opposite sign around the two valleys (given perturbation configuration).

The valley Chern number $C_{\mathrm{K/K'}}$ is obtained by summing the Berry curvature $\mathcal{F}_{i,j}$ at the $\boldsymbol{k}_{i,j}$ point over the desired surface $S_{\mathrm{K/K'}}$. The integration is performed over the two valley domains $S_{\mathrm{K/K'}}$ defined in Fig. 2.5 as the two triangles which together form the dual of the standard hexagonal BZ tessellation of reciprocal space The valley Chern number obtained for positive (negative) perturbation $\delta = 0.15$ ($\delta = -0.15$) by integrating around the K/K′ are $C_{\mathrm{K/K'}} = \pm 0.18$ ($C_{\mathrm{K/K'}} = \mp 0.18$).

However, $C_{\mathrm{K/K'}}$ is not a quantised topological invariant because $S_{\mathrm{K/K'}}$ is not a closed surface. We further show that the valley Chern number $C_{\mathrm{K/K'}}$ depends on the perturbation strength and explain why $C_{\mathrm{K/K'}} = \pm 0.5$ [17–20, 23–25, 64–66, 68, 69] is only achieved for infinitesimal perturbation.

Recall the Weyl Hamiltonian in the vicinity of the K point takes the fol-

lowing form:

$$\mathcal{W} = \boldsymbol{h} \cdot \boldsymbol{\sigma} \tag{2.9}$$

where $\boldsymbol{h} = (h_x, h_y, h_z) = (-\delta k_y, \tilde{\delta}, \delta k_x)$ is a vector in a three-dimensional (3D) parameter space, $\delta k_i = k_i - k_{K,i}\,,\ i = x, y$ [Eq. 2.1]. This gives the following Berry curvature, for the lower band [76]:

$$\boldsymbol{\mathcal{F}}(\boldsymbol{h}) = -\frac{1}{2}\frac{\boldsymbol{h}}{|\boldsymbol{h}|^3} \tag{2.10}$$

with $|\boldsymbol{h}| = \sqrt{\delta k_x^2 + \delta k_y^2 + \tilde{\delta}^2} = \sqrt{\boldsymbol{\delta k}^2 + \tilde{\delta}^2}$. By integrating over a loop around K, γ_{K}, the valley Chern number is:

$$C_{\mathrm{K}} = \frac{1}{2\pi}\int_{S_{\mathrm{K}}} \boldsymbol{\mathcal{F}}(\boldsymbol{h})\, d^2\boldsymbol{k} = \frac{1}{2\pi}\int_{S_{\mathrm{K}}} \frac{1}{2}\frac{\tilde{\delta}}{|\boldsymbol{h}|^3}\, dk_x dk_y \tag{2.11}$$

where $d^2\boldsymbol{k} = dk_x \wedge dk_y$, S_{K} is the surface generated by the closed path γ_{K}. This gives $C_{\mathrm{K}} = -\operatorname{sign}(\tilde{\delta})\frac{1}{2}$.

However, $C_{\mathrm{K}} = -\,C_{\mathrm{K}'}$ because of time-reversal symmetry, hence we need to take this opposite Weyl charge into account in the practical calculation: the information from the positive and negative Weyl charges cannot be separated numerically. Indeed, for numerical calculation, the loop is chosen, for simplicity, to be half the BZ, as depicted in Fig. 2.6(a). Therefore, when calculating the Berry curvatures, the Berry flux coming from the positive and negative charges cancel each other for high enough perturbation $\tilde{\delta}$. Thus the valley Chern number becomes:

$$\tilde{C}_{\mathrm{K}} = \frac{1}{2\pi}\int_{S_{\mathrm{K}}} \tilde{\boldsymbol{\mathcal{F}}}(\boldsymbol{h})\, d^2\boldsymbol{k} \tag{2.12}$$

where, here, the tilde on $\tilde{C}_{\mathrm{K}}$ and $\tilde{\boldsymbol{\mathcal{F}}}(\boldsymbol{h})$ stands for the practical value, numerically calculated, of the valley Chern number and Berry curvature, with:

$$\tilde{\boldsymbol{\mathcal{F}}}(\boldsymbol{\delta k}, \tilde{\delta}) = \tilde{\boldsymbol{\mathcal{F}}}_{\mathrm{K}}(\boldsymbol{\delta k}, \tilde{\delta}) + \tilde{\boldsymbol{\mathcal{F}}}_{\mathrm{K}'}(\boldsymbol{\delta k}, \tilde{\delta}). \tag{2.13}$$

The positive and negative Weyl charges contribution at K and K′ are given by

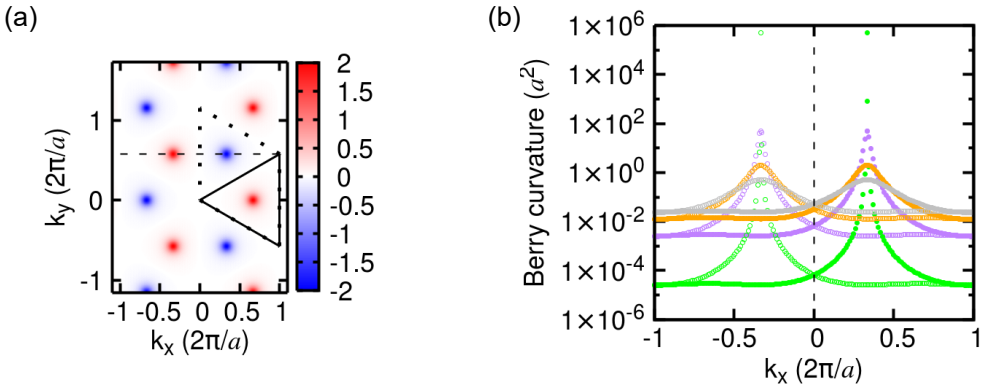

Figure 2.6: (a) Berry curvatures calculated using Eq. 2.13 with perturbation $\tilde{\delta} = 0.5$. The dotted line shows the limit of one reciprocal primitive unit cell. The solid line represents the contour γ_K used to calculate the K-valley Chern number. The horizontal dashed line represents the path followed in order to plot (b). (b) Plot of the absolute value of the Berry curvature for different perturbations: $\tilde{\delta} = 10^{-3}$ (green circles), $\tilde{\delta} = 0.1$ (purple circles), $\tilde{\delta} = 0.5$ (orange circles) and $\tilde{\delta} = 1$ (grey circles). The open and closed correspond to $\tilde{\boldsymbol{\mathcal{F}}}_{\mathrm{K}}(\boldsymbol{\delta k}, \tilde{\delta})$ and $\tilde{\boldsymbol{\mathcal{F}}}_{\mathrm{K}'}(\boldsymbol{\delta k}, \tilde{\delta})$ respectively. The vertical dashed line represents the boundary of the contour integration.

$\tilde{\boldsymbol{\mathcal{F}}}_{\mathrm{K}}(\boldsymbol{\delta k}, \tilde{\delta})$ and $\tilde{\boldsymbol{\mathcal{F}}}_{\mathrm{K}'}(\boldsymbol{\delta k}, \tilde{\delta})$ respectively:

$$\tilde{\boldsymbol{\mathcal{F}}}_{\mathrm{K}}(\boldsymbol{\delta k}, \tilde{\delta}) = \frac{\tilde{\delta}}{2} \sum_{(m,n)\in\mathbb{Z}^2} \left[(\boldsymbol{\delta k}_{m,n})^2 + \tilde{\delta}^2 \right]^{-3/2}, \tag{2.14}$$

$$\tilde{\boldsymbol{\mathcal{F}}}_{\mathrm{K}'}(\boldsymbol{\delta k}, \tilde{\delta}) = -\frac{\tilde{\delta}}{2} \sum_{(m,n)\in\mathbb{Z}^2} \left[(\boldsymbol{\delta k}_{1/2+m,1/2+n})^2 + \tilde{\delta}^2 \right]^{-3/2} \tag{2.15}$$

where $\boldsymbol{\delta k}_{m,n} = \boldsymbol{k} + m\boldsymbol{b_1} + n\boldsymbol{b_2} - \boldsymbol{k}_{\mathrm{K}}$, with the reciprocal lattice vectors $\boldsymbol{b_i}$.

Figure 2.6(a) shows the calculated Berry curvature using Eq. 2.13 with perturbation $\tilde{\delta} = 0.5$. The dotted lines correspond to one reciprocal primitive unit cell and the solid lines represent the contour integral γ_{K} performed to calculate the K-valley Chern number. The horizontal dashed line represents the path followed to plot the absolute of the Berry curvatures $\tilde{\boldsymbol{\mathcal{F}}}_{\mathrm{K}}(\boldsymbol{\delta k}, \tilde{\delta})$ and $\tilde{\boldsymbol{\mathcal{F}}}_{\mathrm{K}'}(\boldsymbol{\delta k}, \tilde{\delta})$ in Fig. 2.6 in open and closed circles, respectively. In Fig. 2.6(b), the Berry curvature is plotted for $\tilde{\delta} = 10^{-3}$ (green circles), $\tilde{\delta} = 0.1$ (purple circles), $\tilde{\delta} = 0.5$ (orange circles) and $\tilde{\delta} = 1$ (grey circles). The vertical dashed line represents the boundary of the contour integration. This illustrates that for infinitesimal small perturbation, the "leakage" of the Berry flux can be negligible compared to its high value at the K/K′ points and one gets $\tilde{C}_K = 0.5$. In

contrast, when the perturbation is relatively high, *i.e.* not infinitesimal, the Berry flux associated with Weyl charges are leaking out of the more or less arbitrarily defined valley domain $\gamma_{\mathrm{K/K'}}$ respectively, and are cancelling with the Berry flux of opposite Weyl charges. For $\gamma_{\mathrm{K/K'}}$ defined as in Fig. 2.6, this results in lower valley Chern number than expected: $\tilde{C}_K = 0.47$ for $\tilde{\delta} = 0.1$, $\tilde{C}_K = 0.36$ for $\tilde{\delta} = 0.5$ and $\tilde{C}_K = 0.25$ for $\tilde{\delta} = 1$. The same analysis is mirrored for the K′ point and its corresponding valley Chern number $\tilde{C}_{K'}$. This shows that the valley Chern number is not a proper topological invariant since the sign of the perturbations is the same, *i.e.* the gap remains open, but the valley Chern number calculated changes for different perturbations.

The angular distribution of the Berry curvature obtained here is different from the one obtained with MPB. The difference is rooted in the fact that the Weyl Hamiltonian [Eq. 2.9] is only a first-order approximation of perturbations in any direction, i.e. not valid for finite geometrical perturbation. Of course, that does not change the valley Chern number for any surface enclosing only one Weyl monopole, *i.e.* the integrated Berry flux stays the same, but the angular distribution of the Berry flux will generally be altered. The cancellation of Berry flux associated with opposite Weyl charges will therefore be different. However, as we will see in the following, only the sign matters in determining the topology and possible topological edge modes.

Although the valley Chern number is not a topological invariant, a strong bulk-boundary correspondence similar to Ref. [56] exists in the extended parameter space $(-\delta k_y, \tilde{\delta}, \delta k_x)$ where Weyl charges of opposite chirality lead to guaranteed edge modes in the K/K′ valleys, respectively [62]. These Weyl charges can be correlated one-to-one to the sign of the valley Chern numbers, which can thus be interpreted as a topological integer with associated bulk-boundary correspondence. In contrast to Ref. [56], however, the existence of the strong correspondence in the extended parameter space only fixes crystal termination and is only valid for inclinations for which the K and K′ points are not projected to the same point in the edge BZ [cf. BZ insets in Fig. 2.7]. The bulk-boundary correspondence thus reduces to the weaker form which is rigorously valid only for specific well-defined boundaries.

Alternatively, the existence of the topological edge states can be seen as a consequence of a non-zero Berry curvature around the two valleys in a low-energy continuum model. These edge states with linear dispersion can be found as a solution of a domain wall type Dirac equation where the mass term changes sign across the interface [akin to Chap. 1].

From the expression of the effective Hamiltonian $\mathcal{H}_{\text{kagome}}$, it is evident that a non-trivial Weyl charge is located at the K and K$'$ points which have opposite signs because $\mathcal{W}_{\text{K}} = -\mathcal{W}_{\text{K}'}$ and which has opposite signs for opposite perturbation strength as well. The Weyl Hamiltonian near the K point is given by:

$$\mathcal{W}_K = -\delta k_y \sigma_x + \tilde{\delta}\sigma_y + \delta k_x \sigma_z. \tag{2.16}$$

At the domain wall between topologically distinct phases, $\tilde{\delta}$ changes sign:

$$\tilde{\delta}(x) = \begin{cases} \tilde{\delta}_0 & x > 0 \\ -\tilde{\delta}_0 & x < 0 \end{cases} \tag{2.17}$$

The continuum Hamiltonian $H_{\text{continuum}}$ is then obtained by replacing the wave vector δk_x with $-i\partial_x$ since translation along the a_1-direction is here broken. The edge states $\varphi(x, y)$ with energy E at the interface need to satisfy:

$$H_{\text{continuum}}\varphi(x, y) = E\varphi(x, y). \tag{2.18}$$

With the following ansatz of the localised state on the left and right side of the interface:

$$\varphi(x, y) = \begin{pmatrix} a_i \\ b_i \end{pmatrix} e^{i\delta k_y y} e^{\pm\kappa x}, \tag{2.19}$$

one can show, from the continuity of the state at the interface, that $E = q_y$, $\kappa = \tilde{\delta}_0$ with $a_i = 1$, $b_i = -1$:

$$\varphi(x, y) = \begin{pmatrix} 1 \\ -1 \end{pmatrix} e^{i\delta k_y y} e^{\pm\kappa x}. \tag{2.20}$$

More generally, one can show that an edge state with linear dispersion $E = q_y$

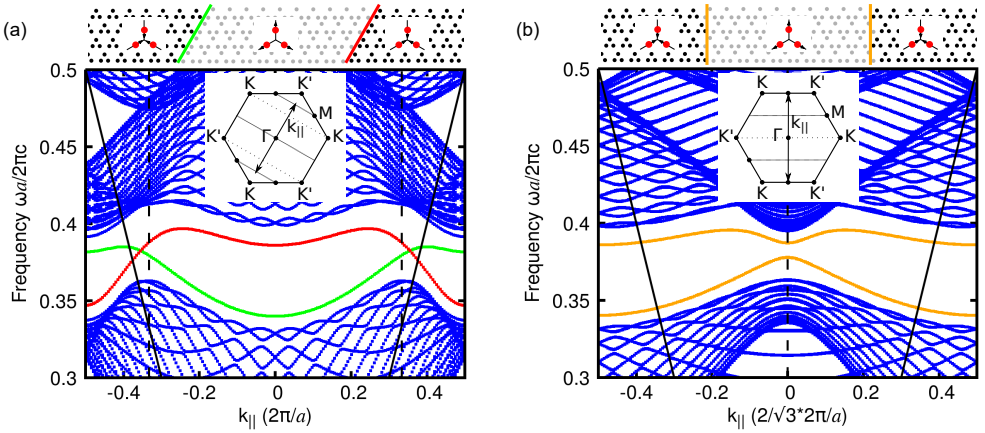

Figure 2.7: Supercell band structure at the interface between two topologically distinct kagome photonic crystals along different inclination directions: (a) Γ−K, (b) Γ−M. The front and back interfaces are represented by solid lines with different colours on both the sketch and the band structure in (a). In (b), the interfaces and the edge mode dispersions are represented by the same colour because the two interfaces are equivalent. The insets show the $k_{\|}$ sweep direction. The solid black line represents the light lines. The vertical dashed lines mark the position of K/K′. The parameters are the same as in Fig. 2.1 and with perturbation strength $\delta = \pm 0.15$.

exists along the interface of two systems characterised by opposite mass terms:

$$\varphi(x,y) = \begin{pmatrix} 1 \\ -1 \end{pmatrix} C e^{i\delta k_y y} e^{-\int_0^x dx' \tilde{\delta}(x')}, \tag{2.21}$$

with C a constant scalar.

Similar results can be obtained at the K′ point, except that the dispersion will have an opposite slope. Therefore, at the interface between $\mathcal{H}_{\text{kagome}}$ where the mass term changes, the bulk-edge correspondence manifests as gapless valley-dependent edge states at the interface. As a consequence, the interface between two systems characterised by different signs in the valley Chern numbers or different signatures in the Berry curvature leads to counter-propagating topological edge modes locked to their valley degree of freedom, given no valley mixing.

2.4 Topological protected mode

Based on the Berry curvature plots in Fig. 2.5, starting with an unperturbed lattice and then perturbing positively on one side of a chosen interface and neg-

atively on the other side could potentially lead at most frequencies to counter-propagating topological edge modes locked to their valley degree of freedom. Figure 2.7 shows the corresponding supercell band structure for $\delta = \pm 0.15$ and for different interface inclinations. The solid blue lines correspond to the bulk modes and the solid coloured lines correspond to topological edge modes inside the bulk bandgap. This figure shows that an anti-crossing arises when the K/K′ points are projected onto the same $k_{\|}$ points [Γ−M inclination, Fig. 2.7(b)] while a crossing arises for Γ−K inclination, [Fig. 2.7(a)]. In the Γ−K inclination case [Fig. 2.7(a)], each interface supports two counter-propagating edge modes corresponding to the well-defined pseudo-spin up (down) edge modes of the K (K′) valleys. These result from the opposite Weyl charges at the K (or K′) point for two sides of the interface [56, 62]. In the Γ−M inclination case [Fig. 2.7(b)], however, the pseudo-spin separation breaks down and the edge modes suffer from back-scattering, similarly to the honeycomb PhC [11].

From the counter-propagating modes locked to their valley degree of freedom at a given frequency, the left or right mover can be excited using a circularly polarised source [11, 77] and located at a specific spatial position of the source. If the source chosen is left-polarised $S_+ = H_x + iH_y$, only one pseudo-spin unidirectional edge mode can be excited by locating the source at a certain position. The information is given by means of a wave-vector $k_{\|}$-dependent chirality map [78]. Figure 2.8(a) shows the interface considered: it corresponds to the red interface in Fig. 2.7 with perturbation $\delta = \pm 0.15$. Therefore we will be looking at only the edge modes represented by the red dispersion line in the following.

TM modes (non-zero E_z, H_x, H_y) are considered here but the concept of chirality of the edge modes can be similarly applied to TE modes (non-zero H_z, E_x, E_y). From the magnetic field components (H_x, H_y) of the edge modes, the chirality of the mode is calculated using the Stokes parameters:

$$S_1 = |H_x|^2 - |H_y|^2, \tag{2.22}$$

$$S_2 = 2Re(H_x H_y^*), \tag{2.23}$$

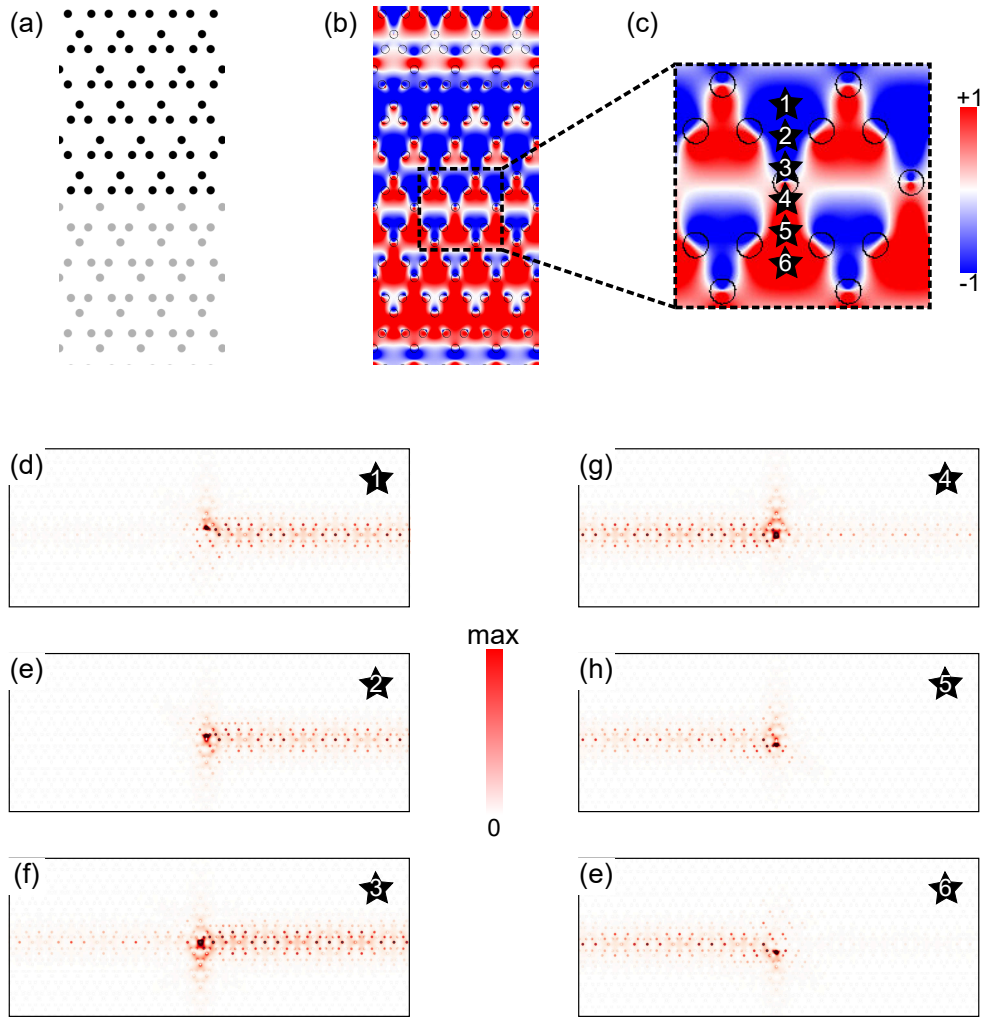

Figure 2.8: (a) Sketch of the interface considered between two opposite kagome lattice. (b) Chirality map calculated at the $k_{\|} = 0.4\,(2\pi/a)$ point. (c) Zoom in of (c) with different positions of the source considered represented by the stars. (d)-(e) Snapshot of the total power of the edge mode for the different positions of the source with polarised source $S_+ = H_x + iH_y$.

$$S_3 = -2Im(H_x H_y^*). \tag{2.24}$$

On the Poincaré sphere defined by (S_1, S_2, S_3), the chirality is then defined as $\tan(\chi)$ where:

$$\chi = \frac{1}{2}\arctan\left(\frac{S_3}{\sqrt{S_1^2 + S_2^2}}\right). \tag{2.25}$$

Using the Bloch states of the bandstructure obtained from MPB, Fig. 2.8(b) shows the calculated chirality at the corresponding $k_{\|} = 0.4\,(2\pi/a)$ point. It is interesting to see that the chirality map has a region between the two different PTIs with almost the same sign of values [close to $+1$ (-1), shown in

red (blue) in Fig. 2.8(b)]. This implies that different circular polarisations are needed to excite edge modes propagating in the same direction at the two positions [*e.g.* points denoted by "1" and "6" in Fig. 2.8(c)]. Alternatively, the same circularly polarised dipoles at the two positions would excite edge modes propagating in the opposite direction. This is demonstrated in Figs. 2.8(d) and 2.8(e) using the full-wave dynamics of the 2D system via the open-source software *MIT Electromagnetic Equation Propagation* (MEEP) [79]. The total power $(\boldsymbol{E}^* \cdot \boldsymbol{D} + \boldsymbol{H}^* \cdot \boldsymbol{B})/2$ is plotted for different source positions "1" to "6" [Fig. 2.8(c)], with polarisation $S_+ = H_x + iH_y$. Starting with the source located at the position "1", *i.e.* in the negative chirality, the excited topological edge mode corresponds to the one propagating to the right. Moving the location of the source to position "6" with positive chirality will predominantly excite the mode propagating to the left. Therefore the position of the source is crucial for the excitation of unidirectional topological edge modes, as in other systems [14, 77, 80, 81] with the main difference being the robustness to bendings.

We here demonstrate broadband back-reflection-immunity numerically in Fig. 2.9 for finite perturbations, going beyond what has been shown rigorously for infinitesimal perturbation strengths with our generic theory based on symmetry only. The unidirectional propagation with negligible inter-valley coupling is demonstrated by studying the transmission through waveguides with bendings of different inclinations. Because the simulations are in 2D, there is no out-of-plane loss and any energy that is not transmitted is back-reflected. The unidirectional edge mode has been excited using a rotating magnetic point dipole source and the spatial position of the source has been determined using the chirality map obtained above [Fig. 2.8]. Figures 2.9(a) and 2.9(b) show two examples of waveguides oriented in a $\Gamma-$K inclination direction in which a bending is introduced such that the projected wavevectors of K and K$'$ onto the $k_{\parallel}$ line are distinct in a Z-shaped design [Fig. 2.9(a), inset Fig. 2.7(a)], or fall onto the same point along the vertical interface in a staircase-shaped design [Fig. 2.9(b), inset Fig. 2.7(b)]. In the case of the Z-shaped waveguide, we focus on the red interface highlighted in Fig. 2.7(a) (which is not equivalent to the green interface). Figure 2.9(c) shows the normalised transmitted flux at

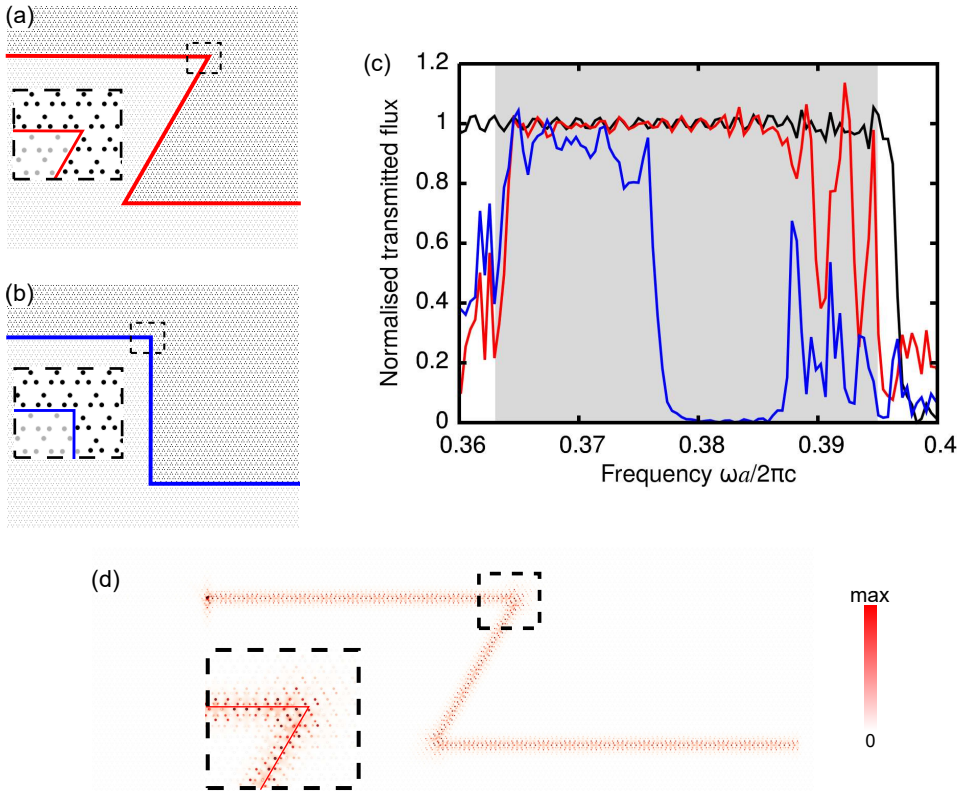

Figure 2.9: (a)-(b) Waveguides where the bending has a: (a) Z-shape or (b) staircase-shape where the bright (dark) rods are the positively (negatively) perturbed kagome lattice. Insets are the zoom-in on the interface at the dashed square region. (c) Transmission spectra for a waveguide without any bending (solid black line), Z-shaped (solid red line) or staircase-shaped (solid blue line) bending. The shaded area is a guide for the bandgap frequency range. The parameters are kept the same as in Fig. 2.7. (d) Power of the edge modes excited at the Z-shaped bending structure. The 2D full-wave simulations have perfect matching layer (PML) boundary conditions in the x- and y-directions.

the end of the waveguides. This has been obtained from 2D simulations of the waveguides in MEEP where the flux monitors are positioned after the bendings and far enough from boundary of the simulation cell. The transmission spectra of the bent waveguide are then normalised with respect to the transmission of a straight waveguide with the same geometrical parameters. At high frequencies, around the upper edge of the photonic bulk bandgap, large oscillations are observed due to the presence of additional modes that couple with the two valley channels [see Fig. 2.7]. Additional oscillations around the normalised transmission of 1 are also present because of numerical artefacts created by the source being directly inside the waveguide. The transmission for the Z-shaped waveguide (solid red line) is of the same order of magnitude as for a straight

waveguide (solid black line) for most of the frequencies inside the bandgap (represented by the grey shaded region). In contrast, the staircase-shaped bending (solid blue line) leads to substantial back-reflection resulting in lower transmission because of the non-negligible inter-valley couplings on the $\Gamma-$M inclination interface. This $\Gamma-$M inclination bending additionally introduces a bandgap in the dispersion where the edge mode cannot propagate. Broadband robust transmission is therefore achieved for the $\Gamma-$K inclination and in practice the orthogonality of two pseudo-spin channels at the wavevectors away from K/K$'$ is as good as at K/K$'$. Figure 2.9(d) shows a snapshot of the power profile for a mode propagating, with negligible back-reflection along the interface with bendings, excited by circular polarised source at frequency $\omega = 0.37\,(2\pi c/a)$.

2.5 Topological waveguide at telecommunication wavelengths

From a practical point of view, for the case of a $\Gamma-$K interface inclination, edge modes lie close to or below the light line, thus improving vertical mode confinement without the need of sandwiching the waveguides with mirrors [11]. To make use of the better confinement, we propose a design composed of an InGaAsP free-standing PhC slab ($n = 3.3$ [71]) of 170 nm thickness. Fabrication of this structure can be carried out using a III$-$V semiconductor wafer consisting of an InGaAsP substrate. The pattern of the air-holes can be defined by standard electron-beam lithography and inductively coupled plasma reactive-ion etching. Importantly, the proposed structure can be designed to work at telecommunication wavelengths, from 1.2 µm to 1.8 µm, as demonstrated in Fig. 2.10(a). The supercell band structure for TE-like modes (even-symmetric electric fields) is calculated with *Lumerical* [82], a finite-difference time-domain (FDTD) solver, for a lattice constant $a = 0.5$ µm, air-holes with diameter $d = 0.3a = 150$ nm and perturbation $\delta = \pm 0.15$. The bandgap ranges from 1.48 µm to 1.58 µm corresponding to a mid-gap at 1.53 µm. Since the materials are assumed to be lossless in our simulations, any temporal decay, quantified by γ in $E(t) \propto e^{i(\omega+i\gamma)t}$, is due to the leakiness of the mode. Figure 2.10(b) plots the slope of the curves corresponding to γ, and demonstrates

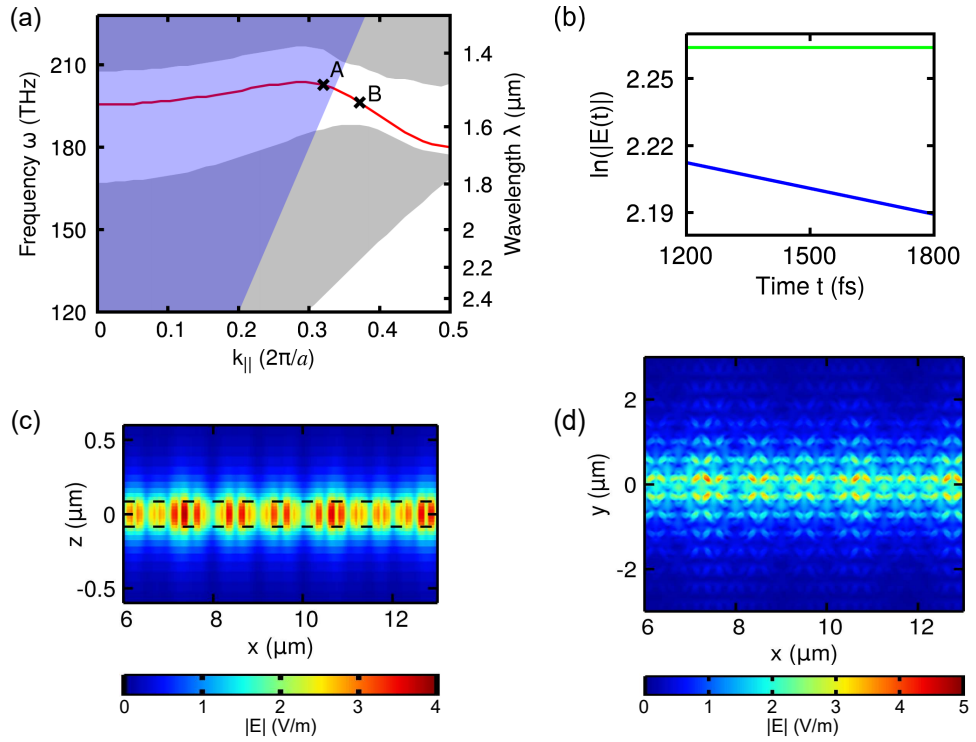

Figure 2.10: (a) Calculated band structure of the PhC slab along the front, red, interface configuration [see Fig. 2.7(a)]. The grey region corresponds to the projected bulk bandstructure, the red line is the edge mode dispersion and the purple shaded area represents the light cone. Modes at A and B are above and below the light line, respectively. The band structure has been obtained with Bloch PBCs on the (xy)-plane, PML boundary conditions in the z-direction and an air spacer layer between the slab and the PML. (b) Temporal decay of the mode at the point A (blue curve) and B (green curve) in (a). (c),(d) Field profile of the edge modes lying below the light line (point B) in the $y = 0$ plane and the $z = 0$ plane, respectively. The dashed lines are a guide to the eye for the z-limit of the free-standing slab. The field profiles have been obtained from time monitors after excitation of the edge mode with an electric dipole source inside the slab at the interface and at the "B"-point frequency. The 3D simulation cell for the field profiles is made of several unit cells and PML boundary conditions is applied in all boundaries.

a negligible γ_B for the mode below the light line (point B), whereas a finite leakage γ_A is present for the mode lying above the light line (point A). Figures 2.10(b) and 2.10(c) show the electric field distribution corresponding to the point B in Fig. 2.10(a). Out-of-plane confinement is guaranteed by the mode's presence below the light line.

2.6 Summary

In summary, we have introduced a new kagome-like photonic topological insulator emulating the optical analogue of the quantum valley Hall effect. We have numerically shown that the associated topological edge modes do not intrinsically suffer from back-scattering for tailored inclinations. For $\Gamma-K$ inclination, the coupling between pseudo-spin channels is shown to be negligible while edge modes are guaranteed in the centre of the bandgap. It can be shown further that these modes also exhibit a certain degree of robustness against bends with arbitrary angles and weak disorders as long as the field overlap of the modes belonging to different valleys is negligible [17, 21]. Based on our theoretical predictions, we have presented a realistic 3D design that can be fabricated with state-of-the-art methods [71], and works at suitable wavelengths for telecommunication applications. We have demonstrated improved vertical confinement due to edge modes lying below the light line. The simplicity of the proposed design structure due to its monodisperse rods/holes makes it possible to fabricate it using many conventional techniques such as selective-area epitaxy or electron-beam patterning. We have also shown that possible challenges resulting from the low filling ratio can be overcome by tuning the perturbation making the bandgap of about 100 nm wide at telecommunication wavelengths. Complementing previous work with kagome lattices [83], we have provided an in-depth analysis by explaining the reason for possible back-reflection translated in the transmission spectra and analysing the out-of-plane loss in 3D realistic design.

Chapter 3

Topological insulator laser using valley Hall photonic crystals

3.1 Introduction

Transplanting the concept of topological phase transitions in fermionic systems to photonics has recently attracted enormous interest [3, 4, 84]. In contrast to conventional photonic defect states that are sensitive to perturbations, edge states from two topologically distinct regions in PTIs are robust against local perturbations and immune to backscattering [6–26]. This could lead to intriguing and remarkable photonic devices and functionalities for robust electromagnetic wave transport and processing [58, 85–87].

In addition to passive PTIs systems, a lot of attention has been made towards the study of non-Hermitian PTIs by engaging edge states with optical non-linearity to enable topological lasing. In contrast to the conventional laser technologies, which are generally sensitive to cavity deformations caused by fabrication imperfections and fluctuations, topological insulator laser cavities are potentially immune to certain cavity defects with higher lasing efficiency attributed to the unique characteristics of non-trivial edge states. A topological insulator laser was first experimentally reported in magneto-optical photonic crystals pumped by a static magnetic field to break time-reversal symmetry [31]. Although this approach allows non-reciprocal lasing from topological cavities of arbitrary geometries, it produces a narrow topological bandgap due to weak magneto-optic effect in the optical regime. Non-magnetic topologi-

cally protected edge-mode lasing was later proposed and implemented by non-trivial semiconductor ring resonator arrays, and high-efficiency single-mode lasing that is robust to cavity defects/disorders was reported [36, 37]. The one-dimensional SSH Hamiltonian model is another popular approach to generating edge states and various types of SSH lasing devices have been recently demonstrated based on micro-ring resonators [34, 35] [Chap. 1], semiconductor pillar arrays [88], and photonic crystal nanocavities [89, 90]. A topological laser arising from the valley Hall edge state was theoretically suggested [84] and an electrically pumped topological laser with valley edge modes was first experimentally achieved in the terahertz regime using quasi-hexagonal photonic crystals [91].

In this chapter, we propose a new kind of all-dielectric photonic topological lasers in the telecommunication region based on kagome valley Hall photonic crystals (KVPs) that consist of a hexagonal lattice with primitive cells containing three nano-holes in a compound semiconductor membrane. We first start looking at the presence of the topological edge state at telecommunication wavelengths. The topological waveguide obtained from topologically distinct KVPs is then used to construct a triangular cavity. The lasing dynamics of the topological cavity by means of a four-level two-electron model are explored in the last section.

3.2 Topological waveguide

The proposed all-dielectric topological strategy is based on a hole array KVPs in a high refractive index InGaAsP membrane, which has a hexagonal lattice with primitive cells composed of three nanoholes with identical diameters D, as schematically depicted in Fig. 3.1(a). As shown in Chap. 2, perturbation to retrieve non-trivial KVPs can be introduced by putting the three nanoholes closer (negative perturbation) or further away (positive perturbation) from each other. When the hole-to-centre spacing d equals to $d_0 = a/2\sqrt{3}$, the KVPs are typical kagome photonic crystals with C_{6v} symmetry featuring a Dirac cone at the K and K$'$ points in the momentum space. When we in-

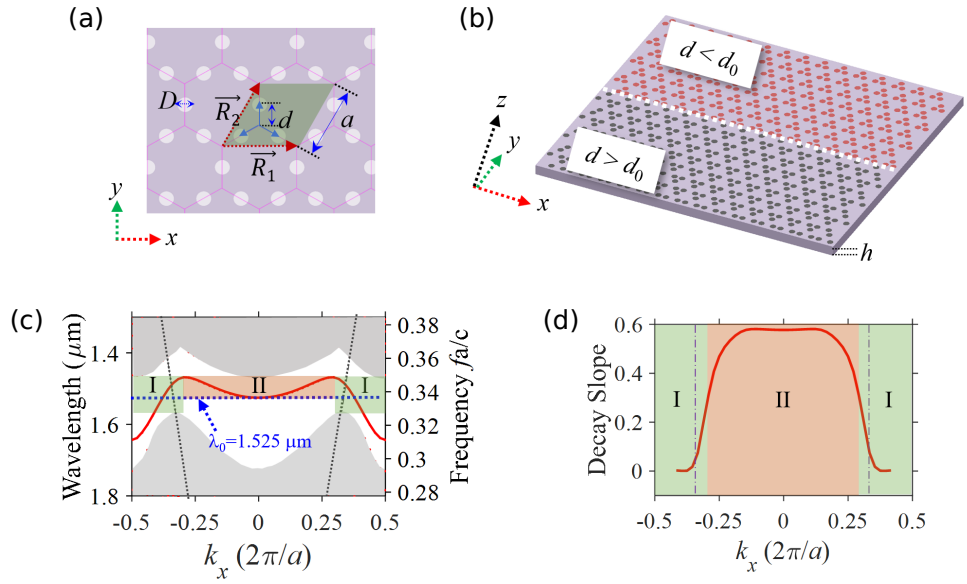

Figure 3.1: (a) Schematic of the top view of the KVPs indicating the primitive cell that contains three holes with unit vectors of $\boldsymbol{R_1}$ and $\boldsymbol{R_2}$ and lattice constant length of a. (b) Schematic of the topological waveguide made of positive and negative perturbed KVPs. The positive and negative perturbation occurs at spacing $d > d_0$ and $d < d_0$, respectively, with $d_0 = a/2\sqrt{3}$. (c) Projected band structure of the topological waveguide in (b). The black dotted lines represent the light lines, and the blue parallel dotted line shows edge mode wavelength $\lambda_0 = 1.525\,\mu\text{m}$ at $k_x = 0$. The band structure has been obtained with Bloch PBCs on the (xy)-plane, PML boundary conditions in the z-directions and an air spacer layer between the slab and the PML. (d) Decay slope of the edge states of the topological waveguide. The purple perpendicular dashed lines indicate the wave vector at which the light lines and the edge dispersion curve cross. The KVPs have lattice constant $a = 500\,\text{nm}$, hole diameter $D = 150\,\text{nm}$, and a slab height $h = 170\,\text{nm}$. The unperturbed KVPs has $d = d_0 = 144\,\text{nm}$, while the positively and negatively perturbed KVPs have $d = 1.1d_0$ and $d = 0.9d_0$, respectively. The refractive index of InGaAsP material is 3.3 and the material dispersion has been neglected [77] in the calculation of the band structure.

troduce a positive perturbation by varying $d = d_0$ to $d = 1.1d_0$ or a negative perturbation by varying $d = d_0$ to $d = 0.9d_0$, the inversion symmetry is broken and the lattice symmetry is reduced to the C_{3v} symmetry. As a result, the degeneracy at the K (and K′) point is lifted and a bandgap opens. The positively (negatively) perturbed KVPs have a positive (negative) valley Chern number [see Chap. 2]. Thereby edge states are guaranteed at the interface between them.

Thanks to the bulk-edge correspondence, we can achieve topological edge states at the boundary between the KVPs with positive and negative pertur-

bation as shown in Fig. 3.1(b). The band structure [Fig. 3.1(c)] numerically calculated using *Lumerical FDTD solutions* [82], a FDTD solver, reveals that edge states with wavelengths, ranging from 1.468 µm to 1.578 µm, are generated within a photonic bandgap. Moreover, the edge states at wavelengths ranging from 1.500 µm to 1.578 µm are below the light line, thus guaranteeing broadband topologically protected light propagation with out-of-plane confinement.

It is worth noting that the edge states can be categorised into two regions: region I ($v_p v_g \leq 0$) and region II ($v_p v_g > 0$), where v_p and v_g are the phase velocity and group velocity, respectively. The wavelengths of the two regions overlap from 1.468 µm to $\lambda_0 = 1.525$ µm within the photonic bandgap. We observe from Fig. 3.1(c) that when the edge mode wavelength is longer than λ_0, only the single unidirectional edge modes within the region I can be excited at each wavelength with propagation in the $\pm x$-direction. However, when the edge mode wavelength is shorter than (or equal to) λ_0, dual unidirectional edge modes (one in region I and the another in region II) can be excited at each wavelength with propagation in the $\pm x$-direction. The above interesting features have not been demonstrated by the valley Hall photonic crystals based on kagome lattices reported in Ref. [26, 92]. Figure 3.1(d) demonstrates that the edge modes below the light line in region I have a smaller decay slop than the others because of lower vertical light loss.

Similarly to the 2D analysis done in Chap. 2, we investigate the unidirectional propagation feature of the edge states in KVP waveguide in 3D, as schematically depicted in Fig. 3.2(a). Figure 3.2(b) shows that the same sources at different structure positions can excite unidirectional edge states propagating in the opposite direction due to chiral light-matter interaction [92], which is also observed in other reported photonic spin Hall systems [11, 13, 14] and photonic valley Hall systems [24, 25]. When a left-handed circularly polarised source excites photons at locations "1" ("2"), negative (positive) chirality is predominant and leftward (rightward) unidirectional light propagation occurs. At location "3", the local electric fields of the edge mode are elliptically polarised and hence the light propagates in both left and right directions [78, 92]. In any case, the light is well confined at the boundary between

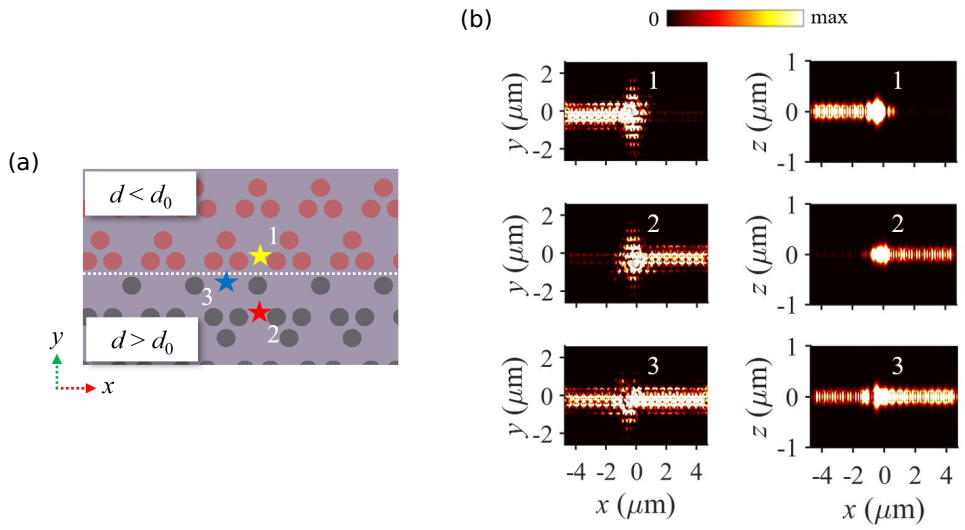

Figure 3.2: (a) Positions of the left-handed circular polarised dipoles (marked as star symbols) near the interface between the negatively and the positively perturbed KVPs. The white dotted line indicates the boundary between the negatively and the positively perturbed KVPs. (b) Field distribution $|E|^2$ of the edge mode at $\lambda = 1.550\,\mu$m in the (xy) and (xz) planes for the different source positions in (a). The geometric parameters are the same as in Fig. 3.1.

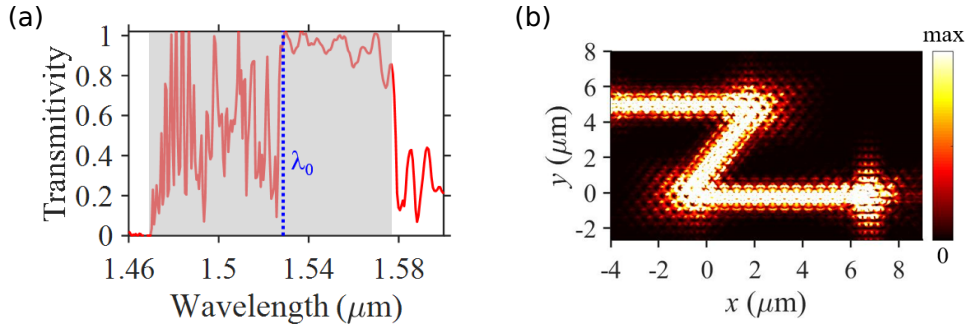

Figure 3.3: (a) Transmission spectra of the Z-shaped waveguide obtained by normalising the transmission with respect to the transmission of the straight waveguide. (b) Field distribution $|E|^2$ at $\lambda = 1.550\,\mu$m along the Z-shaped topological waveguide. The shaded area indicates the wavelength range of the bandgap. The 3D full-wave simulations have PML boundary conditions in all the x-, y-, and z-directions. The geometric parameters are the same as in Fig. 3.1.

the two perturbed KVPs in both the (xy) and (xz) planes due to the presence of the topological edge states below the light line. The modes in both region I and region II are excited [as predicted in Fig. 3.1], and the intensity of the excited modes in the two regions varies significantly with wavelength under the same dipole source excitation.

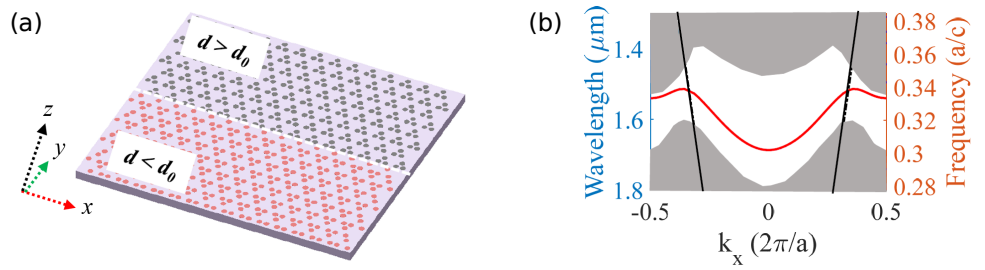

Figure 3.4: (a) Schematic of the topological waveguide made of positive and negative perturbed KVPs. (b) Projected band structure of the topological waveguide in (a). The solid black lines represent the light lines. The band structure has been obtained with Bloch PBCs on the (xy)-plane, PML boundary conditions in the z-direction and an air spacer layer between the slab and the PML. The geometric parameters are the same as in Fig. 3.1 except for the perturbation value that is reversed.

The transmission spectrum of the Z-shaped waveguide normalised by the transmission of the straight waveguide with the same geometrical parameters is plotted in Fig. 3.3(a). We can see a wavelength range where the transmission is close to 1. This confirms that the excited topologically protected light mode indeed propagates smoothly around sharp bends with high transmission. Because of the simulations done in 3D, any transmission below 1 is representative of some back-reflection or out-of-plane loss at the bendings. Besides, spectral oscillations happen at wavelengths shorter than $\lambda_0 = 1.525\,\mu\text{m}$ because of mode mixing and dual unidirectional propagation coming from region I and region II. The field profile of the mode propagating along the Z-shaped topological waveguide at wavelength $\lambda = 1.550\,\mu\text{m}$ is shown in Fig. 3.3(b).

3.3 Topological cavity

Based on the developed KVP scheme, we design a triangular topological cavity with 120-degree bends that consists of negatively perturbed KVPs inside the cavity and positively perturbed KVPs outside the cavity, as depicted in Fig. 3.5(a). If the cavity is arranged in an opposite manner, i.e. the interior of the cavity is the positively perturbed KVPs while the exterior is the negatively perturbed KVPs, then the interface is different than in Fig. 3.1 and the majority of the edge states lie above the light line [Fig. 3.4].

The proposed topological cavity supports two types of resonator modes:

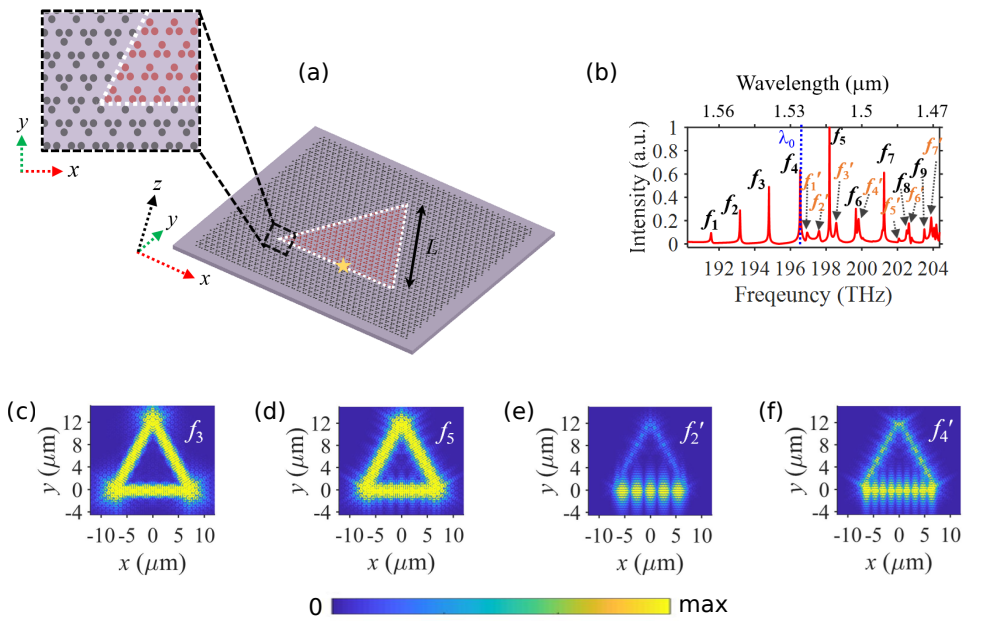

Figure 3.5: (a) Schematic of the topological cavity, and a zoomed-in on the bottom-left cavity corner area. The red and black areas represent the negatively and positively perturbed KVPs, respectively, and the white dotted lines indicate the boundary between them. The star symbol indicates the location where the dipole sources are placed to excite the cavity modes. (b) Optical spectrum of the KVP cavity with a cavity edge length of $L = 14.5\,\mu\text{m}$. (c),(d) Field distribution $|E|$, in the $z = 0\,\mu\text{m}$ plane, of the topological ring resonator modes at frequencies of $f_3 = 194.8\,\text{THz}$ ($\lambda_3 = 1.540\,\mu\text{m}$) and $f_5 = 198.2\,\text{THz}$ ($\lambda_5 = 1.513\,\mu\text{m}$), respectively. (e),(f) Field distribution $|E|$, in the $z = 0\,\mu\text{m}$ plane, of the FP resonator modes at frequencies of $f_2' = 197.6\,\text{THz}$ ($\lambda_2 = 1.518\,\mu\text{m}$) and $f_4' = 199.8\,\text{THz}$ ($\lambda_4 = 1.501\,\mu\text{m}$), respectively. The 3D full-wave simulations have PML boundary conditions in all the x-, y-, and z-directions. The geometrical parameters are the same as in Fig. 3.1.

ring resonator modes and Fabry-Pérot (FP) resonator modes. Using a cavity edge length $L = 14.5\,\mu\text{m}$ and electrical dipoles placed randomly near one of the cavity edges (see the star symbol in Fig. 3.5) to excite all the resonant modes, we observe in Fig. 3.5(b) nine ring resonator modes with frequencies of f_i ($i = 1, 2, \ldots 9$) and seven FP resonator modes with frequencies of f_m' ($m = 1, 2, \ldots 7$). The ring resonator modes arise from the excitation of the low propagation loss edge modes within region I [Figs. 3.1(c) and 3.1(d)]. This is evidenced by the E-field distributions in Figs. 3.5(c) and 3.5(d) showing that the light propagates smoothly along the whole cavity. In contrast to the ring resonator modes, the FP resonator modes experience high reflection from the cavity corners as seen in Figs. 3.5(e) and 3.5(f). The FP resonator modes

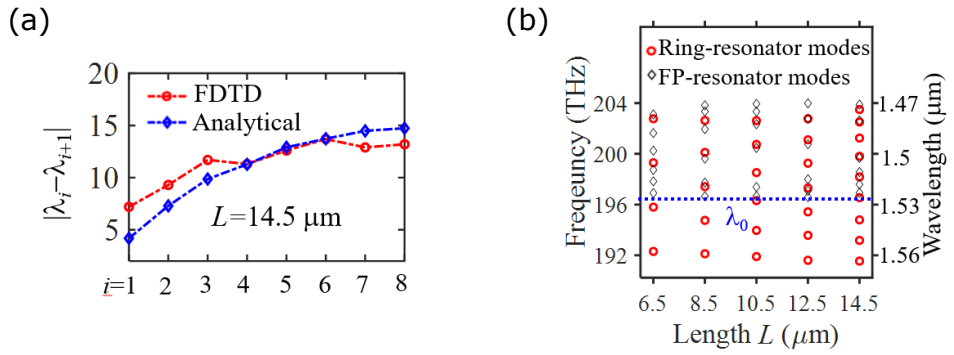

Figure 3.6: (a) Numerically and analytically obtained FSR of the ring resonator modes for a cavity edge length $L = 14.5\,\mu\text{m}$. (b) Dependence of the frequencies of the resonant modes on cavity length. The geometrical parameters are the same as in Fig. 3.1.

originate from the excitation of the lossy edge modes in region II [Figs. 3.1(c) and 3.1(d)], which explains why the wavelengths of the FP resonator modes are shorter than λ_0 in Fig. 3.5(b).

However, one should note that for the ring resonator modes displayed, both the left and right counter-propagating topological edge modes are excited. This results in standing wave patterns in Figs. 3.5(c) and 3.5(d) where interference fringes are observed.

The resonant modes can be further analysed. The cavity modes are studied by performing free-spectral-range (FSR) calculations of the ring resonator modes based on [93]:

$$\Delta\lambda_{\text{FSR}} = \frac{\lambda^2}{n_g L_{\text{cavity}}}, \tag{3.1}$$

where λ is the light wavelength, $n_g = c\partial k/\partial\omega$ is the group index obtained from the bandstructure in Fig. 3.1 and L_{cavity} is the effective length of light propagating in the cavity. Here c is the velocity of light, k the wavenumber and ω the angular frequency of light. The length of the edge of the cavity is chosen similar to Fig. 3.5, *i.e.* $L = 14.5\,\mu\text{m}$. The numerically calculated FSR results are obtained from FDTD results using:

$$\Delta\lambda_{\text{FSR,FDTD}} = |\lambda_i - \lambda_{i+1}|\,, \tag{3.2}$$

where λ_i, $i = 1, 2, \ldots 8$, are the wavelengths of the i-th ring resonator modes. Figure 3.6(a) shows that there is a discrepancy between the analytically and

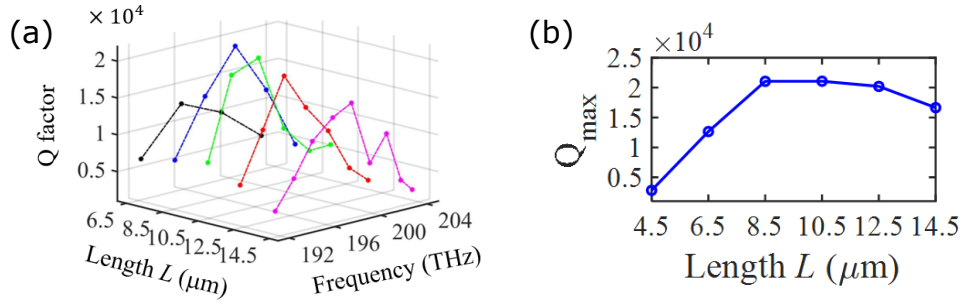

Figure 3.7: (a) Dependence of the ring resonator modes' Q factor on the cavity length L. (b) The maximum Q factor ($Q_{\max}$) of the edge modes against the cavity length L. The geometrical parameters are the same as in Fig. 3.1.

the numerically obtained FSR. This arises from the fact that we approximate $L_{\text{cavity}} = 3L$ in the numerical analysis. In fact, L_{cavity} should change with the wavelength, since different ring resonator modes have slightly different field profiles around the cavity corners and thus yield different effective length L_{cavity}. Besides, we note that the value of the FSR of the ring resonator modes is not constant because of the waveguide dispersion, namely n_g varies with the wavelength. We further study, in Fig. 3.6(b), the dependence of the cavity length on the frequencies of the resonant modes. The frequency spacing of the ring resonator modes decreases with L. We note that the FP resonator modes always appear at wavelengths shorter than $\lambda_0 = 1.525\,\mu\text{m}$, which confirms that the physical origin of FP resonator modes is coming from the excitation of the edge modes in region II [Figs. 3.1(c) and 3.1(d)].

The Q factor is also studied for this type of topological cavity. It is defined by [94, 95]:

$$Q = \frac{2\pi n_g}{\alpha\lambda}, \tag{3.3}$$

where n_g, α and λ are the group index, propagation loss and resonant wavelength of the edge mode, respectively. Using the same simulation setup as in Fig. 3.5, time monitors are randomly placed near the cavity edges to record the electric field. The logarithmic slope of the envelope of the decaying light signal in the cavity is extracted, and the Q factor is derived by averaging the obtained slopes from all the monitors. We stress that estimating the Q factor of the cavity is valid only when the size of the surrounding PhCs is large enough to confine the field of the edge modes near the cavity edges. When the size of

the surrounding PhCs is small, light leakages to the surrounding occurs and introduces additional optical loss, and hence estimation of the Q factor will not be correct. Figure 3.7(a) shows that for the same cavity length, the ring resonator modes at the frequencies in the sides of the edge states range tend to have smaller Q factors than those at the frequencies in the middle of the edge states range. This is because the modes that are closer to the bulk modes have larger lateral losses. We observe that the maximum Q factor reaches $Q = 2.1 \times 10^4$ at wavelength $\lambda = 1.518\,\mu\text{m}$ ($f = 197.4\,\text{THz}$) when the cavity edge length is $L = 8.5\,\mu\text{m}$. The proposed cavity has a higher Q factor than that of the recently reported topological ring resonator cavity based on the photonic quantum spin hall effect [16]. We demonstrate in Fig. 3.6(b) that the maximum Q factor depends on the cavity length and decreases rapidly when $L < 8.5\,\mu\text{m}$. This is due to couplings of the light in the cavity edges when the size of the cavity becomes too small. We also note that the maximum Q factor starts to slightly decrease when the cavity length increases ($L > 8.5\,\mu\text{m}$). This is a numerical artefact because of the large simulation cell required and the surrounding of the cavity being too close to the PML in (xy)-plane.

3.4 Topological laser cavity

We study the lasing performance of the topological cavity by introducing gain to the InGaAsP material and by optically pumping the topological cavity [Fig. 3.8]. In order to investigate the lasing dynamics of the cavity, we utilised the four-level two-electron model based on a 3D FDTD method implemented in *Lumerical* [96]. Figure 3.8(a) illustrates how the dynamics of the electron transition and the population density are modelled in the four-level system by considering two coupled dipole oscillators P_a (formed by level 1 and level 2) and P_b (formed by level 0 and level 3) with an angular frequency of ω_a and ω_b, and a dephasing rate γ_a and γ_b, respectively. The dipoles are assumed to be linearly polarised. The transition dipole moments are also assumed to be equal in the x-, y- and z-components with the polarisation field components being independent to each other, and given by $\mu_a = \sqrt{6\hbar\pi\epsilon_0 c^3/2\omega_a^3\tau_{21}}$ and

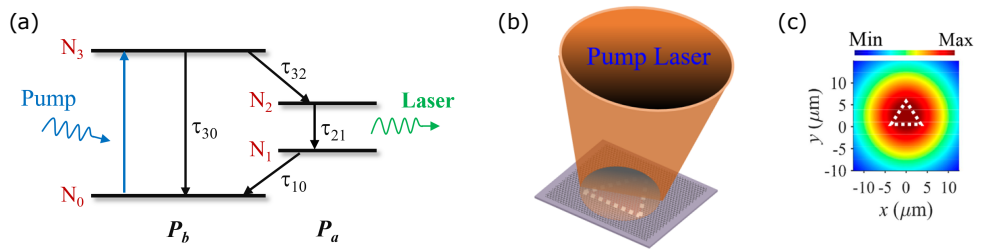

Figure 3.8: (a) Schematic diagram of the four-level two-electron model used to modelled the gain in the active material. N_i is electron population density probability in level i and τ_{ij} $(i, j = 0, 1, 2, 3)$ are the decay time constant between levels i and j. The gain parameters for the InGaAsP material in the model are $\omega_a = 1260\,\text{THz}$, $\omega_b = 1770\,\text{THz}$, $\gamma_a = 168\,\text{THz}$, $\gamma_b = 1\,\text{THz}$, $\tau_{30} = \tau_{21} = 300\,\text{ps}$ and $\tau_{32} = \tau_{10} = 0.1\,\text{ps}$ [96,97], which give $\mu_a = 6.28 \times 10^{-28}\,\text{C m}$, $\mu_b = 3.77 \times 10^{-28}\,\text{C m}$. (b) Schematic of the cavity that is optically pumped by another laser from the top. (c) Spatial intensity profile of the Gaussian source directed along the z-direction with waist radius of 12 µm and at $z = 1\,\mu\text{m}$ above the cavity. The Gaussian source is linearly polarised along the x-direction. The white dotted line represents the outline of the cavity edges.

$\mu_b = \sqrt{6\hbar\pi\epsilon_0 c^3/2\omega_b^3\tau_{30}}$, with ϵ_0 and c being the permittivity and speed of light in vacuum [96]. The system is then selectively pumped with a narrow linewidth that is centred on the transition frequency ω_b. The angular frequencies chosen for the InGaAsP material are here set to $\omega_a = 1260\,\text{THz}$ ($\lambda_a = 1.495\,\mu\text{m}$) and $\omega_b = 1770\,\text{THz}$ ($\lambda_b = 1.064\,\mu\text{m}$) [96, 97]. A continuous-wave laser with a Gaussian shape intensity profile [Fig. 3.8(b)] at wavelength $\lambda = 1.064\,\mu\text{m}$ is used to pump the KVP cavities to excite the topological laser modes in the telecommunication region. The Gaussian source is placed at $z = 1\,\mu\text{m}$ away from the cavity surface and has a waist radius of 12 µm in order to pump both the inside and outside of the cavities [Fig. 3.8(c)].

The electron population density of the levels relies on the stimulated and spontaneous emission decay. Lasing is achieved once population inversion between level 1 and level 2 is realised, from which the stimulated emission is the dominant process. As an example, we simulate a topological cavity with an edge length of $L = 6.5\,\mu\text{m}$. Figure 3.9(a) shows that the laser intensity ($|E_x|^2 + |E_y|^2 + |E_z|^2$) recorded at the bottom-left corner experiences a dramatically jump when the power of the pump laser increases to a certain threshold value, and then the laser intensity becomes saturated when the pump laser intensity further increases. This is a typical laser behaviour which indicates a transition

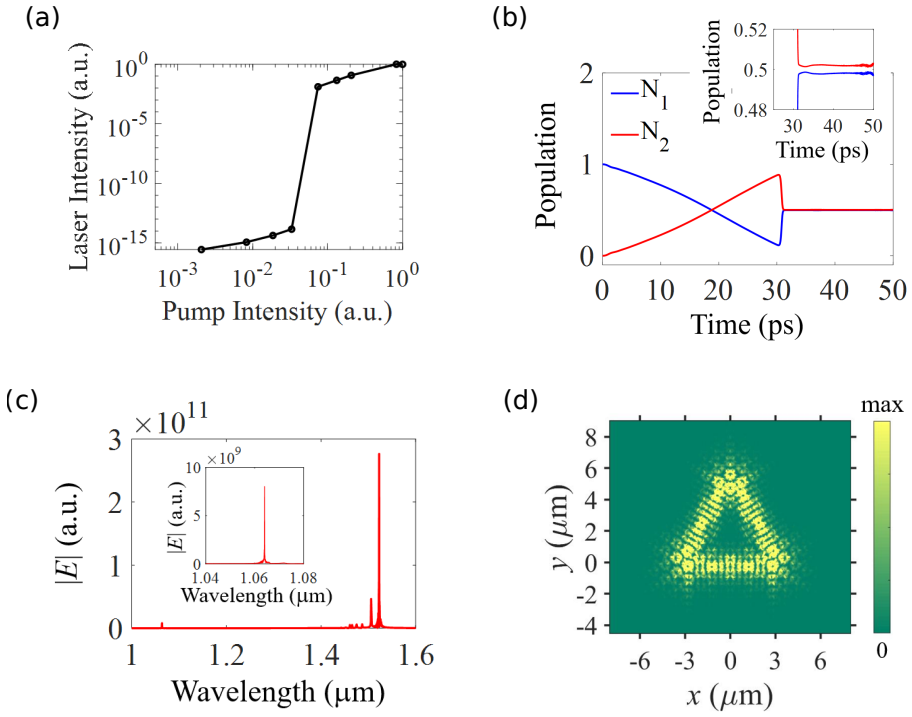

Figure 3.9: (a) Normalised output laser intensity versus normalised pump laser intensity with 1 corresponding to a pump amplitude of $|E| = 3 \times 10^5\,\mathrm{V/m}$. (b) Time evolution of the electron population density N_1 and N_2 of the level 1 and 2, respectively. The inset shows the population inversion when the lasing is stabilised. (c) Spectrum of the KVP laser at a pump amplitude of $|E| = 3 \times 10^5\,\mathrm{V/m}$. The inset is the spectrum of the pump laser at $\lambda = 1.064\,\mu\mathrm{m}$. (d) Lasing field distribution $|E|$ in the $z = 0\,\mu\mathrm{m}$ plane of the topological cavity at $\lambda = 1.523\,\mu\mathrm{m}$ in (c). The 3D full-wave simulations have PML boundary conditions in all the x-, y-, and z-directions. The cavity edge length in the simulations is $L = 6.5\,\mu\mathrm{m}$ and the other geometrical parameters are the same as in Fig. 3.1. The gain parameters are the same as in Fig. 3.8.

from dominant spontaneous emission to dominant stimulated emission. We demonstrate in Fig. 3.9(b) that the population inversion of level 2 relative to level 1 can indeed be achieved with a pump laser amplitude of $|E| = 3 \times 10^5\,\mathrm{V/m}$. Consequently, lasing at edge state $\lambda \simeq 1.523\,\mu\mathrm{m}$ is achieved, as shown from the laser spectrum and the field distribution in Figs. 3.9(c) and 3.9(d). The field profile looks slightly different to that in Fig. 3.5(c) because they are corresponding to different modes at different wavelengths. Similarly to Fig. 3.5, the lasing mode in Fig. 3.9(d) displays standing wave patterns because both counter-propagating edge modes are lasing.

We now investigate the robustness of the proposed topological laser cavity. We design a topological cavity with a complex closed boundary between

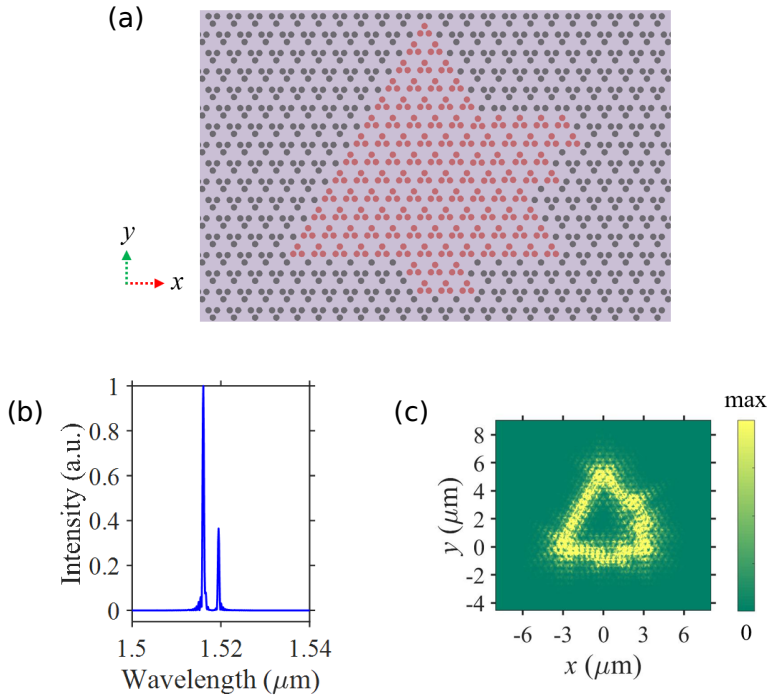

Figure 3.10: (a) Schematic top-view of the cavity with a complex geometry. The red and black regions indicate the negatively and positively perturbed KVPs, respectively. (b) Spectrum of the laser cavity in (a) at a pump amplitude of $|E| = 3 \times 10^5\,\mathrm{V/m}$. (c) Field distribution $|E|$ of the edge mode laser at wavelength $\lambda = 1.516\,\mu\mathrm{m}$ in (b). The 3D full-wave simulations have PML boundary conditions in all the x-, y-, and z-directions. The geometrical parameters of the cavity are the same as in Fig. 3.1 except for the cavity shape and length. The gain parameters are the same as in Fig. 3.8.

the perturbed KVPs as depicted in Fig. 3.10(a). Despite the complex cavity geometry, distinct topological invariants of the two perturbed KVPs ensure the existence of topological modes, and the generated laser is well confined and propagates smoothly along the boundary [Fig. 3.10(c)] as long as there is no inter-valley mixing. The cavity has a different cavity length to that in Fig. 3.9 and hence generates resonant edge modes with different wavelengths. The lasing at the resonant mode wavelength $\lambda = 1.516\,\mu\mathrm{m}$ is dominant, which we think is due to this mode having higher gain and lower loss than the other resonant modes from the same cavity.

We note from Fig. 3.9(c) and Fig. 3.10(b) that multiple lasing modes are excited, which is due to the fact that we use a relatively large value of dephasing rate γ_a in our design so that the gain of the material covers a broad wavelength range of edge states. As a result, when the pump laser power is strong enough,

additional ring resonator modes start to lase as well.

3.5 Summary

In summary, we have demonstrated a PTI strategy based on an all-dielectric hole-type kagome lattice. One advantage of the developed KVPs in the semiconductor membrane platform is that it allows broadband non-trivial generation in the telecommunication region below the light line and thus enables robust photonic routing in waveguides even with sharp bends. We analytically and numerically investigate the bandstructure of the kagome photonic crystals and show that the valley-dependent edge states can be categorised into two regions, *i.e.* region I ($v_p v_g \leq 0$) and region II ($v_p v_g > 0$), where v_p and v_g are phase velocity and group velocity, respectively. Edge modes in region I have low propagation loss and are topologically protected while the edge modes in region II have high propagation loss and suffer from inter-valley mixing. This results in the coexistence of the topological ring resonator modes and the trivial Fabry–Pérot resonator modes in the proposed triangular-type KVP cavities. We study the proposed topologically protected laser cavity based on the four-level two-electron model and evaluate the robustness and dynamics of the lasing cavities by studying the population inversion, the lasing spectra, the field profile of the lasing modes, and the light-in light-out (L-L) responses. To date, tight-binding models are widely used to design and analyse gain and lasing behaviours of topological insulator lasers [36, 37]. Our work suggests that the FDTD-based four-level two-electron model offers a powerful alternative platform to study laser performances of topological insulator cavities with arbitrary geometry. Our study will help to understand the interplay between non-Hermiticity and topology, and more importantly provides a new scheme to explore compact all-dielectric topological lasers that can be easily integrated into other passive or active photonic devices by the well-established semiconductor photonic integrated circuit technologies.

Chapter 4

Topological bulk lasing modes using an imaginary gauge field

4.1 Introduction

In an attempt of controlling the flow of light, PTIs [4] have enabled exciting devices such as unidirectional waveguides and topological lasers that are robust against a certain class of perturbations and defects. In particular, the realisation of robust topological optical systems has drawn attention for advanced photonic by reducing propagation loss in optical devices [57, 92], for quantum computers [98, 99], photonic neural networks [100] and near-zero epsilon devices [101–103].

Recently, considerable effort has been made to study non-Hermitian PTIs by engaging topological edge modes to enable a lasing regime with optical non-linearity [34, 37], distribution of gain and loss [33, 35, 104–106] or non-reciprocal couplings [31, 38, 39]. For example, the 1D SSH model [32] has been utilised to generate edge states with gain/loss and implement topological lasing devices [33–35]. A cavity made of topologically distinct PTIs has been proposed to enhance the lasing efficiency by using unidirectional topologically protected edge modes [31, 106].

However, the edge-mode-based topological lasers are not appropriate for high power lasers due to the localised nature of the edge modes and the possible breakdown of the constituting optical elements. As an alternative, topological bulk lasers have been proposed to achieve broad-area emission by using ex-

tended topological modes based solely on the parity symmetry at the Γ-point in a 2D hexagonal cavity [38] or by using an imaginary gauge field in a 1D $\mathcal{PT}$-symmetric SSH lattice to delocalise the zero-energy boundary mode over the 1D bulk [39]. Although the spatial stability, *i.e.* robustness, of the topological lasing mode is guaranteed based on topological band theory, its temporal behaviour is not necessarily stable due to the non-linear nature of the optical gain in lasers [42]. Therefore the temporal instability can further deteriorate the performance of lasing devices and it becomes important to study the dynamics and the temporal stability of the topological lasing modes [107].

In this chapter, we generalise the topological extended mode on the 1D SSH [39] lattice to higher-dimensional lattices. In particular, we demonstrate a topological extended mode on a 2D bulk by using a kagome lattice with a rhombus geometry and by using non-reciprocal couplings modelled by a complex imaginary gauge field. The topological bulk laser is studied with an alternating gain and loss distribution. Using the laser rate equations, we show that the topological extended mode lases and has large stable regions in its parameter space. We thus demonstrate that a phase-locked broad-area topological laser can be realised in a 2D kagome lattice.

4.2 Extended topological mode in a 1D lattice

Here, we briefly recall the procedure used to delocalise the topologically protected (zero-energy) mode in the SSH lattice in Ref. [39].

The SSH lattice, depicted in Fig. 4.1(a), is a 1D lattice made of an array of N_s sites. It has a unit cell composed of two sites (A and B) and the lattice is characterised by alternating intra- and inter-unit cell couplings given by the real scalars t_1 and t_2, respectively.

In the non-Hermitian configurations, where an extended mode has been proposed [39, 108], a purely complex imaginary gauge potential, $\boldsymbol{\mathcal{A}} = -ih\boldsymbol{e_1}$, h real, is introduced. In the presence of the gauge field, the Peierl's phase modifies the hopping terms by a factor: $e^{i\int \boldsymbol{\mathcal{A}}\cdot\boldsymbol{dl}}$, with $\boldsymbol{dl} = dx_i\boldsymbol{e_i}$ the direction of the hopping. The couplings are therefore modified and become asymmetric.

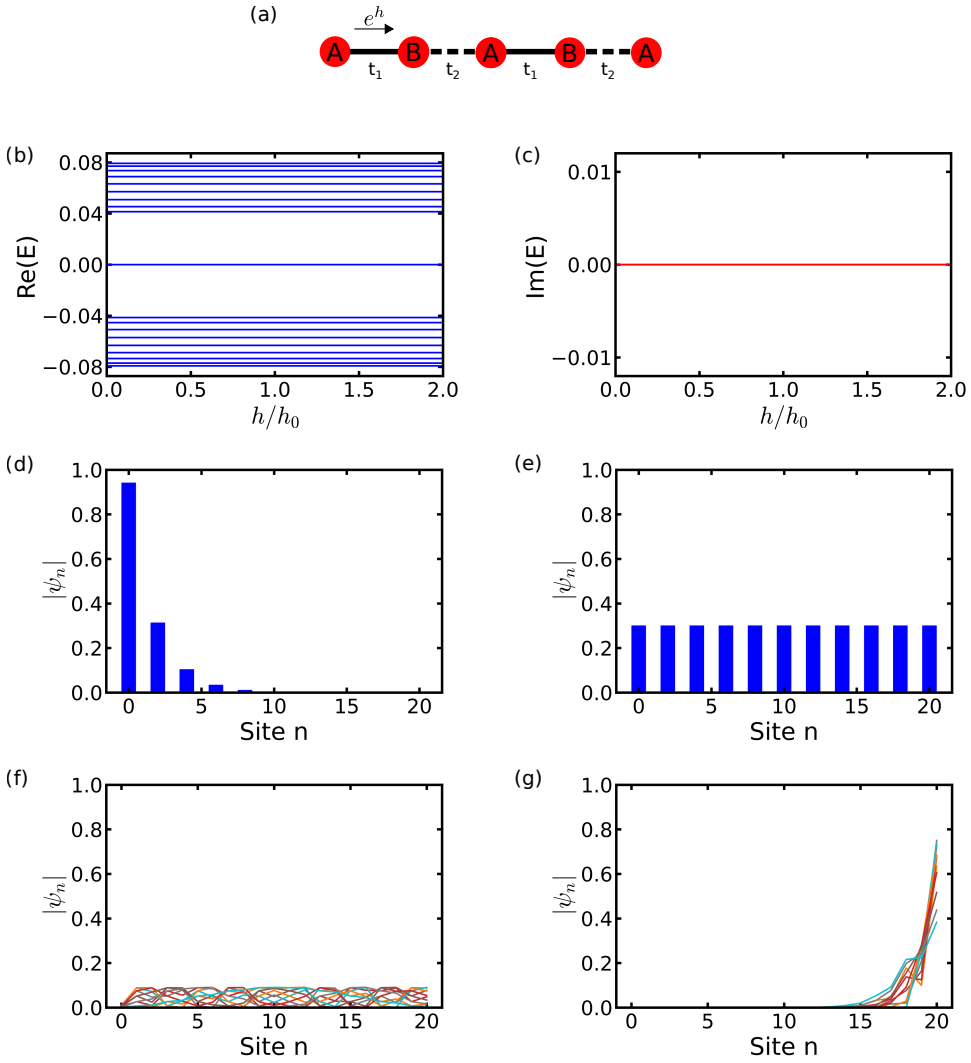

Figure 4.1: (a) Schematic of a non-Hermitian SSH finite-size lattice made of an array of N_s sites. The lattice starts from a site A and terminates at a site A. The usual Hermitian SSH lattice corresponds to the case where $h = 0$. (b),(c) Real and imaginary parts of the spectrum of the finite-size SSH lattice against the non-Hermitian term h, respectively. (d),(e) Normalised field profile $|\psi_n|$ of the zero-energy mode from the finite-size SSH lattice in the Hermitian ($h = 0$) and non-Hermitian ($h = h_0$) settings, respectively. (f),(g) Normalised field profile $|\psi_n|$ of all the non-zero-energy (bulk) modes from the finite-size SSH lattice in the Hermitian ($h = 0$) and non-Hermitian ($h = h_0$) settings, respectively. The colours correspond to the different modes. The parameter are chosen such that $N_s = 19$, $E_A = E_B = 0$, $t_1 = 0.02$, $t_2 = 0.06$.

Note that the usual pre-factors are here absorbed in $\boldsymbol{\mathcal{A}}$, or equivalently in h. The coupling constants get a e^h factor term when hopping from left to right, and a e^{-h} factor term when hopping from right to left. The coupled-mode

equations are then written as:

$$i\frac{da_n}{dt} = E_A a_n + t_1 e^{-h} b_n + t_2 e^{h} b_{n-1}, \tag{4.1}$$

$$i\frac{db_n}{dt} = E_B b_n + t_1 e^{h} a_n + t_2 e^{-h} a_{n+1}, \tag{4.2}$$

with a_n and b_n the modal amplitudes on the A and B sites at the n-th unit cell, respectively. E_σ is the on-site energy on the site $\sigma = A, B$.

For a finite system, the introduction of the imaginary gauge field will not affect the spectrum [108] as shown in Figs. 4.1(b) and 4.1(c). This can be made explicit by noting that the system of equations above can be solved with a suitable gauge transformation:

$$a_n = e^{2hn}\tilde{a}_n, \tag{4.3}$$

$$b_n = e^{2hn}e^{-2h}\tilde{b}_n \tag{4.4}$$

where a_n and b_n are solutions of the coupled-mode equations if $\tilde{a}_n$ and $\tilde{b}_n$ are solutions of the Hermitian SSH coupled-mode equations, namely when $h = 0$.

For a SSH lattice starting and terminating on an A site, it is known that the zero-energy mode of the Hermitian SSH lattice reads:

$$\tilde{a}_n = \tilde{r}^n \tilde{a}_0, \tag{4.5}$$

$$\tilde{b}_n = 0, \tag{4.6}$$

where

$$\tilde{r} = -\frac{t_1}{t_2} \tag{4.7}$$

is defined by

$$\tilde{a}_{n+1} = \tilde{r}\tilde{a}_n \tag{4.8}$$

and satisfies the destructive interference condition on the B sites

$$t_1 + \tilde{r}t_2 = 0. \tag{4.9}$$

The solution for the non-Hermitian SSH lattice is then written as:

$$a_n = r^n a_0, \tag{4.10}$$

$$b_n = 0, \tag{4.11}$$

where

$$r = -\frac{t_1}{t_2} e^{2h} \tag{4.12}$$

is defined as

$$a_{n+1} = r a_n \tag{4.13}$$

and satisfies the modified destructive interference condition on the B sites

$$t_1 e^{h} + r t_2 e^{-h} = 0. \tag{4.14}$$

The main effect of this imaginary gauge field is to change the localisation property of the modes without affecting the spectrum [Figs. 4.1(b) and 4.1(c)]. In particular, one can delocalise the topologically protected edge mode over the whole 1D bulk, while keeping its topological protection from the chiral symmetry of the Hermitian topologically protected (zero-energy) mode. The exponentially increasing or decaying factor is removed by appropriately choosing the gauge field h such that $|r| = 1$:

$$h = h_0 := -\frac{1}{2} \ln \left(\frac{t_1}{t_2} \right). \tag{4.15}$$

Figures 4.1(b) and 4.1(c) show that the spectrum of the finite-size Hermitian and non-Hermitian SSH lattice are indeed unchanged as we turn on the non-Hermitian term h. However, for $t_1 < t_2$, the field profile $|\psi_n|$ of the zero-energy mode is localised on the left edge for the Hermitian case [Fig. 4.1(d)], while it is extended over the 1D bulk for the non-Hermitian case with $h = h_0$ [Fig. 4.1(e)]. In addition to the zero-energy mode, the field profiles of the bulk modes are also modified [Figs. 4.1(f) and 4.1(g)]. For $t_1 < t_2$, and thus $h > 0$, they become localised on the right edge of the lattice: this is known as the (non-Hermitian) skin effect. This alteration of the bulk modes is one of the reasons why the bulk-edge correspondence breaks down in non-Hermitian systems [27]

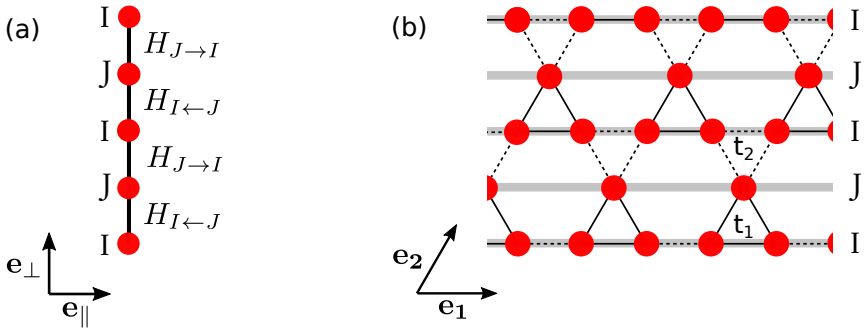

Figure 4.2: (a) Schematic of a d-dimensional lattice in a quasi-1D lattice made of an array of N_s $(d-1)$-dimensional lattices. (b) Schematic of the kagome lattice drawn in the quasi-1D lattice formalism. The solid and dashed lines denote the intra-cell (t_1) and inter-cell couplings (t_2), respectively.

and justify the importance to do the analysis in the open boundary conditions as mentioned in Chap. 1.

Finally, it is worth noting that although the zero-energy mode is topologically protected, its localisation property depends locally on the coupling constants, and is therefore sensitive to their perturbations. However, for reasonably small perturbations, *i.e.* small enough so that the bandgap does not close, the delocalisation is not destroyed: the amplitudes remain at the same order of magnitude over the bulk but are simply not equal anymore [see for example Fig. 4.6(f)].

4.3 Extended topological mode in a d-dimensional lattice: example on the kagome lattice

We now generalise this notion of delocalised (or extended) topological mode over a whole d-dimensional bulk.

4.3.1 General framework

The strategy follows similar steps as in the previous section, namely to find an exact solution of the (topologically protected) boundary state, and then use non-Hermiticity to change the localisation property of the chosen mode.

In order to find an exact solution, we follow the procedure in Ref. [109,110]. One needs to consider a d-dimensional lattice as a stack of $(d-1)$-dimensional

lattices ($\boldsymbol{e}_{\parallel}$-direction) and with OBCs in the remaining one-dimensional ($\boldsymbol{e}_{\perp}$-direction) boundaries [109–111] [see Fig. 4.2 for the example of the kagome lattice]. The lattice can then be considered as a quasi-1D lattice with the unit cell composed of two lattice-sites, I and J, except that here the lattice-sites represent $(d-1)$-dimensional lattices, as shown in Fig. 4.2. Additional conditions are assumed such as the quasi-1D lattice needs to start and terminate on the same I lattice-site, and we forbid direct hopping between the I lattice-sites [109, 110, 112]. Therefore, the lattice naturally supports the exact disappearance of the modal amplitude of n modes on the J lattice-sites, with n the number of degrees of freedom on the I lattice-site.

From the quasi-1D formalism, the coupled-mode equation is conveniently written as:

$$i\frac{d\Psi}{dt} = H_{\text{lattice}}\Psi \tag{4.16}$$

where $\Psi = (\psi_{I,0}, \psi_{J,0}, \ldots, \psi_{I,N})^T$ with $\psi_{I,n}$ and $\psi_{J,n}$ being the modal amplitudes on the I and J lattice-sites in the n-th stacked unit cell, respectively. N is the index of the last unit cell. The Hamiltonian of the lattice reads:

$$H_{\text{lattice}} = \begin{pmatrix} H_I & H_{I\leftarrow J} & 0 & \cdots \\ \tilde{H}^{\dagger}_{I\leftarrow J} & H_J & \tilde{H}^{\dagger}_{J\rightarrow I} & \cdots \\ 0 & H_{J\rightarrow I} & H_I & \cdots \\ \vdots & \vdots & \vdots & \ddots \end{pmatrix} \tag{4.17}$$

with H_I and H_J being the Hamiltonian of the lattice I and J, respectively. $H_{I\leftarrow J}$ and $H_{J\rightarrow I}$ are $(N_s \times N_s')$-matrices, and correspond, respectively, to the intra- and inter-unit cell couplings between the I and J lattices. N_s and N_s' are the number of sites in the I and J lattices, respectively. For the Hermitian case, we have $\tilde{H}^{\dagger}_{I\leftarrow J} = H^{\dagger}_{I\leftarrow J}$ and $\tilde{H}^{\dagger}_{J\rightarrow I} = H^{\dagger}_{J\rightarrow I}$.

For the general d-dimensional lattice, the eigenvalue problem $H_{\text{lattice}}\Psi = E\Psi$ yields, for $n = 0, \ldots, N$:

$$H_{I,k}\psi_{I,n} + H_{I\leftarrow J}\psi_{J,n} + H_{J\rightarrow I}\psi_{J,n-1} = E\psi_{I,n}, \tag{4.18}$$

$$H_{J,k}\psi_{J,n} + \tilde{H}^{\dagger}_{I\leftarrow J}\psi_{I,n} + \tilde{H}^{\dagger}_{J\rightarrow I}\psi_{I,n+1} = E\psi_{J,n}. \tag{4.19}$$

The condition for destructive interference on the J-lattices, $\psi_{J,n} = 0$, is given

by:

$$\tilde{H}^{\dagger}_{I\leftarrow J}\psi^{(i)}_{I,n} + \tilde{H}^{\dagger}_{J\rightarrow I}\psi^{(i)}_{I,n+1} = 0. \tag{4.20}$$

From Eq. 4.18, the solution with vanishing amplitude on the J-lattice therefore gives the additional condition:

$$H_I\psi_{I,n} = E\psi_{I,n}, \tag{4.21}$$

namely $\psi_{I,n}$ must be an eigenmode of the Hamiltonian on the lattice I, labelled $\psi^{(i)}_{I,n}$, with corresponding energy $E = E^{(i)}_I$.

Since we are looking at edge states, we can ask for solutions which exponentially decay or increase, or equivalently solutions that satisfy [109, 111]:

$$\psi^{(i)}_{I,n+1} = r_i\psi^{(i)}_{I,n} \tag{4.22}$$

with r_i being a scalar term representing the decaying amplitudes of the mode inside the quasi-1D lattice.

The boundary state solution of the Hamiltonian H_{lattice} with energy $E^{(i)}_I$ is therefore of the form:

$$\psi^{(i)}_{I,n} = r_i^n\psi^{(i)}_{I,0} \tag{4.23}$$

with r_i satisfying the destructive interference condition on the J lattice:

$$\tilde{H}^{\dagger}_{I\leftarrow J}\psi^{(i)}_{I,0} + r_i\tilde{H}^{\dagger}_{J\rightarrow I}\psi^{(i)}_{I,0} = 0. \tag{4.24}$$

In summary, the modes with eigenenergy $E = E^{(i)}_I$, such that $H_I\psi^{(i)}_I = E_I\psi^{(i)}_I$, are the modes which are exponentially localised on one edge and with non-vanishing amplitudes only on the lattice-sites I, with mode distribution corresponding to $\psi^{(i)}_I$ on the lattice-site I.

The delocalisation of the edge modes is then realised by introducing an imaginary gauge field such that $|r_i| = 1$. The non-Hermitian terms allow the change of the localisation properties while keeping the spectrum unchanged.

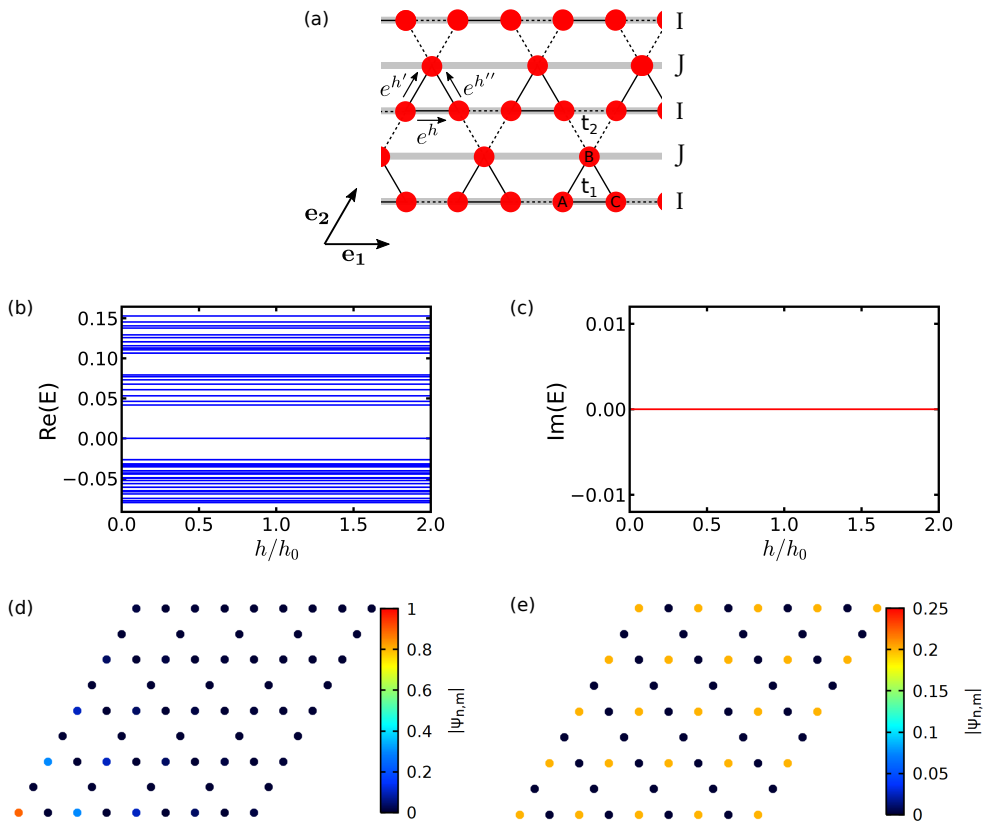

Figure 4.3: (a) Schematic of the kagome lattice in the non-Hermitian setting. e^{h}, $e^{h'}$, $e^{h''}$ correspond to the imaginary gauge field introduced for delocalising the topological mode. (b),(c) Real and imaginary parts of the spectrum of the kagome lattice in the rhombus geometry against the non-Hermitian term h, respectively. (d),(e) The normalised field profile $|\psi_{n,m}|$ of the zero-energy mode of the kagome lattice in the rhombus geometry in the Hermitian ($h = h' = h'' = 0$) and non-Hermitian setting ($h = h' = h_0$, $h'' = 0$), respectively. Here, there are $N_s = 9$ sites both in the I lattice and the quasi-1D lattice. $t_1 = 0.02$, $t_2 = 0.06$.

4.3.2 Extended topological mode in 2D kagome lattice

As a concrete example, we will look at the case of the kagome lattice as shown in Fig. 4.3(a). Additional examples, such as the Lieb and the 2D SSH lattices, are given in Sect. 4.5. The kagome lattice is characterised by a unit cell composed of three sites A, B, and C and the coupling strengths between sites are different for intra-unit cell (t_1) and inter-unit cell (t_2) couplings.

We will specifically look at the topological zero-energy corner mode present in the rhombus geometry of the kagome lattice [113–115] [see Fig. 4.3(d) for the geometry of the lattice]. Figure 4.3(c) plots the normalised field distribution $|\psi_{n,m}|$ of the zero-energy mode for $t_1 < t_2$. This shows that the mode is

localised on the bottom-left corner, with vanishing amplitudes on the B and C sites, as explained later.

Applying the previous quasi-1D formalism to the kagome lattice in the rhombus geometry, we have $H_I = H_{\mathrm{SSH}}$, $H_J = \mathrm{diag}(E_B, \ldots, E_B)$. The coupling matrices are given by:

$$\tilde{H}^{\dagger}_{I\leftarrow J} = H^{\dagger}_{I\leftarrow J} = \begin{pmatrix} t_1 & t_1 & 0 & \ldots & \ldots & \ldots \\ \ldots & 0 & t_1 & t_1 & 0 & \ldots \\ \ldots & \ldots & \ldots & \ldots & \ldots & \ldots \\ \ldots & \ldots & \ldots & \ldots & 0 & t_1 \end{pmatrix} \tag{4.25}$$

and

$$\tilde{H}^{\dagger}_{J\rightarrow I} = H^{\dagger}_{J\rightarrow I} = \begin{pmatrix} t_2 & 0 & \ldots & \ldots & \ldots & \ldots \\ 0 & t_2 & t_2 & 0 & \ldots & \ldots \\ \ldots & \ldots & \ldots & \ldots & \ldots & \ldots \\ \ldots & \ldots & \ldots & 0 & t_2 & t_2 \end{pmatrix}. \tag{4.26}$$

The rhombus geometry is interesting since in the $\boldsymbol{e}_{\parallel}$-direction, the I lattices, which are equivalent to the SSH lattice, start with and are terminated by the same site (here site A). In this configuration, we can see the zero-energy corner mode is related to the topological zero-energy mode present in the chiral symmetric SSH lattice. The zero-energy corner mode can be seen as the boundary state of the kagome lattice with eigenenergy $E_I^{(i)} = E_I^{(0)} = 0$ and can be analytically written as [110]:

$$\psi^{(0)}_{I,m} = r^m_{0,2}\psi^{(0)}_{I,0} \tag{4.27}$$

with

$$\left[\psi^{(0)}_{I,0}\right]_n = r^n_{0,1}a_{0,0} \tag{4.28}$$

being the n-th component of the zero-energy mode $\psi^{(0)}_{I,0}$ of the SSH lattice, and $a_{n,m}$ the modal amplitude on the A site at the n-th unit cell in the m-th lattice I. The interference conditions [Eq. 4.24] give:

$$r_{0,1} = -\frac{t_1}{t_2} \tag{4.29}$$

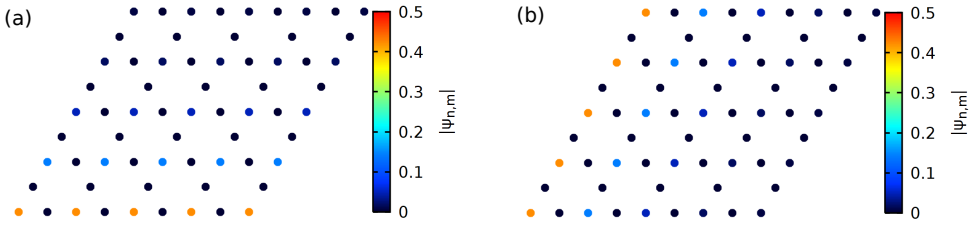

Figure 4.4: Normalised field profile $|\psi_{n,m}|$ of the zero-energy mode of the kagome lattice in the rhombus geometry with (a) $h = h_0$, $h' = h'' = 0$ and (b) $h' = h_0$, $h = h'' = 0$. The other parameters are the same as in Fig. 4.3.

and

$$r_{0,2} = -\frac{t_1}{t_2}. \tag{4.30}$$

As expected, the analytical expression shows that by choosing different intra- and inter-unit cell coupling constants, $t_1 < t_2$ or $t_1 > t_2$, the zero-mode is exponentially localised, respectively, on the bottom-left or upper-right edge of the SSH lattice with vanishing amplitudes on the B and C sites.

We now use an imaginary gauge field to change the localisation property of this corner mode [39, 108]. Figure 4.3(a) sketches the gauge potential considered where e^h, $e^{h'}$ and $e^{h''}$ represent the phase factor in the couplings between the sites A and B, A and C, and B and C, respectively. Conditions on h, h' and h'' are imposed given an imaginary gauge field $\boldsymbol{\mathcal{A}} = (\mathcal{A}_1, \mathcal{A}_2)$. From the Peierls' phase corresponding to e^h we have $\mathcal{A}_1 = -ih$, with $\boldsymbol{dl} = \boldsymbol{e_1}$. Similarly, $e^{h'}$ gives $\mathcal{A}_2 = -ih'$, using $\boldsymbol{dl} = \boldsymbol{e_2}$. These two conditions on $\boldsymbol{\mathcal{A}}$ mean that for $e^{h''}$ we must have:

$$h'' = -h + h' \tag{4.31}$$

where $\boldsymbol{dl} = \boldsymbol{e_2} - \boldsymbol{e_1}$. With the imaginary gauge field, the coupling matrices are then modified, and particularly we have:

$$\tilde{H}^{\dagger}_{I\leftarrow J} = \begin{pmatrix} t_1 e^{h'} & t_1 e^{h''} & 0 & \dots & \dots & \dots \\ \dots & 0 & t_1 e^{h'} & t_1 e^{h''} & 0 & \dots \\ \dots & \dots & \dots & \dots & \dots & \dots \\ \dots & \dots & \dots & \dots & 0 & t_1 e^{h'} \end{pmatrix} \tag{4.32}$$

and

$$\tilde{H}^{\dagger}_{J\to I} = \begin{pmatrix} t_2 e^{-h'} & 0 & \dots & \dots & \dots & \dots \\ 0 & t_2 e^{-h''} & t_2 e^{-h'} & 0 & \dots & \dots \\ \dots & \dots & \dots & \dots & \dots & \dots \\ \dots & \dots & \dots & 0 & t_2 e^{-h''} & t_2 e^{-h'} \end{pmatrix}. \tag{4.33}$$

The interference conditions now yield:

$$r_{0,1} = -\frac{t_1}{t_2} e^{2h} \tag{4.34}$$

and

$$r_{0,2} = -\frac{t_1}{t_2} e^{2h'}. \tag{4.35}$$

Delocalisation over the $\boldsymbol{e_1}$-direction is achieved by requiring $|r_{0,1}| = 1$, namely choosing $h = h_0$. Similarly, delocalisation over the $\boldsymbol{e_2}$-direction is realised with $h' = h_0$ so that $|r_{0,2}| = 1$. One can notice that there is no further condition on h'' to delocalise the mode in the quasi-1D lattice. This is because of the vanishing amplitudes on the B and C sites. Figures 4.4(a) and 4.4(b) show the normalised field profile $|\psi_{n,m}|$ of the zero-energy mode using $h = h_0$, $h' = h'' = 0$ and $h' = h_0$, $h = h'' = 0$, respectively. In Fig. 4.4(a), the mode is localised on the bottom edge while being extended over the $\boldsymbol{e_1}$-direction. On the other hand, Fig. 4.4(b) shows that the mode is localised on the left edge while being extended along the $\boldsymbol{e_2}$-direction. It is worth noting that for the values of h, h' and h'' chosen for drawing Fig. 4.4, the spectrum is not identical to the Hermitian case since the condition on the gauge field [Eq. 4.31] is not satisfied.

Provided Eq. 4.31 holds, the introduction of the imaginary gauge field will only affect the localisation property of the mode while keeping the spectrum unchanged [Figs. 4.3(b) and 4.3(c)]. Therefore, in this case, the condition $|r_{0,i}| = 1$ does not correspond to the band touching between the edge band and the bulk band [109], and thus the topological is retained. Combining the two results obtained above for the delocalisation of the zero-energy mode and

the restricting condition on the gauge field [Eq. 4.31], we can choose:

$$h = h' = h_0 := -\frac{1}{2}\ln\left(\frac{t_1}{t_2}\right) \tag{4.36}$$

and

$$h'' = 0 \tag{4.37}$$

to completely delocalise the topological corner mode over the bulk of the kagome lattice. Figures 4.3(b) and 4.3(c) show that the numerically calculated spectrum of the kagome lattice in the rhombus geometry does not change when the imaginary gauge is introduced. Nevertheless, Figure 4.3(c) plots the normalised field distribution of the zero-energy mode using $h = h' = h_0$ and $h'' = 0$, and shows that the topologically protected zero-energy mode is now extended over the whole bulk of the kagome lattice: we have obtained a topological bulk mode in the 2D kagome lattice.

The generalisation to higher-dimensional lattices can be achieved using a similar procedure: namely starting by delocalising a topologically protected mode over a lower-dimensional bulk, and repeating this step with the higher dimension.

It is interesting to note the usefulness of this bottom-up approach presented in this section because it gives us some intuitive insight into the behaviours of the boundary states from the lower dimensional lattice. This will be used again in the next section [Sect. 4.4] when the gain and loss will be considered.

4.4 Lasing in the non-Hermitian kagome lattice

The peculiarity of this extended topological mode is its vanishing amplitudes on the B and C sites but most of all, that it is topologically protected over a 2D bulk, and has a π-phase difference between non-vanishing sites. This hints at the possibility to realise phase-locked broad-area topological lasers in 2D lattices.

4.4.1 An active and non-Hermitian kagome lattice

The design presented above can be extended to build a topological laser by considering optical pumping of semiconductor ring resonators with gain (g) and loss ($-g$) as the main sites A, B or C. The imaginary gauge field can be made using auxiliary ring resonators with different losses strength between the upper and lower half perimeter of the ring [39], as we will see in section 4.6. The values of the imaginary gauge field h, h', h'' would then mainly depend on the losses contrast by depositing lossy materials with different thicknesses on top of the auxiliary rings or using different materials [34–36, 116].

The gain and loss configuration is chosen based on the SSH sublattices since we are looking for topological modes in the kagome lattice that originate from the topological mode in the SSH sublattice. In the literature, it is well known that the SSH lattice in a $\mathcal{PT}$-symmetric configuration [33, 34] (gain on A sites, $E_A = ig$, and loss on C sites, $E_C = -ig$) can preserve the topological protection of the zero-energy. Particularly, if the SSH lattice is in the unbroken $\mathcal{PT}$-symmetric phase, *i.e.* $g/t_1 < (t_2/t_1 - 1)$, then the gap does not close in the presence of gain or loss, and the zero-energy mode remains well separated from the bulk [34, 105]. When the energy is complex, we refer to the zero-energy as the real part of the energy being zero.

Since the only non-vanishing terms of the extended topological mode are located in the A sites [as shown in Eq. 4.27 and Fig. 4.3(e)], we would like to get lasing to come from these sites. Therefore we consider gain on site A, $E_A = ig$, and lossy rings on the B and C sites, ($E_B = E_C = -ig$), as shown in Fig. 4.5(a). We observe in Figs. 4.5(b) and 4.5(c) that as long as the gain and loss strength is low enough, the zero-energy mode is well isolated and no bandgap closing occurs. Thus the topological protection remains for low gain and loss g. The gap closing occurs when $g/t_1 = (t_2/t_1 - 1)$ (here $g/t_1 = 2$) and corresponds to the transition point from unbroken $\mathcal{PT}$-symmetric to broken $\mathcal{PT}$-symmetric phase in the $\mathcal{PT}$-symmetric SSH lattice [34] [Chap. 1]. This topological transition of the zero-energy mode in the kagome lattice is in correspondence with the topological transition of the zero-energy mode in the SSH lattice since they have the same origin: the topological mode can be derived from the topological mode in the SSH lattice. Figure 4.5(b) plots

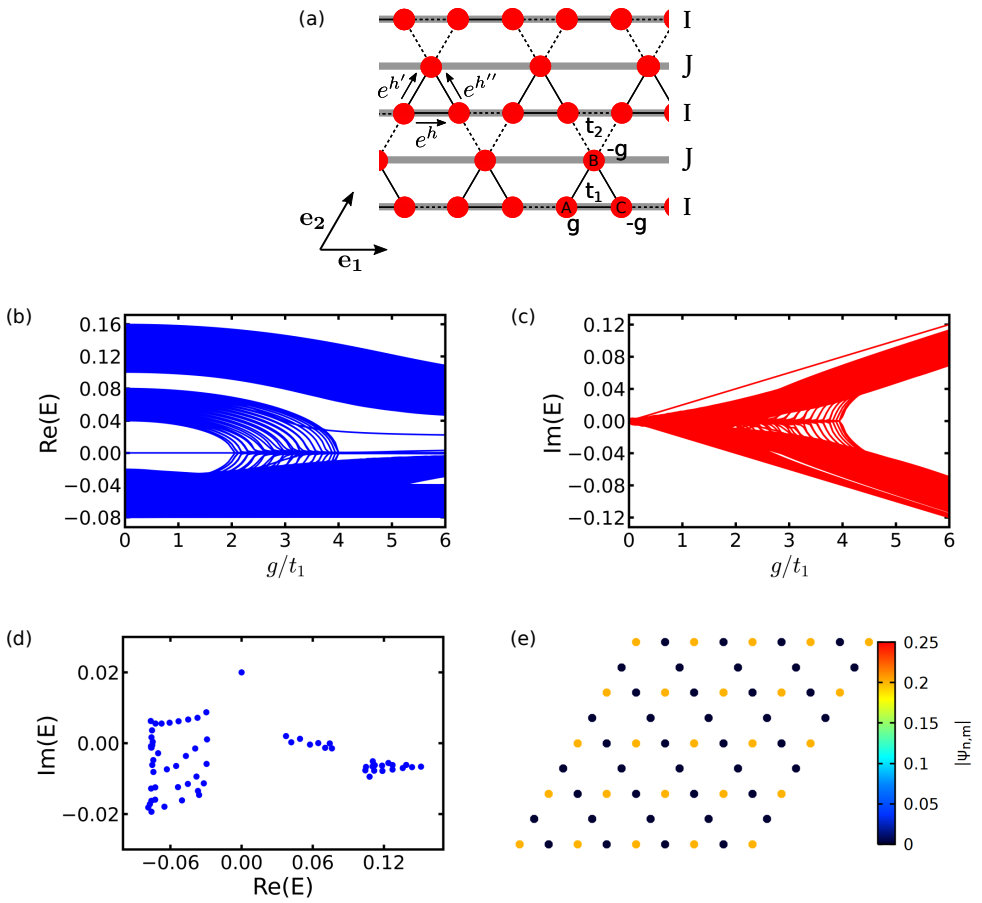

Figure 4.5: (a) Schematic of the non-Hermitian kagome lattice in the active setting. g ($-g$) is the gain (loss) considered for the laser setting. (b),(c) Real and imaginary parts of the spectrum of the kagome lattice in the rhombus geometry against the linear gain g, respectively. (d) Spectrum of the non-Hermitian active kagome lattice in the rhombus geometry for $g/t_1 = 1$. (e) The normalised field profile $|\psi_{n,m}|$ of the zero-energy mode of the non-Hermitian active kagome lattice in the rhombus geometry. We have $N_s = 29$ sites both in the I lattice and the quasi-1D lattice in (b),(c) and $N_s = 9$ in (d),(e). The coupling parameters are $t_1 = 0.02$, $t_2 = 0.06$ and $h = h' = h_0$, $h'' = 0$.

the spectrum in the complex plane and the normalised field profile $|\psi_{n,m}|$ of the zero-energy mode, numerically calculated with $E_A = ig$, $E_B = E_C = -ig$ and $g/t_1 = 1$. with $h = h' = h_0$ and $h'' = 0$. This demonstrates that the zero-energy mode is present and remains delocalised over the kagome bulk. Besides, the zero-energy mode has high gain compared to the other modes because of the gain on the A sites, *i.e.* where the zero-energy mode is non-vanishing. This shows that, for $g/t_1 < (t_2/t_1 - 1)$, the zero-energy mode is lasing and its delocalisation is not altered as well as its topological protection: we have obtained a topological bulk lasing mode in the 2D kagome lattice.

One should note that having gain only near the region where the topological edge mode is localised should be enough for the topological bulk mode to lase. Indeed, the gauge transformation relating the Hermitian and non-Hermitian kagome lattice similar to Eq. 4.3[1] suggests that the mode is mainly sensitive to the gain near the edge where the topological localised mode is present. A deeper reason is that the overlap matrix element with gain also involves the left eigenvectors which are even more localised to the edge [117]. This explains why the topological bulk mode is still mainly sensitive to gain near the edge.

However, apart from lasing, it is also important to note the importance of the gain and loss distribution in terms of the bulk excitation and their decay in time. Indeed, as we have seen in Sect. 4.2, the non-Hermitian skin effect is present due to the imaginary gauge field. The skin effect will thus be dominant in the dynamics if the loss distribution is not appropriately chosen, *i.e.* if the bulk modes do not vanish over time.

4.4.2 Temporal dynamics of the zero-energy mode

Time-domain modelling of the mode dynamics is essential for determining whether the lasing mode is stable. In the frequency analysis, we have shown it is possible to have an active non-Hermitian kagome lattice with an extended topological mode. However, the previous analysis provides only a simple physical model of the active non-Hermitian kagome lattice. Indeed, it has been shown that temporal instabilities in the laser array may prevent phase-locking and reduce the laser quality or even dominate and suppress the topological signature of the corresponding lasing mode [39, 42].

We consider the laser rate equation based on a two-level system for modelling the gain in the active rings A [39,52,118] [see Chap. 1]. Optical pumping is assumed to be small enough to leave the lossy ring resonators (rings B and C, and auxiliary rings) in the linearised regime below their threshold point. Linear losses are thus chosen, and the losses and imaginary gauge field are considered to be carrier-independent. The normalised laser rate equation in

[1] A similar expression can be found for the kagome lattice in the rhombus geometry.

the kagome lattice, with $h = h' = h_0$ and $h'' = 0$, is then given by:

$$\begin{aligned} i\frac{da_{n,m}}{dt} &= i\frac{1}{\tau_p}(1 - i\alpha_{\mathrm{H}})Z_{n,m}a_{n,m} \\ &\quad + t_1 e^{-h_0} b_{n,m} + t_1 e^{-h_0} c_{n,m} + t_2 e^{h_0} b_{n,m-1} + t_2 e^{h_0} c_{n-1,m}, \end{aligned} \tag{4.38}$$

$$\begin{aligned} i\frac{db_{n,m}}{dt} &= i(-g_B + i\delta_B)b_{n,m} \\ &\quad + t_1 e^{h_0} a_{n,m} + t_1 c_{n,m} + t_2 e^{-h_0} a_{n,m-1} + t_2 c_{n-1,m+1}, \end{aligned} \tag{4.39}$$

$$\begin{aligned} i\frac{dc_{n,m}}{dt} &= i(-g_C + i\delta_C)c_{n,m} \\ &\quad + t_1 e^{h_0} a_{n,m} + t_1 b_{n,m} + t_2 e^{-h_0} a_{n+1,m} + t_2 b_{n+1,m-1}, \end{aligned} \tag{4.40}$$

$$\tau_s \frac{dZ_{n,m}}{dt} = p_A - Z_{n,m} - (1 + 2Z_{n,m})|a_{n,m}|^2, \tag{4.41}$$

where $a_{n,m}$, $b_{n,m}$ and $c_{n,m}$ are the normalised modal amplitudes on the site A, B and C and in the (n, m)-th unit cell, respectively. n and m stand for the unit-cell index in the SSH lattice and quasi-1D lattice, respectively. $Z_{n,m}$ is the normalised excess carrier density in the active ring A, τ_p and τ_s are the photon and spontaneous carrier lifetimes, respectively, α_{H} the linewidth enhancement factor [54], p_A the normalised excess pump current in the ring A, and g_B and g_C the linear loss in the ring B and C, respectively. δ_B and δ_C are added to the equations in order to take into account possible (global) geometrical perturbation of the ring resonators with respect to the A rings.

Here we show that a broad-area and phase-locked laser can be realised. The parameters are chosen similar to Ref. [39, 52, 118] and are typical for semiconductor lasers. The coupled-mode equations are integrated using random noise of field amplitudes between $[0, 0.01]$ and equilibrium carrier density $Z_{n,m} = p_A$ as the initial condition. The random noise as initial condition is chosen to trigger non-linear behaviour and see whether or not the mode is stable. Figure 4.6(a) plots the time evolution of the instantaneous spectrum of the matrix Hamiltonian given by Eqs. 4.38-4.40 (recall Eq. 4.16), namely using the carrier density $Z_{m,n}(t)$ at given time t. This shows that after a transient time, the system reaches a single laser mode regime. The laser mode is the topological zero-energy mode with $\mathrm{Im}(E) = 0$. Figures 4.6(b) and 4.6(c) show that after a transient regime, only the zero-energy mode survives and reaches

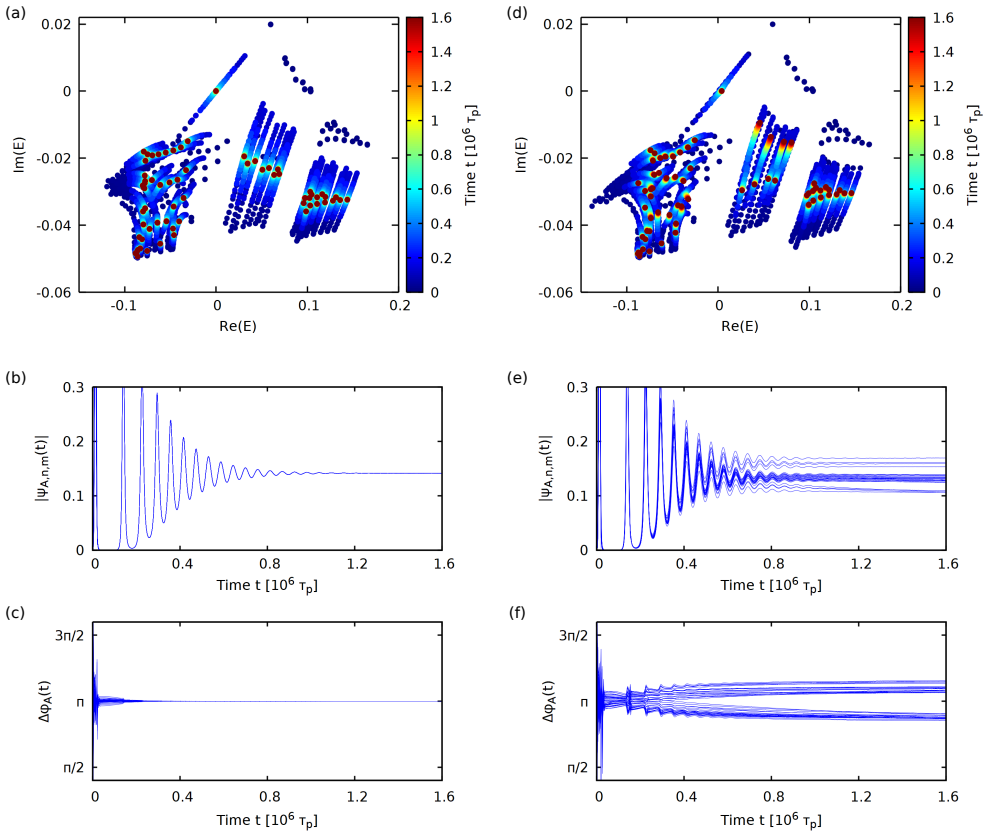

Figure 4.6: Time evolution of (a) the instantaneous spectrum of the kagome lattice in rhombus geometry (b) the amplitudes of all the A sites, and (c) the phase differences between the adjacent A sites when there is no disorder. Similarly for (d), (e) and (f) when asymmetric disorders are introduced. The parameters used are: $\tau_p = 40\,\text{ps}$, $\alpha_\text{H} = 3$, $\tau_s = 80\,\text{ns}$, $p_A = 0.02$, $g_B\tau_p = g_C\tau_p = 0.05$, $\delta_B\tau_p = \delta_C\tau_p = 0.01$, $t_1\tau_p = 0.02$, $t_2\tau_p = 0.06$.

a steady state. The amplitudes of all the A sites are equally distributed over the bulk and have a fixed π-phase difference. The laser system obtained is, therefore, broad-area and phase-locked.

The laser mode is topologically protected in addition to being broad-area and phase-locked. Figure 4.6(d) shows the spectrum of the system when a spatially varying and random asymmetric perturbation on the couplings, $\delta t_{1\pm} \in [-0.12t_1, 0.12t_1]$, is added: $t_1 e^{h} \to (t_1 + \delta t_{1+})e^{h}$ and $t_1 e^{-h} \to (t_1 + \delta t_{1-})e^{-h}$. This asymmetric perturbation accounts for perturbation in the coupling strength as well as for the imaginary gauge field. One can see that the zero-energy mode is still present. However, Figures 4.6(e) and 4.6(f) show a slightly different behaviour in the time series of the field amplitudes and the phase differences between the A rings. They do not reach the same values in

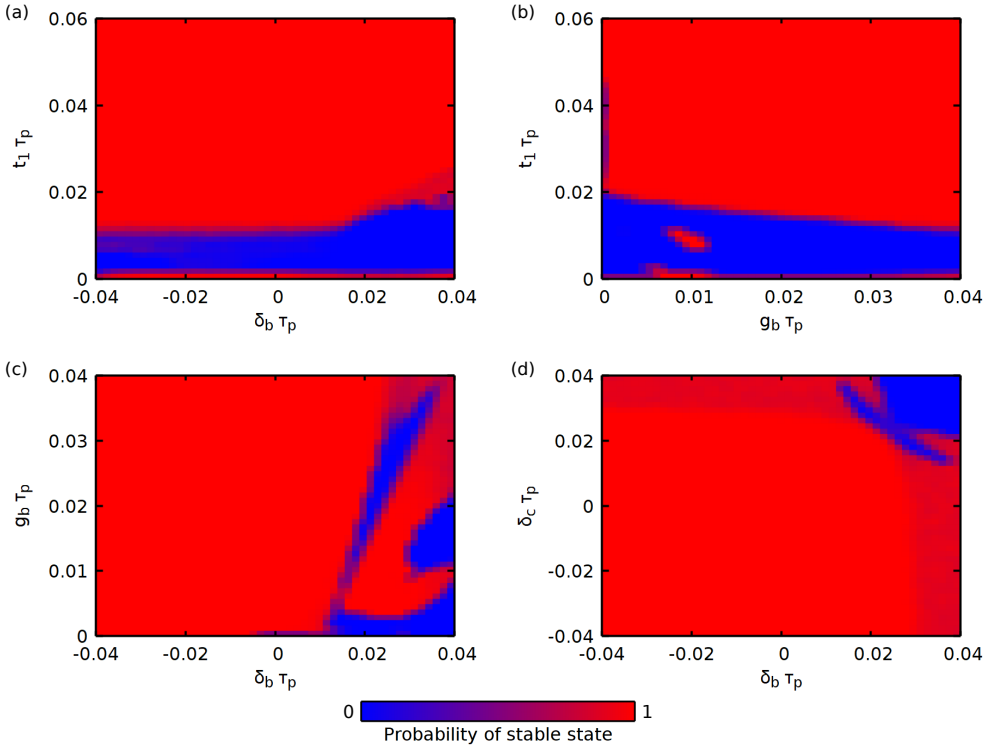

Figure 4.7: Stability diagrams of the topological extended mode. The colour corresponds to the probability of the system being in the stable regime over 200 realisations in the random initial conditions of the mode amplitudes. The fixed parameters are the same as in Fig. 4.6.

amplitudes and phase differences. The amplitudes are not equally distributed but have slightly different offsets because of the different couplings between two adjacent sites: a single choice for the imaginary gauge field h and h' cannot satisfy the $|r_{0,i}| = 1$ conditions between each sites. Similarly, the phase differences are no longer equal to π and are seen to be due to the non-linear Henry factor α_{H}. Nevertheless, here, the addition of perturbation in the coupling strengths does not give rise to unstable behaviour in the amplitudes and phases of the topological extended mode.

With the chosen parameters, the zero-energy mode shown in Fig. 4.6 does not suffer from non-linear instabilities. Indeed, the system reaches a stationary state which does not evolve into random oscillation in their amplitudes and phase differences. Even though the spatial stability of the topological mode may be guaranteed by its topological invariant, it is worth looking at its temporal stability in the parameter space to delimit the region where temporal instabilities arise due to the non-linear terms. In the following, we will refer to

the stable regime, the regime of single-mode lasing in the topological extended mode. Therefore, we say the system to be unstable (or stable) if oscillations are present (or not) in their amplitudes or phase differences.

Stable phase-locking of the non-Hermitian gauge laser array is possible in a relatively large region of the parameter space. Figure 4.7 shows the stability diagram of the topological extended lasing mode for different slices of the parameter space. The numerical results show the stability of the topological extended mode requires a minimum coupling strength [Figs. 4.7(a) and 4.7(b)]. One reason is that the $\mathcal{PT}$-symmetric phase of the SSH lattice is broken when the couplings are too small compared to the gain and loss [34]: the system is no longer in the single-mode lasing regime. The second reason is that the non-reciprocal dissipative couplings need to be high enough in order to reach a (soft) synchronisation [119]. On the other hand, instabilities arise when the detunings δ_b and δ_c are too high [Fig. 4.7(c)]. The major critical case is with positive detunings [Figs. 4.7(c) and 4.7(d)]. However, stability is retrieved if the dissipation is large enough to compensate the detunings in the rings B and C.

Extended lasing modes present an important advantage in getting a better slope efficiency, compared to the localised lasing modes. Figure 4.8(a) plots the total intensity, $I = \sum_{m,n} |\psi_{n,m}|^2$ against the pump amplitudes p_A for the localised and extended lasing modes where the colour plot corresponds to the system being in the stable or unstable regime. The numerical results show that the localised mode has lower slope efficiency compared to the extended mode. The remarkable difference is the scaling of the slope efficiency with the size of the system for the delocalised mode while it remains constant for the localised mode, as shown in the inset of Fig. 4.8(a). This is because of the extended nature of the mode whose contribution to the lasing intensity increases with the size of the system. Figure 4.8(b) shows the slope efficiency is robust against asymmetric disorder in the couplings, for both the localised and extended modes, due to the topological nature of the lasing modes. The localised mode has a relatively constant slope efficiency with increasing disorder strength. While the extended mode gives varying slope efficiency because of the varying field distribution of the extended mode in the bulk as explained

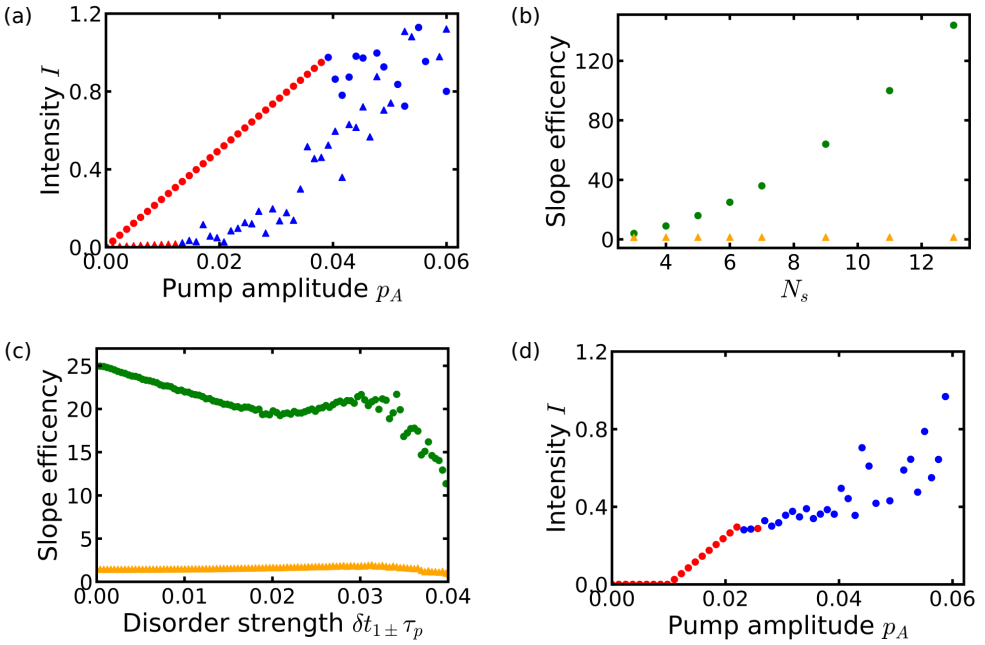

Figure 4.8: (a) Total intensity against pump amplitudes p_A for the localised and delocalised topological modes with $N_s = 9$. The triangles (circles) correspond to the topological edge (bulk) laser. The colours indicate if the system is in the unstable (blue) or stable (red) regime. (b) Slope efficiency against the size N_s of the system for the topological edge (bulk) laser in orange triangle points (green circle). (c) Slope efficiency against disorder strength $\delta t_{1\pm}$ (for $N_s = 9$). The orange triangle (green circle) points correspond to the topological edge (bulk) laser. For each disorder strength, the slope efficiency is averaged over 800 random realisations of the disorder. (d) Total intensity against pump amplitudes p_A for the topological bulk modes with $N_s = 9$ and with a background loss $\gamma_0\tau_p = 0.01$. The parameters are the same as in Fig. 4.6. Besides, panel (a)-(c) has no background loss $\gamma_0\tau_p = 0$.

before, its slope efficiency remains higher compared to the localised mode. However, for high values of disorder strength in the couplings, the slope efficiency of the extended mode starts to decrease. This is explained because the delocalisation of the topological mode, originating from non-reciprocal couplings, is highly perturbed by the asymmetric perturbation $\delta t_{1\pm}$ in the couplings: the topological mode may not be completely delocalised anymore.

It is worth noting that any background losses have been neglected, resulting in threshold-less lasers [Fig. 4.8(a)]. However, the physical elements that produce the non-reciprocal couplings might inevitably change the laser threshold. Indeed, as we will see in Sect. 4.6, the non-reciprocal couplings can be implemented by introducing additional gain and/or loss in the system that

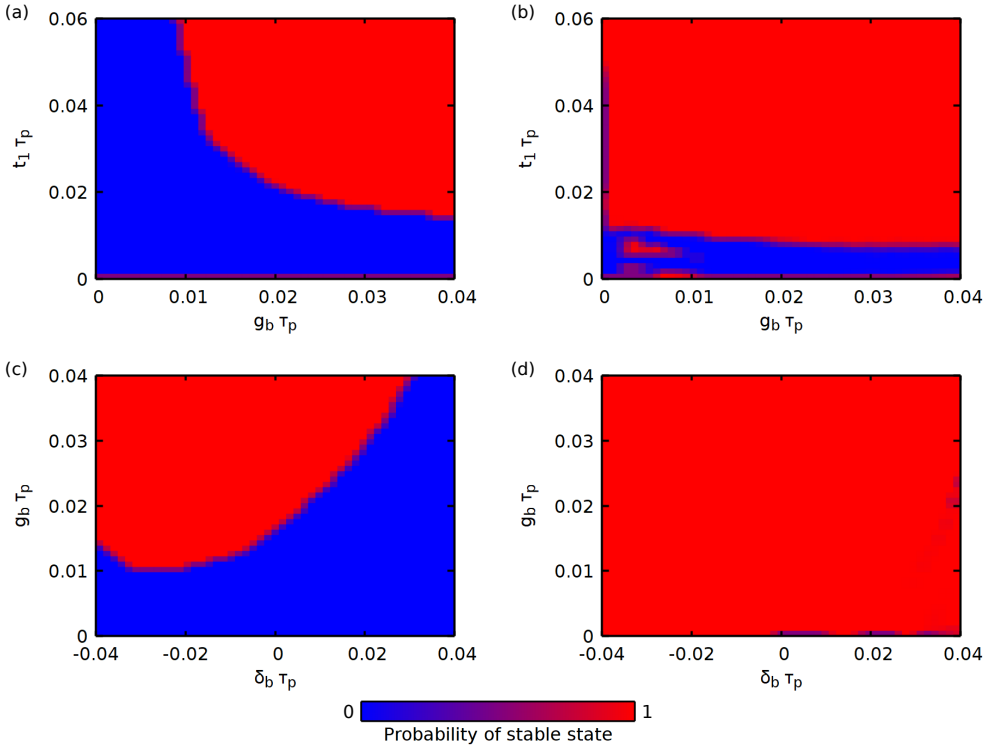

Figure 4.9: Stability diagrams of the topological (a),(c) localised and (b),(d) extended modes. The colour corresponds to the probability of the system being in the stable regime over 200 realisations in the random initial conditions of the mode amplitudes. The fixed parameters are the same as in Fig. 4.6 except here $p_A = 0.01$.

were previously hidden in the tight-binding model. By considering only additional losses in a system made of ring resonator array, the imaginary gauge field strength $h = h_0$ required for complete delocalisation can be related to an overall background loss γ_0 via Eq. 4.93: $h_0 = \alpha\eta/2$. Using Eq. 4.91, we have $\gamma_0 = 2h_0 c/\eta n_g$, where c is the speed of light, n_g the group refractive index of the ring resonator, and η the length of the additional leg of the auxiliary rings. We set $\gamma_0\tau_p = 0.01$ by controlling the length's leg η. Figure 4.8(d) then shows the total intensity I against the pump amplitude p_A from which the system has now a laser threshold at $p_A = 0.01$. Although the laser threshold value of the system changes, the slope efficiency is the same as in the absence of background loss ($\gamma_0 = 0$). Nevertheless, we can see [Fig. 4.8(d)] that the stability has now been reduced and the stability region might be reduced in the parameter space due to the additional background loss.

The imaginary gauge field helps to stabilise the system in the zero-energy

lasing mode. The extended nature of the topological mode over the bulk allows the zero-energy mode to carry all the gain of the system while suppressing all the other bulk modes. The colour plot in Fig. 4.8(a) indicates that the localised mode reaches an unstable regime for relatively low values of pump intensity whereas the extended mode is unstable for higher pump intensities. Nevertheless, the topological bulk mode survives up to a critical pump intensity before becoming unstable. From the linear gain $g_A\tau_p = p_A$ equivalent, this critical pump value is given by $p_A/t_1 \approx (t_2/t_1 - 1)$ (here $p_A = 0.04$) and corresponds to the bandgap closing in Fig. 4.5(b) and, thus, to a possible topological phase transition. This is another evidence where temporal stability is important to take into account: the localised zero-energy mode does not survive to high pump intensity even though it is guaranteed to be stable spatially from its topological properties. The stability diagrams for the localised mode are shown in Figs. 4.9(a)-4.9(c). Compared to the extended mode in Figs. 4.9(b)-4.9(d), these diagrams demonstrate that the extended mode have, indeed, larger regions of stability in the parameter space than the localised mode.

4.5 Extended topological mode in Lieb lattice and 2D SSH lattice

This section provides additional examples of the delocalisation of the boundary modes over a d-dimensional bulk: the Lieb lattice and the 2D SSH lattice.

4.5.1 Lieb lattice

We focus, here, on the anisotropic Lieb lattice [120] which is described by three sites by unit cell and intra-cell couplings (t_1, t_2) and inter-cell couplings (t_3, t_4) as shown in Fig. 4.10(a).

Specifically, we will delocalise the zero-energy corner mode present in the truncated Lieb lattice [see Fig. 4.10(b) for a sketch of the finite-size lattice]. Figure 4.10(b) plots the normalised field distribution $|\psi_{n,m}|$ of the zero-energy corner mode obtained for $t_1 < t_2$ and $t_3 < t_4$.

Applying the recipe given in above to the (Hermitian) truncated Lieb lat-

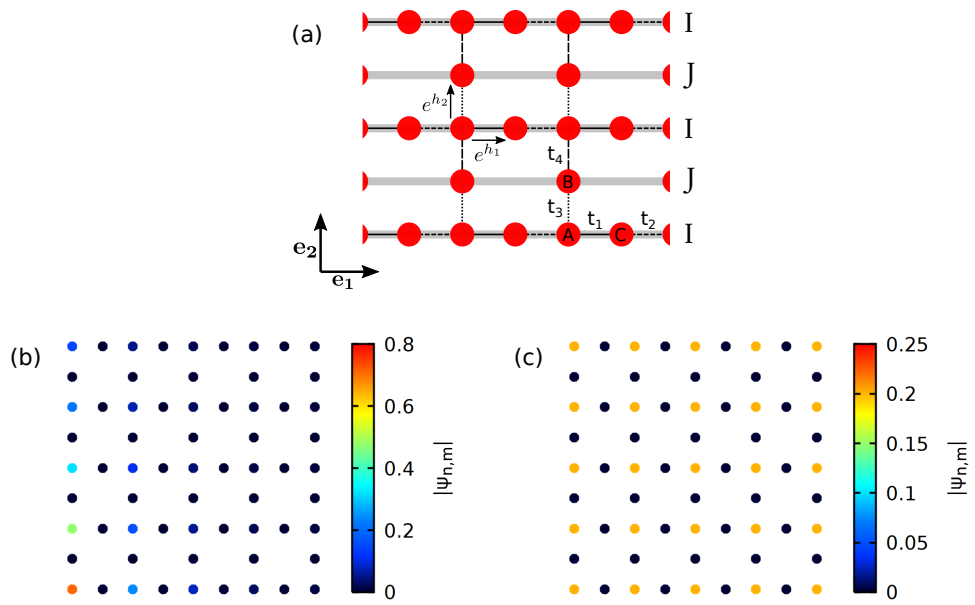

Figure 4.10: (a) Schematic of a non-Hermitian (and anisotropic) Lieb lattice drawn in the quasi-1D lattice formalism. The solid and dotted lines represent the intra-cell couplings t_1 and t_2, respectively. The short and long dashed lines denote the inter-cell couplings t_3 and t_4, respectively. e^{h_1}, e^{h_2} correspond to the imaginary gauge field. The normalised field profile $|\psi_{n,m}|$ of the zero-energy mode of the truncated Lieb lattice is plotted in (b) for the Hermitian case, and in (c) for the non-Hermitian case. Here, there are $N_s = 9$ sites both in the I lattice and the quasi-1D lattice. $t_1 = 0.02$, $t_2 = 0.06$, $t_3 = 0.03$ and $t_4 = 0.045$. The Hermitian setting corresponds to the case $h_1 = h_2 = 0$, whereas the non-Hermitian setting is for $h_1 = h_0$, $h_2 = h_0'$.

tice, we have $H_I = H_{\mathrm{SSH}}$, $H_J = \mathrm{diag}(E_B, \ldots, E_B)$. The Hermitian coupling matrices are given by:

$$\tilde{H}^{\dagger}_{I\leftarrow J} = H^{\dagger}_{I\leftarrow J} = \begin{pmatrix} t_3 & 0 & \ldots & \ldots & \ldots & \ldots \\ \ldots & 0 & t_3 & 0 & \ldots & \ldots \\ \ldots & \ldots & \ldots & \ldots & \ldots & \ldots \\ \ldots & \ldots & \ldots & \ldots & 0 & t_3 \end{pmatrix} \tag{4.42}$$

and

$$\tilde{H}^{\dagger}_{J\to I} = H^{\dagger}_{J\to I} = \begin{pmatrix} t_4 & 0 & \ldots & \ldots & \ldots & \ldots \\ \ldots & 0 & t_4 & 0 & \ldots & \ldots \\ \ldots & \ldots & \ldots & \ldots & \ldots & \ldots \\ \ldots & \ldots & \ldots & \ldots & 0 & t_4 \end{pmatrix}. \tag{4.43}$$

The zero-energy corner mode is analytically written as:

$$\psi^{(0)}_{I,m} = r^m_{0,2}\psi^{(0)}_{I,0} \tag{4.44}$$

with

$$\left[\psi^{(0)}_{I,0}\right]_n = r^n_{0,1}a_{0,0} \tag{4.45}$$

being the n-th component of the zero-energy mode $\psi^{(0)}_{I,0}$ of the SSH lattice, and $a_{n,m}$ is the modal amplitude on the A site at the n-th unit cell in the m-th lattice I. The interference conditions [Eq. 4.24] give:

$$r_{0,1} = -\frac{t_1}{t_2} \tag{4.46}$$

and

$$r_{0,2} = -\frac{t_3}{t_4}. \tag{4.47}$$

We use an imaginary gauge field in order to delocalise the corner mode. Figure 4.10(a) sketches the gauge potential considered where e^{h_1} and e^{h_2} represent the phase factor in the couplings between the sites A and C, A and B, respectively. The coupling matrices are then modified, and we have:

$$\tilde{H}^\dagger_{I\leftarrow J} = \begin{pmatrix} t_3e^{h_2} & 0 & \dots & \dots & \dots & \dots \\ \dots & 0 & t_3e^{h_2} & 0 & \dots & \dots \\ \dots & \dots & \dots & \dots & \dots & \dots \\ \dots & \dots & \dots & \dots & 0 & t_3e^{h_2} \end{pmatrix} \tag{4.48}$$

and

$$\tilde{H}^\dagger_{J\to I} = \begin{pmatrix} t_4e^{-h_2} & 0 & \dots & \dots & \dots & \dots \\ \dots & 0 & t_4e^{-h_2} & 0 & \dots & \dots \\ \dots & \dots & \dots & \dots & \dots & \dots \\ \dots & \dots & \dots & \dots & 0 & t_4e^{-h_2} \end{pmatrix}. \tag{4.49}$$

The interference conditions now yield:

$$r_{0,1} = -\frac{t_1}{t_2}e^{2h_1} \tag{4.50}$$

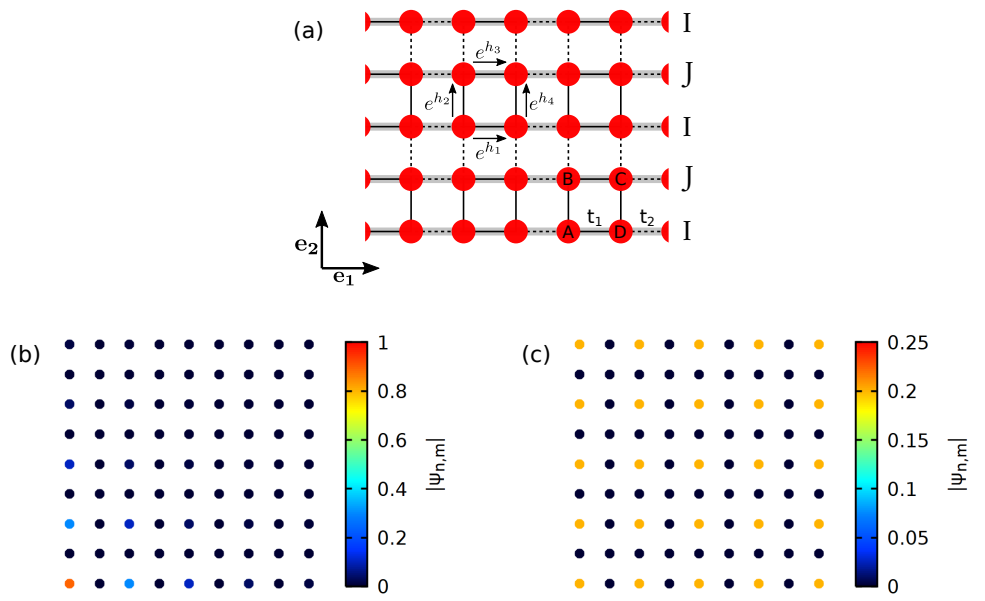

Figure 4.11: (a) Schematic of a non-Hermitian 2D SSH lattice drawn in the quasi-1D lattice formalism. The solid and dashed lines denote the intra-cell (t_1) and inter-cell couplings (t_2), respectively. e^{h_1}, e^{h_2}, e^{h_3} and e^{h_4} correspond to the imaginary gauge field. The normalised field profile $|\psi_{n,m}|$ of the zero-energy mode of the truncated 2D SSH lattice is plotted in (b) for the Hermitian case, and in (c) for the non-Hermitian case. Here, there are $N_s = 9$ sites both in the I lattice and the quasi-1D lattice. $t_1 = 0.02$, $t_2 = 0.06$. The Hermitian setting corresponds to the case $h_1 = h_2 = h_3 = h_4 = 0$, whereas the non-Hermitian setting is for $h_1 = h_2 = h_3 = h_4 = h_0$.

and

$$r_{0,2} = -\frac{t_3}{t_4} e^{2h_2}. \tag{4.51}$$

Delocalisation over the $\boldsymbol{e_i}$-direction is achieved by requiring $|r_{0,i}| = 1$, namely choosing:

$$h_1 = h_0 := -\frac{1}{2} \ln\left(\frac{t_1}{t_2}\right) \tag{4.52}$$

and

$$h_2 = h_0' := -\frac{1}{2} \ln\left(\frac{t_3}{t_4}\right). \tag{4.53}$$

Figure 4.10(c) shows that the zero-energy mode is indeed extended over the whole bulk of the Lieb lattice.

4.5.2 2D SSH lattice

Here, we study the 2D SSH lattice [121] which is characterised by four sites by unit cell, and intra-cell (t_1) and inter-cell (t_2) couplings, as shown in

Fig. 4.11(a). The method follows similarly to the two examples already provided previously.

We will delocalise the zero-energy mode present in the 2D SSH lattice [see Fig. 4.11(b) for the shape of the lattice]. Figure 4.11(b) plots the normalised field distribution $|\psi_{n,m}|$ of the zero-energy corner mode which is exponentially localised on the bottom-left corner for $t_1 < t_2$.

For the (Hermitian) truncated 2D SSH lattice, we have $H_I = H_{\mathrm{SSH}}$, $H_J = H_{\mathrm{SSH}}$. The intra- and inter-stacked lattice couplings $H_{I\leftarrow J}$ and $H_{J\rightarrow I}$, respectively, are given via:

$$\tilde{H}^{\dagger}_{I\leftarrow J} = H^{\dagger}_{I\leftarrow J} = \mathrm{diag}(t_1, t_1, \ldots, t_1, t_1) \tag{4.54}$$

and

$$\tilde{H}^{\dagger}_{J\rightarrow I} = H^{\dagger}_{J\rightarrow I} = \mathrm{diag}(t_2, t_2, \ldots, t_2, t_2). \tag{4.55}$$

The zero-energy corner can be written as:

$$\psi^{(0)}_{I,m} = r^{m}_{0,2}\psi^{(0)}_{I,0} \tag{4.56}$$

with

$$\left[\psi^{(0)}_{I,0}\right]_n = r^{n}_{0,1}a_{0,0} \tag{4.57}$$

being the n-th component of the zero-energy mode $\psi^{(0)}_{I,0}$ of the SSH lattice, and $a_{n,m}$ is the modal amplitude on the A site at the n-th unit cell in the m-th lattice I. The interference conditions [Eq. 4.24] give:

$$r_{0,1} = -\frac{t_1}{t_2} \tag{4.58}$$

and

$$r_{0,2} = -\frac{t_1}{t_2}. \tag{4.59}$$

An imaginary gauge field is used to change the localisation property of the corner mode. Figure 4.11(a) sketches the gauge potential considered where e^{h_1}, e^{h_2}, e^{h_3} and e^{h_4} represent the phase factor in the couplings between the sites A and D, A and B, B and C, and D and C, respectively. The values for e^{h_1}, e^{h_2}, e^{h_3} and e^{h_4} are not independent of each other. For the spectrum to

remain unchanged, one needs to satisfy:

$$h_3 = h_1 \tag{4.60}$$

and

$$h_4 = h_2. \tag{4.61}$$

With the imaginary gauge field, the coupling matrices are then modified. Particularly, we have:

$$\tilde{H}^{\dagger}_{I\leftarrow J} = \mathrm{diag}(t_1 e^{h_2}, t_1 e^{h_4}, \ldots, t_1 e^{h_2}, t_1 e^{h_4}) \tag{4.62}$$

and

$$\tilde{H}^{\dagger}_{J\rightarrow I} = \mathrm{diag}(t_2 e^{-h_2}, t_2 e^{-h_4}, \ldots, t_2 e^{-h_2}, t_2 e^{-h_4}). \tag{4.63}$$

The interference conditions read:

$$r_{0,1} = -\frac{t_1}{t_2} e^{2h_1} \tag{4.64}$$

and

$$r_{0,2} = -\frac{t_1}{t_2} e^{2h_2}. \tag{4.65}$$

Delocalisation over the $\boldsymbol{e_i}$-direction is achieved by requiring $|r_{0,i}| = 1$, namely choosing:

$$h_1 = h_2 = h_0 := -\frac{1}{2} \ln\left(\frac{t_1}{t_2}\right). \tag{4.66}$$

Figure 4.11(c) shows that the zero-energy mode is indeed extended over the whole bulk of the 2D SSH lattice.

4.6 Physical realisation of extended modes in a ring resonator array

A physical realisation of such a non-Hermitian system for the extended modes is possible by considering an array of coupled active ring resonators [39, 122]. Then, the non-Hermitian term can be modelled by an auxiliary ring, connecting the ring resonators, and with different loss constants on the upper

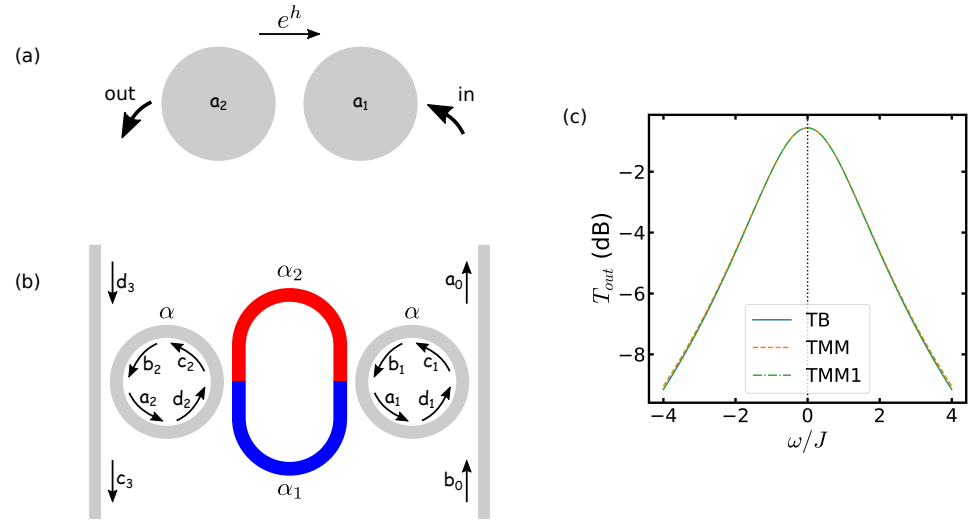

Figure 4.12: (a) Schematic of the tight-binding model (TB) with non-reciprocal couplings. a_i, $i = 1, 2$, are the amplitudes on the corresponding site, and h is the non-Hermitian strength. The "in" and "out" arrays represent the input and output coupling of the system, respectively. (b) Schematic of the transfer matrix method (TMM) with main rings coupled via an intermediate ring. The main rings have absorption constant α and the intermediate ring has different absorption constants on the upper (α_2) and lower (α_1) half of its perimeter. a_i, b_i, c_i and d_i are the modal amplitudes in their corresponding section of the waveguides. (c) Absolute value of transmission (in dB) $10\ln(|T_{\text{out}}|^2)/\ln(10)$. TB stand for the transmission calculated from the TB model (Eq. 4.70), TMM and TMM1 for the exact (Eq. 4.72) and approximated (Eq. 4.94) expression in the TMM method, respectively. The parameters used are similar to Ref. [8]. The tight-binding parameters are $\kappa_{\text{ex}} = 3\,\text{GHz}$, $\kappa_{\text{in}} = 0.2\,\text{GHz}$, $J = 2\,\text{GHz}$. We have consider silicon-on-insulator (SOI) ring resonators with effective (group) refractive index $n_{\text{eff}} = 2.47$ ($n_g = 4.7$). The ring resonator length is $L = 80.3\,\mu\text{m}$ so that the resonant wavelength is at $\lambda_0 = 1550\,\text{nm}$. In the auxiliary ring, the additional leg length is $\eta = 4\lambda_0/n_{\text{eff}}$, the absorption constant is given by $\alpha_0 = \alpha/2$.

and lower half of its perimeter as illustrated in Fig. 4.12(b). In this section, we explore the equivalence between the tight-binding (TB) formalism used to derive the results so far, and the transfer matrix method (TMM) commonly used to describe the ring resonator arrays [50, 51]. This extends the work realised in Ref. [8] which was used for introducing phase shifts in the couplings. Moreover, the TMM analysis provides additional insight into the geometrical parameters for an experimental realisation.

To study the equivalence between the two formalisms, we will focus on the transmission spectra after injection of a source term. Besides, instead of looking at the whole lattice, we will consider the building block of the system:

it is made of only two sites that are coupled each other via an asymmetric coupling, as illustrated in Fig. 4.12(a) for the TB model. The equivalent building block for the ring resonator system is made of two main rings and an additional auxiliary ring resonator [Fig. 4.12(b)].

The tight-binding formalism [Fig. 4.12(a)] is given by:

$$i\frac{da_1}{dt} = i(-\kappa_{\text{in}} - \kappa_{\text{ex}})a_1 + Je^{h}a_2 - \sqrt{2\kappa_{\text{ex}}}E_{\text{in}}, \tag{4.67}$$

$$i\frac{da_2}{dt} = i(-\kappa_{\text{in}} - \kappa_{\text{ex}})a_2 + Je^{-h}a_1 \tag{4.68}$$

where κ_{in} is the internal loss, J the coupling strength, h the gauge field. E_{in} is the source term that is coupled with the system at the a_1 site with an external coupling strength κ_{ex}. The transmission at the a_2 site is defined as:

$$T_{\text{out,TB}} := \frac{\sqrt{2\kappa_{\text{ex}}}a_2}{E_{\text{in}}}. \tag{4.69}$$

This yield:

$$T_{\text{out,TB}} = \frac{2i\kappa_{\text{ex}}Je^{-h}}{J^2 + (i\omega - \kappa_{\text{in}} - \kappa_{\text{ex}})^2}. \tag{4.70}$$

On the other hand, the ring resonator system is composed of two main rings of perimeter L and an auxiliary ring of perimeter $L + 2\eta$, where 2η is the total length of the additional legs compared to the main circular rings. The absorption constant of the main rings is α, and the auxiliary is considered to have different internal losses on the upper (α_2) and lower (α_1) half of its perimeter. The relation between the input b_0 and the output c_3 is given, in the transfer matrix formalism, by:

$$\begin{pmatrix} c_3 \\ d_3 \end{pmatrix} = M \begin{pmatrix} b_0 \\ a_0 \end{pmatrix} \tag{4.71}$$

from which we set $a_0 = 0$ and $d_3 = 0$, and the transmission is defined as:

$$T_{\text{out,TMM}} := \frac{c_3}{b_0}. \tag{4.72}$$

The transfer matrix M reads:

$$M = M_1 Q_1 (M_2 Q_2 M_2) Q_1 M_1. \tag{4.73}$$

The matrices M_i, $i = 1, 2$, are the transfer matrices of the waveguided modes between the external waveguide to the main rings, or between the main rings and the auxiliary ring, respectively. For example, we have for M_1:

$$\begin{pmatrix} c_1 \\ d_1 \end{pmatrix} = M_1 \begin{pmatrix} b_0 \\ a_0 \end{pmatrix} \quad , \quad \begin{pmatrix} c_3 \\ d_3 \end{pmatrix} = M_1 \begin{pmatrix} b_2 \\ a_2 \end{pmatrix} \tag{4.74}$$

The matrices Q_i, $i = 1, 2$, are the transfer matrices of the waveguided modes inside the main rings or the auxiliary, respectively. For example, we have for Q_1:

$$\begin{pmatrix} b_1 \\ a_1 \end{pmatrix} = Q_1 \begin{pmatrix} c_1 \\ d_1 \end{pmatrix} \quad , \quad \begin{pmatrix} b_2 \\ a_2 \end{pmatrix} = Q_1 \begin{pmatrix} c_2 \\ d_2 \end{pmatrix} \tag{4.75}$$

The transfer matrices are then written as:

$$M_i = \frac{1}{t_i} \begin{pmatrix} -r_i^2 + t_i^2 & r_i \\ -r_i & 1 \end{pmatrix} \tag{4.76}$$

with t_i an r_i being the transmission and reflection coefficient between the waveguides, and

$$Q_i = \begin{pmatrix} q_{i,l} & 0 \\ 0 & q_{i,r} \end{pmatrix} \tag{4.77}$$

where

$$q_{1,l} = e^{i(\beta + i\alpha)\frac{L}{2}}, \tag{4.78}$$

$$q_{1,r} = e^{-i(\beta + i\alpha)\frac{L}{2}}, \tag{4.79}$$

$$q_{2,l} = e^{i(\beta + i\alpha_1)\left(\frac{L}{2} + \eta\right)}, \tag{4.80}$$

$$q_{2,r} = e^{-i(\beta + i\alpha_2)\left(\frac{L}{2} + \eta\right)}. \tag{4.81}$$

$\beta = 2\pi n/\lambda$ is the propagation constant, where n is the refractive index of the ring resonators and λ is the considered wavelength.

Assuming the coupling loss is negligible and that the junctions are highly reflective, we set:

$$t_i = i\epsilon_i, \tag{4.82}$$

$$r_i = \sqrt{1-\epsilon_i^2} \tag{4.83}$$

where $\epsilon_i \ll 1$, $i = 1, 2$. Besides, we assume :

$$\beta L \ll 1 \tag{4.84}$$

since we are interested in the regime close to the resonant frequency of the main rings, *i.e.* $\omega \ll \mathrm{FSR}$ with ω the detuning frequency away from the resonant frequency ω_0 and $\mathrm{FSR} = 2\pi c/(n_g L)$ the free spectral range of the cavity mode and n_g the group refractive index. Because of the low propagation loss over the scale of the system, we take, for $i = 1, 2$:

$$\alpha L \ll 1, \tag{4.85}$$

$$\alpha_i L \ll 1. \tag{4.86}$$

By keeping only the terms up to the second order in ϵ_i^2, βL, αL, $\alpha_i L$, $i = 1, 2$, we have for

$$\alpha_{1,2} = \alpha \pm \alpha_0, \tag{4.87}$$

the transmission in the TMM formalism that reads:

$$T_{\mathrm{out,TMM}} \simeq -\frac{2\kappa_{\mathrm{ex}} J e^{-h}}{2(i\omega - \kappa_{\mathrm{in}} - \kappa_{\mathrm{ex}})J\cos(\beta\eta) + i[((i\omega - \kappa_{\mathrm{in}} - \kappa_{\mathrm{ex}})^2 + J^2)\sin(\beta\eta)]} \tag{4.88}$$

where the normalised quantity are:

$$\epsilon_1^2 = 4\pi\frac{\kappa_{\mathrm{ex}}}{\mathrm{FSR}}, \tag{4.89}$$

$$\epsilon_2^2 = 4\pi\frac{J}{\mathrm{FSR}}, \tag{4.90}$$

$$\alpha L = 2\pi\frac{\kappa_{\mathrm{in}}}{\mathrm{FSR}}, \tag{4.91}$$

$$\beta L = 2\pi\frac{\omega}{\mathrm{FSR}}, \tag{4.92}$$

and where the imaginary gauge field h is given by:

$$h = -\alpha_0 \eta = \frac{\alpha_2 - \alpha_1}{2}\eta. \tag{4.93}$$

For general $\beta\eta$, *i.e.* for an arbitrary leg length in the auxiliary ring, and as long as $\sin(\beta\eta) \neq 0$, the transmission is re-written as:

$$T_{\text{out,TMM}} \simeq -\frac{2i\kappa_{\text{ex}} J_{\text{eff}} e^{-h}}{J_{\text{eff}}^2 + (i\omega_{\text{eff}} - \kappa_{\text{in}} - \kappa_{\text{ex}})^2} \tag{4.94}$$

with

$$J_{\text{eff}} := -\frac{J}{\sin(\beta\eta)}, \tag{4.95}$$

$$\omega_{\text{eff}} := \omega - \frac{J}{\tan(\beta\eta)}. \tag{4.96}$$

Therefore, for TB to be equivalent to TMM, one needs to make the following modification:

$$J \to -J_{\text{eff}}, \tag{4.97}$$

$$\omega \to \omega_{\text{eff}}. \tag{4.98}$$

We can see in Fig. 4.12(c) that the transmission spectrum for the TB and TMM formalism are indeed identical for the parameter given in the caption.

Moreover, it should be noted that the ring-resonators feature degenerates clockwise and counter-clockwise modes. Here, we have used the counter-clockwise mode in the main rings for the purpose of the demonstration. Yet, we can see that using the clockwise mode in the main rings, instead of the counter-clockwise mode, leads to a different situation where the modes propagating from left to right go through the α_1-leg, instead of the α_2-leg. Similarly for the modes propagating from right to left that go through the α_2-leg, instead of the α_1-leg. The main consequence is the modification of Eq. 4.93 which takes a minus sign. Therefore, the defining relation for the strength of the imaginary gauge field can be reduced to:

$$h = |\alpha_0 \eta| = \left| \frac{\alpha_2 - \alpha_1}{2}\eta \right|, \tag{4.99}$$

while the sign is determined based on which situation we would like to realise.

4.7 Summary

To summarise, we have shown a procedure to obtain topological modes extended over a d-dimensional bulk using an imaginary gauge field. In particular, we have demonstrated the existence of a topological extended mode in the kagome lattice in the rhombus geometry. The topological extended mode in the kagome lattice has been studied in the context of a lasing system where the laser rate equation is included to take into account non-linear effects. By investigating its temporal stability, we proved that stable topological broad-area phase-locked laser operation is possible in a large region in the parameter space. Furthermore, it has been shown that the topological extended mode presents clear advantages over the topological localised mode. The extended nature of the former topological mode over the bulk enhances its temporal stability, and yields higher slope efficiency that scales with the size of the system. In terms of footprint, a higher-dimensional extended mode is also more advantageous compared to their lower-dimensional one since, at equivalent slope efficiency, for example, the system occupies a smaller region in real space when increasing the dimensionality of the system. This can lead to applications where transport of high energy density is possible. A physical system made of ring resonators has been studied for the purpose of a possible realisation of the topological bulk lasing modes.

Chapter 5

Data-driven classification of topological lasing modes

5.1 Introduction

In the past years, significant research has been made on PTI lasers. Yet, the efforts have been mainly focused on the spatial stability of the topologically protected edge mode, namely on the existence of such topological edge mode from non-Hermitian PTIs [28–30], whereas the temporal stability has not been the focus of interest so far [42]. Because of the non-linear nature of PTI lasers, the temporal stability is an important characteristic to take into account. Indeed spatial stability may be guaranteed in active non-Hermitian PTIs, *i.e.* no back-scattering at corners, sharp edges, etc., but unstable behaviour may be present in its time series. In this regard, the temporal dynamics of the topologically protected modes have been studied [39–41], mainly using linear stability analysis. It is, however, a challenging task to apply the same approach to more complex structures because of the high-dimensional phase and parameter space as well as the lack of analytical solutions [42].

ML can be advantageous for the theoretical study of PTIs which requires the simulations and study of several varying parameters. ML is a data-based method and the most appropriate ML strategy depends on the dataset we are working with. A supervised learning strategy relies on labelled datasets, namely on input-output pairs datasets. This has been utilised, for example, to draw topological phase diagrams [43], calculate topological invariants [44], or

explore topological band structures [45]. On the other hand, an unsupervised learning strategy consists of extracting information from the dataset from which we do not have the labels. This is used for dimensional reductions by keeping only the main features of the high dimensional structure of the dataset or for clustering problems from which the data is divided into different types. For instance, this has been successful in obtaining the phase transition in the Ising model [123], or clustering Hamiltonians belonging to the same symmetry classes [124].

In the unsupervised learning strategy, modal decompositions are common and successful methods which reduce the analysis of a very high-dimensional data to a set of relatively few modes. Principal component analysis (PCA) is one of these modal decomposition methods from which it derives the eigenmodes or the main features based on their variance in the data [125]. These eigenmodes can then be utilised as a basis to represent the dataset [126]. This reduced-order model method has been extended to identify distinct non-linear regimes [127–133] by constructing a library composed of representatives of these regimes: this is known as representation classification. Nevertheless, the construction of the library is a manual process and requires an expert knowledge of the complex system.

In this chapter, we propose to use representation classification in order to study the spatio-temporal dynamics of non-linear topological systems. To remove the required expertise on the complex system, we present an algorithm in order to construct an appropriate library of the different phases in an automatic way. The results will be based on the phase diagram of the SSH lattice with a domain wall and with saturable gain [40, 41]. To this end, we will start by presenting the results on the SSH lattice known from Ref. [40]. This will be used as a reference for comparing the results using the proposed method. Moreover, we will review the representation classification method based on the construction of a library of bases. We will also see how to obtain such bases from the dataset. Finally, we present our adaptive method to classify the topological phase in the SSH system. Here, two approaches are suggested to achieve this goal: a top-down approach for which the library has too many phases and then merge the equivalent phases, and a bottom-up approach for

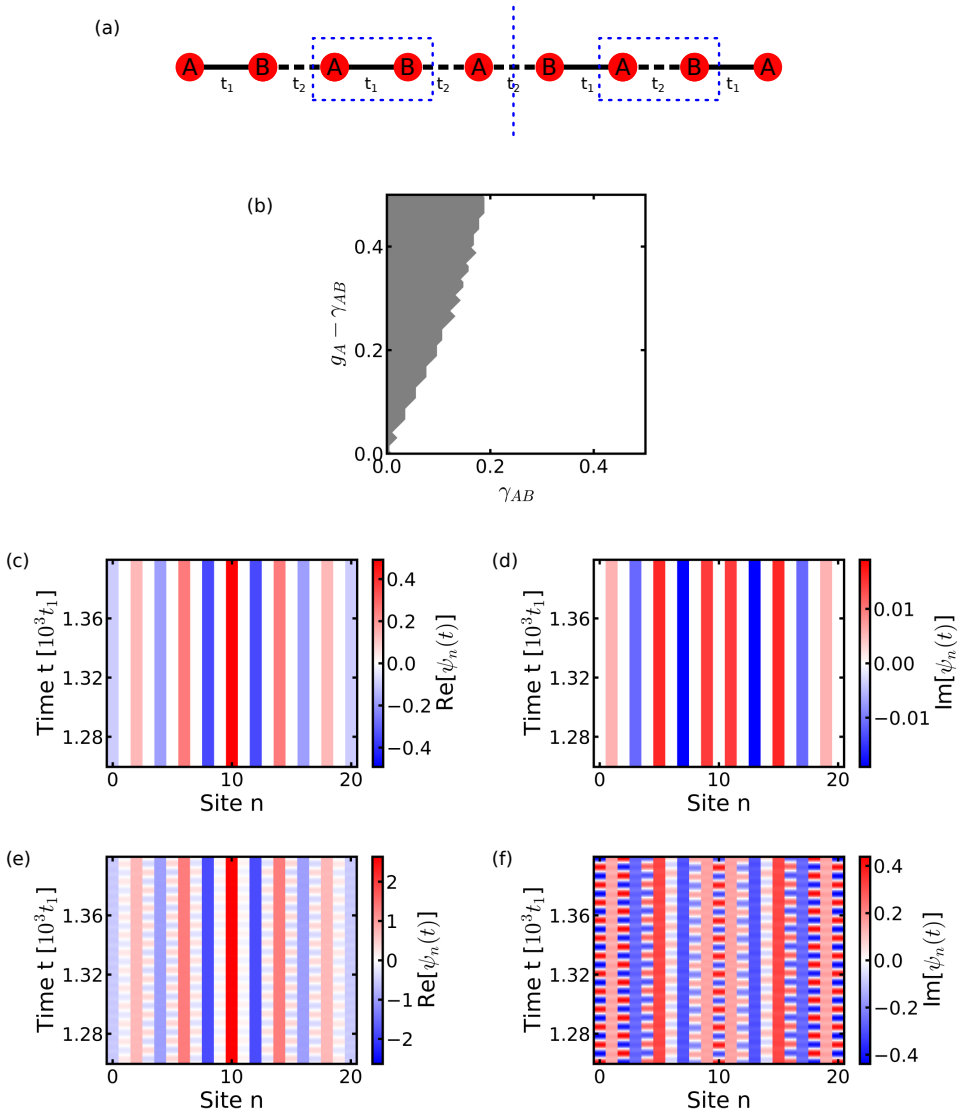

Figure 5.1: (a) Schematic of the domain-wall-type SSH lattice considered. (b) Phase diagram of the SSH lattice presented in (a) with saturable gain and linear loss on the A and B sublattices. The spatio-temporal dynamics of the non-oscillating and oscillating topological lasing modes are plotted in (c),(d) and (e),(f), respectively. The coupling and gain parameters chosen are $t_1 = 1$, $t_2 = 0.7t_1$ and $g_B = 0$.

which we complete the library on the fly in order to get the most accurate classification.

5.2 Toy model: the SSH lattice with saturable gain

The system, that we will be looking at, is the domain-wall-type SSH lattice with saturable gain [Fig. 5.1(a)]. The SSH lattice is composed of two sites per

unit cell, A and B, and is characterised by intra- and inter-unit cell coupling t_1 and t_2, respectively. The domain-wall divides the SSH lattice where the intra-unit cell coupling is greater than the inter-unit cell coupling on one side, and the reverse on the other side [see Chap. 1], as schematically shown with the vertical dotted line in Fig. 5.1(a).

The dynamics $\psi(t) = (\ldots, a_n(t), b_n(t), \ldots) \equiv x(t)$ of the system is governed by the coupled-mode equations:

$$i\frac{da_n}{dt} = i\left(\frac{g_A}{1+|a_n|^2} - \gamma_A\right)a_n + t_1 b_n + t_2 b_{n-1}, \tag{5.1}$$

$$i\frac{db_n}{dt} = i\left(\frac{g_B}{1+|b_n|^2} - \gamma_B\right)b_n + t_1 a_n + t_2 a_{n+1}, \tag{5.2}$$

where a_n and b_n are, respectively, the amplitudes of the A and B sites on the n-th unit cell. g_σ and γ_σ are the linear gain and linear loss at the site $\sigma = A, B$.

Depending on the gain and coupling parameters, it has been shown in Ref. [40,41] that the system belongs to different topological phases. In particular, we show in Fig. 5.1(b) the phase diagram that will serve as a reference for our proposed method. This phase diagram has been obtained by fast Fourier transform (FFT) by setting $t_1 = 1$, $t_2 = 0.7t_1$, $g_B = 0$, and by varying g_A, and $\gamma_A = \gamma_B \equiv \gamma_{AB}$ in the parameter space. The system has two topological phases in this configuration: it can be either in a non-oscillating phase or in an oscillating phase. This can be seen by looking at the real and imaginary parts of the space-time evolution of the topological modes in Figs. 5.1(c)-5.1(f). The even (odd) site indices correspond to the A (B) sites, and the domain wall happens at the site index 10 (an A site). The non-oscillating phase is similar to the zero-energy mode in the passive SSH lattice. We can see in Figs. 5.1(c) and 5.1(d) that the mode is exponentially localised at the interface and has the majority of its amplitudes on the A sublattice. On the other hand, the system with saturable gain exhibits a new topological phase with no counterpart in the Hermitian setting. The new topological mode is characterised by an edge mode at the domain wall with an oscillating behaviour of the amplitudes on the A and B sites, as shown in Figs. 5.1(e) and 5.1(f).

The dataset that we will utilise throughout this chapter is composed of

about 1000 samples which are randomly generated from the same coupling and gain parameters' range as in Fig. 5.1(b). The coupled-mode equations [Eqs. 5.1 and 5.2] are integrated using a fourth-order Runge-Kutta method and with $a_n(t = 0) = b_n(t = 0) = 0.01$, $\forall n$ as initial condition. Although the integration has been performed using a fixed time step $dt/t_1 = 0.01$ until a final time at $t/t_1 = 1400$, only 2000 time snapshots are retrieved in order to keep the time series at a reasonable size. The phase diagram is then intended to be obtained solely from the time series of the states within the given parameter space.

The method proposed in the next sections might seem unnecessary since the phase diagram in Fig. 5.1(b) has been obtained solely by a FFT of the times series in the parameter space. Nevertheless, this classification has been possible thanks to the known results derived in Ref. [40], and thus from an expert knowledge of this non-linear system. The aim is to have a tool to explore the topological phases of topological insulator lasers in a more complicated setting from which we have little knowledge.

5.3 Representation classification

In this section, we will briefly review the representation classification method to identify distinct non-linear regimes [127, 131, 132]. The general idea of representation classification relies on the assumption, and common situations, that the dynamics of a high-dimensional system evolve on a low-dimensional attractor [134]. The low-dimensional structure of the attractors allows for a reduced-order model that accurately approximates the underlying behaviour of the system: the dynamics of the complex system can thus be written using a basis that spans the low-dimensional space. Representation classification consists of constructing a library of appropriate basis, representative of the dynamical regimes of interest, and only then employ a filtering strategy to identify the regime corresponding to a given unknown time series. Here we use the term "regime" to denote the different dynamical behaviours or the different topological phases in the non-linear system.

5.3.1 Library construction

As is common in complex dynamical systems, the dynamics of a system close to an attractor lie in a low-dimensional space. This means that a given spatio-temporal dynamics, denoted by the vector $x(t)$, can be approximately written in terms of a basis $\Phi = \{\phi_i\}_{i=1,\dots,D}$ spanning the low D-dimensional space, namely:

$$x(t) = \sum_{i=1}^{D} \phi_i \beta_i(t) = \Phi\beta(t) \tag{5.3}$$

where β_i are the weighted coefficients in the above linear combination of basis states ϕ_i. $x(t)$, at a given time t, is a vector column of size N_s with N_s the size of the spatial grid, *i.e.* the number of sites in our SSH lattice for instance.

However, one of the main characteristics of non-linear systems is the drastically different dynamical behaviours with respect to the system's parameters. Therefore the reduced-order modelling strategy using a single representative basis, *i.e.* corresponding to a single regime, is bound to fail. Instead of finding a global basis, we here construct a set of local bases, *i.e.* construct a library composed of the bases of each non-linear regime of interest:

$$\mathcal{L} = \{\Phi_1, \cdots, \Phi_J\} = \{\phi_{j,i}\}_{j=1,\dots,J\,,\,i=1,\dots,D}, \tag{5.4}$$

where J is the number of regimes, Φ_j are the bases of each of the dynamical regime j, and $\phi_{j,i}$ are the corresponding basis states. This is the supervised learning part of the method, from which the data-driven method attempts to capture the dynamics of the system in the reduced-order model. Therefore, the library $\mathcal{L}$ contains the representative basis of each regime of interest, and corresponds to an overcomplete basis that approximates the dynamics of the system across the given parameter space:

$$x(t) = \sum_{j=1}^{J} \sum_{i=1}^{D} \phi_{j,i} \beta_{j,i}(t) = \sum_{j=1}^{J} \Phi_j \beta_j(t) \tag{5.5}$$

where $\beta_{j,i}$ are the weighted coefficients in the above linear combination in the overcomplete basis library. It is worth noting that the library modes $\phi_{j,i}$ are not orthogonal to each other, but rather orthogonal in groups of modes for

each different regimes j.

5.3.2 Basis generation

There are many ways to generate the low-order model of a given dynamical behaviour. An important quantity is the so-called data matrix X built from the data at hand. The data matrix is a $(N_s \times N_t)$-matrix that collects the N_t data snapshots $x(t_i)$ into columns:

$$X = [x(t_0), x(t_1), \ldots, x(t_{N_t})]\,. \tag{5.6}$$

Here, the vector $x(t_i)$ is chosen to be the complex-valued amplitudes of the modes at the A and B sites. Other "observables", such as the absolute values or the total intensity per sublattices, can be used. This may give different (better or worse) results and is left for a future study. The bases can then be constructed using dimensional reduction techniques on the data matrix. Here we will cover different methods in order to highlight their importance and limitations for the classification scheme used.

Proper orthogonal decomposition (POD) [128] is a commonly used tool for dimensionality reduction of physical systems. This decomposition relies on the singular value decomposition (SVD) of the data matrix, given by:

$$X = U\Sigma V^\dagger \tag{5.7}$$

where U and $V^\dagger$ are $(N_s \times N_s)$ and $(N_s \times N_t)$ unitary matrices, respectively. Σ is a diagonal $(N \times N)$-matrix diag $= (\sigma_1, \ldots, \sigma_N)$, with $N = \min(N_s, N_t)$. The diagonal entries of Σ are the so-called singular values and are ordered in ascendant order $\sigma_1 > \sigma_2 > \ldots > \sigma_N \geq 0$. The SVD gives us two orthonormal bases U and $V^\dagger$ since the matrices U and $V^\dagger$ are unitary matrices. The columns of U are ordered according to the variance σ_i they capture in the data matrix and are called the singular vectors: these are the POD modes that are used in the basis Φ. Moreover, the POD modes are complex because of the complex data X.

For a low-dimensional attractor, the POD basis can be safely truncated

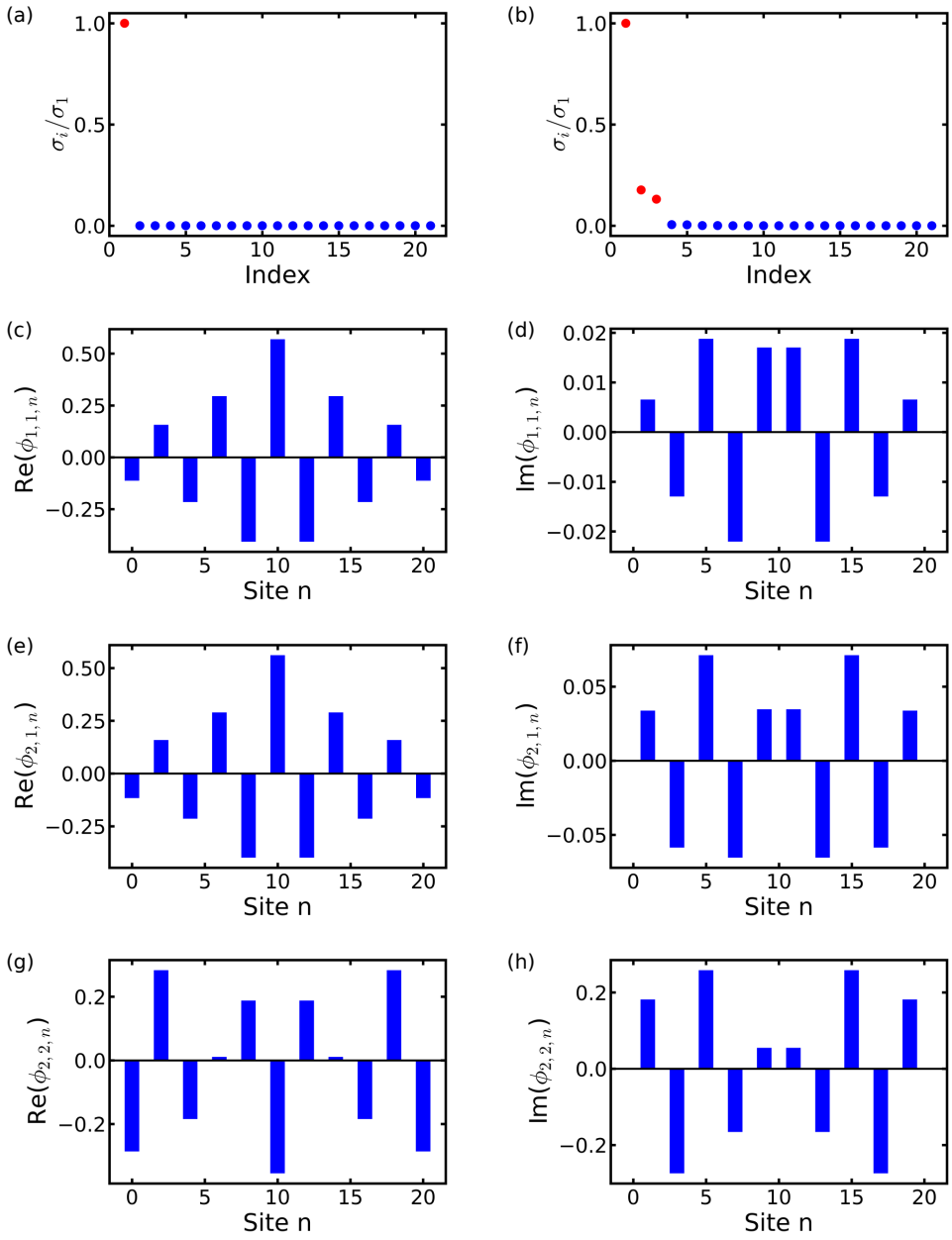

Figure 5.2: Singular values of the (a) non-oscillating and (b) oscillating regimes. The red dots correspond to the singular values cumulating 99% of the total variance of the data. Real and imaginary parts of the field profile of: (c),(d) the first POD mode for the non-oscillating regime ($j = 1$), and of (e),(f) the first and (g),(h) the second POD modes for the oscillating regime ($j = 2$). The POD bases have been generated from the time series starting at the 1800-th time step.

at a cut-off value r while retaining the main information of the data matrix.

Explicitly, the SVD reads:

$$X_{im} = \sum_{n=0}^{N} U_{in}\sigma_n V^{\dagger}_{nm}, \tag{5.8}$$

and keeping only the r highest terms in the decomposition [Eq. 5.8], we have the approximation:

$$X_{im} \simeq \sum_{n=0}^{r} U_{in}\sigma_n V^{\dagger}_{nm}. \tag{5.9}$$

This is re-written, in a matrix form, as:

$$X \simeq U_r \Sigma_r V_r^{\dagger} \tag{5.10}$$

where U_r, Σ_r and $V_r^{\dagger}$ are the truncated matrix of U, Σ and $V^{\dagger}$, respectively. Although the cut-off value r can be chosen based on different criteria [135], r is typically chosen so that the POD modes retain a certain amount of the variance (or energy) σ_X in the data, namely:

$$\sum_{i=0}^{r} \sigma_i > \sigma_X. \tag{5.11}$$

Figure 5.2 displays the POD method of the non-oscillating and oscillating regimes in the domain-wall SSH lattice with saturable gain [Fig. 5.1]. The truncation has been chosen such that $\sigma_X = 99\%$ of the total variance is retained. We observe in Figs. 5.2(a) and 5.2(b) the normalised singular values, and that a single POD mode is retained for the zero-mode-like, whereas three POD modes are needed for the oscillating regime, as marked by the red dots. The real and imaginary parts of the field profile of the corresponding first few POD modes are plotted in Figs. 5.2(c) and 5.2(d) and Figs. 5.2(e)-5.2(h) for the zero-mode-like non-oscillating and oscillating regimes, respectively. One can see that the main spatial feature of the zero-mode is captured in the single POD mode obtained after truncation, where the majority of its amplitudes are on the A sublattice. On the other hand, the POD modes of the oscillating dynamical regime also capture part of the information with some finite amplitudes on the A and B sublattices.

Importantly, in this decomposition [Eq. 5.8], SVD is implicitly doing a

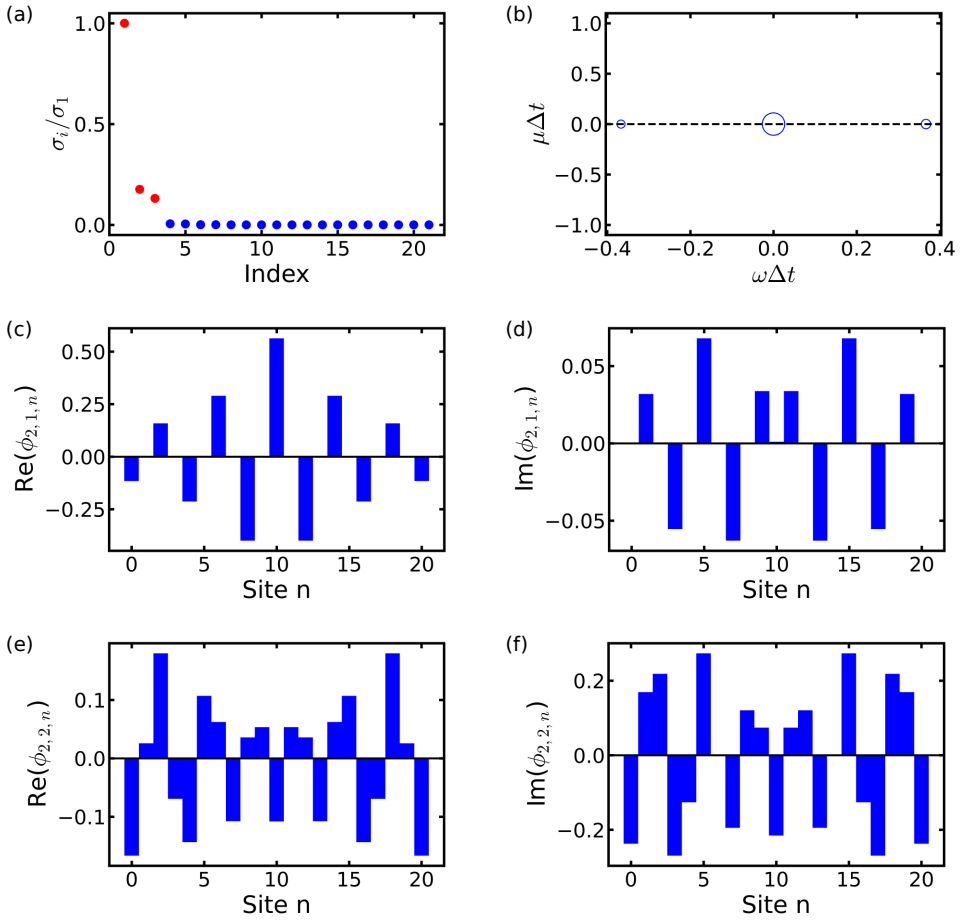

Figure 5.3: (a) Singular values of the oscillating regime in the DMD. The red dots correspond to the singular values cumulating 99% of the total variance of the data. (b) Plots of the logarithm of DMD values $\ln(\lambda)$ in the complex plane. The size of the open circle is proportional to their corresponding singular values. Real and imaginary parts of the field profile of: (e),(f) the first and (g),(h) the second DMD modes, respectively, for the oscillating regime ($j = 2$). The DMD basis has been generated from the time series starting at the 1800-th time step.

space-time separation of the data matrix, where the POD modes U contain the spatial information while V have the temporal information at each spatial grid point. Therefore, the POD modes give a static basis and do not explicitly model the temporal dynamics of the time series. This method will therefore most likely fail to identify the correct dynamical regime in the classification step.

Dynamical mode decomposition (DMD) [128, 136, 137] is an alternative to the POD method for learning the dynamics of non-linear systems. DMD is an

explicitly temporal decomposition that takes the sequences of snapshots into account, and is able to derive the spatio-temporal patterns of the data matrix X. The dynamics of the system are taken into account by considering a linear matrix A that maps a data matrix X_1, starting at some time steps (t_1), to the data matrix X_2, starting at the next time step (t_2). The matrix A is thus defined as:

$$X_2 = AX_1, \tag{5.12}$$

and the corresponding data matrices are given by:

$$X_1 = [x(t_1), x(t_2), \ldots, x(t_{N_t-1})] \tag{5.13}$$

and

$$X_2 = [x(t_2), x(t_3), \ldots, x(t_{N_t})]\,. \tag{5.14}$$

Interestingly, Equation 5.12 is similar to a linear stability analysis formulation for discrete maps if we think of the stability matrix as the linear matrix A. The DMD method thus consists of solving the following eigenvalues problem:

$$A\Phi = \Phi\Lambda \tag{5.15}$$

where the columns of Φ are the DMD modes ϕ_i and the corresponding DMD eigenvalues λ_i are the diagonal entry of Λ. The DMD modes ϕ_i give us the spatial eigenmodes while their corresponding eigenvalues λ_i have their temporal information. Using a change of units from data snapshots, observed at every Δt, to units in time, the eigenvalues are complex-valued scalars:

$$\frac{\ln(\lambda_i)}{\Delta t} = \mu_i + i\omega_i \tag{5.16}$$

where μ_i gives the growth (decay) rate if $\mu_i > 0$ ($\mu_i < 0$) and ω_i the oscillation frequency of the DMD modes ϕ_i.

However, the size of the data matrix usually makes the eigendecomposition not feasible. The goal, here, is therefore to approximate the eigenvalues and eigenvectors of A, using only the data matrices X_1 and X_2. The idea is to

start by the truncated SVD of $X_1 = U_r \Sigma_r V_r^\dagger$ in which Eq. 5.12 becomes:

$$X_2 = A U_r \Sigma_r V_r^\dagger. \tag{5.17}$$

Then the linear matrix A is reduced by considering its projection onto the truncated POD subspace:

$$A_r := U_r^\dagger A U_r = U_r^\dagger X_2 V_r \Sigma^{-1}. \tag{5.18}$$

The eigenvalue problem for A_r is solved with:

$$A_r W = W \Lambda, \tag{5.19}$$

from which we have the relation:

$$\Phi = X_2 V \Sigma^{-1} W. \tag{5.20}$$

The key feature of the DMD method is that it decomposes the data into a set of coupled spatio-temporal modes. The DMD resembles a mixture of the POD in the spatial domain and the discrete Fourier transform (DFT) in the time domain. Figure 5.3 shows the DMD results for the oscillating regime. We can, indeed, see in Fig. 5.3(a) that the singular values are similar to that of the POD. Besides, we observe in Figs. 5.3(c)-5.3(f) that the field profile of the DMD modes closely resembles the POD modes in Fig. 5.2. The largest DMD modes not only look similar to the POD modes, but they also contain the oscillation frequencies from ω_i, as in DFT. The DMD even goes beyond DFT by giving an estimate of the growth (decay) rate in time via $\mu_i > 0$ ($\mu_i < 0$). This can be seen by plotting the DMD modes, scaled by their contribution in the decomposition σ_i, in the frequency plane of λ_i. We can see in Fig. 5.3(b) that the dynamical regime has a single DMD mode with $\omega_i = 0$ akin to the offset of the oscillation amplitudes, and two DMD modes with opposite $\omega_i \neq 0$ corresponding to the oscillating behaviours. All the above three DMD modes have vanishing growth or decay rate $\mu_i = 0$.

Although the DMD gives the temporal behaviours of the non-linear system,

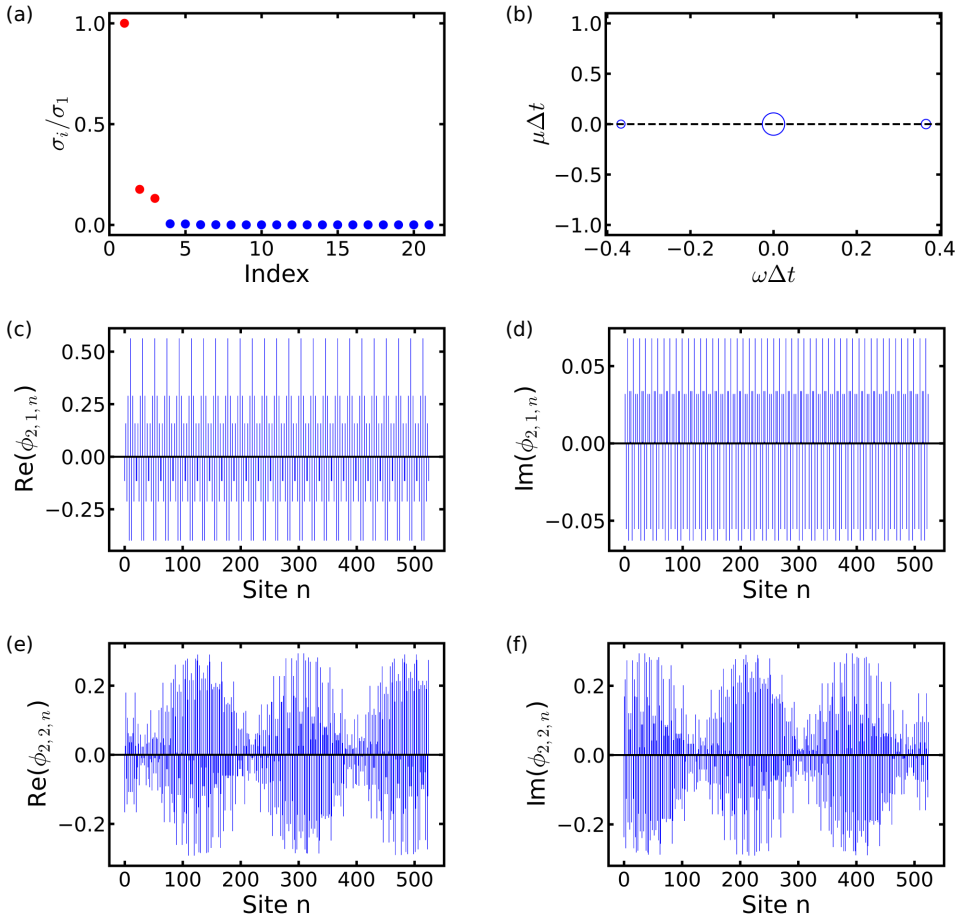

Figure 5.4: (a) Singular values of the oscillating regime in the aDMD. The red dots correspond to the singular values cumulating 99% of the total variance of the data. (b) Plots of the logarithm of aDMD values $\ln(\lambda)$ in the complex plane. The size of the open circle is proportional to their corresponding singular values. Real and imaginary parts of the "field profile" of the (e),(f) first and (g),(h) second aDMD modes, respectively, for the oscillating regime ($j = 2$). Here by "Site n", we mean the n-entry of the eigenvector. The aDMD basis has been generated with $N_w = 25$ from the time series starting at the 1800-th time step.

the temporal information is not fully incorporated into the DMD basis Φ since only the DMD modes are used. Exploiting the time evolution in the dynamical regime requires the use of DMD modes along with their eigenvalues. The idea is therefore to incorporate the dynamic information by augmenting the basis Φ [132]. This time-augmented DMD will be denoted by aDMD in the remaining of this chapter. Using the defining relation of the eigenvalues λ_i as similar to a time evolution operator, *i.e.* multiplying by λ is the same as shifting by one time step, we have for a given DMD mode ϕ_i, its evolution

given by $\lambda_i^{N_w}\phi_i$ at N_w time step ahead in time. Therefore, the time-augmented basis vector reads:

$$\begin{bmatrix} \phi_i \\ \lambda_i\phi_i \\ \vdots \\ \lambda_i^{N_w}\phi_i \end{bmatrix}. \tag{5.21}$$

The basis decomposition for a single regime [Eq. 5.3] is then re-written:

$$x(t_i : t_{i+N_w}) = \Phi\beta(t_i : t_{i+N_w}) \tag{5.22}$$

where the notation $(t_i : t_{i+N_w})$ means we consider a time window from time step t_i to t_{i+N_w}.

By considering a time window N_w, the time-augmentation of the DMD basis provides us with the dynamical information of the non-linear regime. Figure 5.4 shows the aDMD results for the same oscillating regime as in Fig. 5.3. We can see that the singular values and aDMD eigenvalues plots [Figs. 5.4(a) and 5.4(b)] are the same as in the DMD algorithm [Figs. 5.3(a) and 5.3(b)] whereas the "field profile" of the aDMD modes [Figs. 5.4(c)-5.4(f)] carry some temporal evolution information. In particular, we observe in Figs. 5.4(c) and 5.4(d) the static behaviours of the aDMD mode with $\omega_i = 0$. On the other hand, we can see, in Figs. 5.4(e) and 5.4(f), one of the first aDMD modes with $\omega_i \neq 0$ featuring some oscillating behaviour in time. The size of the basis mode is larger than the plain DMD, and can exhibit its time evolution. Nevertheless, the graphs do not exactly plot the temporal evolution of the DMD modes since the first N_s entry of the basis state is for the N_s sites; the next N_s for again the N_s sites but at the next time step, etc.

A last improvement of the DMD method would be to circumvent the restriction of the maximum number of DMD modes [130]. The maximum number of DMD modes is indeed restricted by $N = \min(N_s, N_t)$, which may be too few to capture the dynamics of some non-linear regimes. The work-around is to augment the data matrix by stacking the data matrices with N_h version of

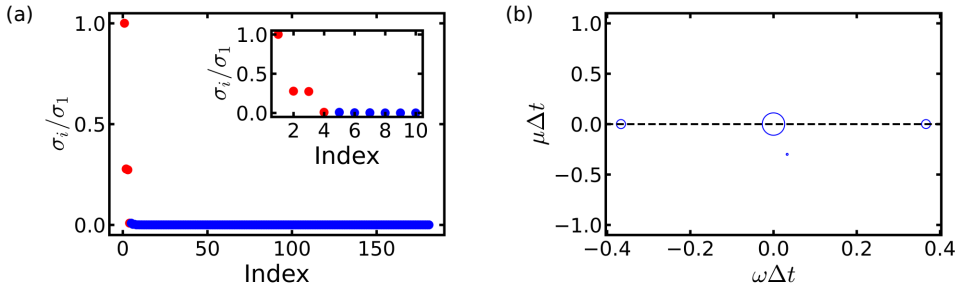

Figure 5.5: (a) Singular values of the oscillating regime in the hDMD. The inset is a zoom-in on the plot. The red dots correspond to the singular values cumulating 99% of the total variance of the data. (b) Plots of the logarithm of hDMD values $\ln(\lambda)$ in the complex plane. The size of the open circle is proportional to their corresponding singular values. The hDMD basis has been generated with $N_h = 19$ from the time series starting at the 1800-th time step.

itself but shifted one time step ahead in time:

$$X_{1,\text{Hankel}} = \begin{bmatrix} x(t_1) & x(t_2) & \cdots & x(t_{N_t-N_h}) \\ x(t_2) & x(t_3) & \cdots & x(t_{N_t-N_h+1}) \\ \vdots & \vdots & \vdots & \vdots \\ x(t_{N_h}) & x(t_{N_h+1}) & \cdots & x(t_{N_t-1}) \end{bmatrix} \tag{5.23}$$

and

$$X_{2,\text{Hankel}} = \begin{bmatrix} x(t_2) & x(t_3) & \cdots & x(t_{N_t-N_h+1}) \\ x(t_3) & x(t_4) & \cdots & x(t_{N_t-N_h+2}) \\ \vdots & \vdots & \vdots & \vdots \\ x(t_{N_h+1}) & x(t_{N_h+2}) & \cdots & x(t_{N_t}) \end{bmatrix}. \tag{5.24}$$

The subscript "Hankel", in the shift-stacking-augmented data matrices, stems for its inspiration from the Hankel matrix [138]. This data-augmented decomposition, denoted by hDMD, proceeds similarly to the DMD method by looking at the following eigenvalues problem:

$$X_{2,\text{Hankel}} = AX_{1,\text{Hankel}}. \tag{5.25}$$

The hDMD modes are then usually taken to be the first N_h entries of the eigenvector of data-augmented matrix A. Likewise, the time-augmentation of

the hDMD basis proceeds as in the aDMD method. Nevertheless, here we will not consider this method, *i.e.* $N_h = 1$, since the rank of the matrix is high enough for the dynamics of interest in this chapter.

Figure 5.5 depicts the hDMD results for the oscillating regime for $N_h = 19$. We can see that the number of singular modes, hence the number of hDMD modes, has indeed increased. The decomposition has also become more accurate. This is seen by observing, for example, that the two hDMD modes, contributing to the oscillating behaviour, have now almost equal contributions in the plot of the singular values. We also observe that a fourth hDMD mode, close to zero frequency $\omega_i \approx 0$, is present but with a decay rate $\mu_i < 0$. Nevertheless, this hDMD mode has negligible contribution to the dynamics as its variance σ_i is small compared to the other hDMD modes.

5.3.3 Classification strategy

We will use the terminology frequently employed in the literature and refer to the N_s-vector column $x(t_i)$ as the state measured at snapshot t_i. Sparse sensing is often desirable since the measurement and the data collection can be expensive for a complex system if the space grid is too fine, *i.e.* if N_s is very large. The compressed measurement $y(t)$ is derived from the full-state measurement $x(t)$ and the measurement matrix C:

$$y(t) = Cx(t), \tag{5.26}$$

where C is a matrix of size $(N_p \times N_s)$ with N_p the number of measurements. Although the measurement matrix C can be represented by some advance and complex mapping [139], here we focus on point-wise measurements, namely the C_{ij} entry in the matrix measurement corresponds to the i-th measurement at the j-th spatial grid point. Therefore the compressed basis is given by:

$$\Theta = C\Phi \tag{5.27}$$

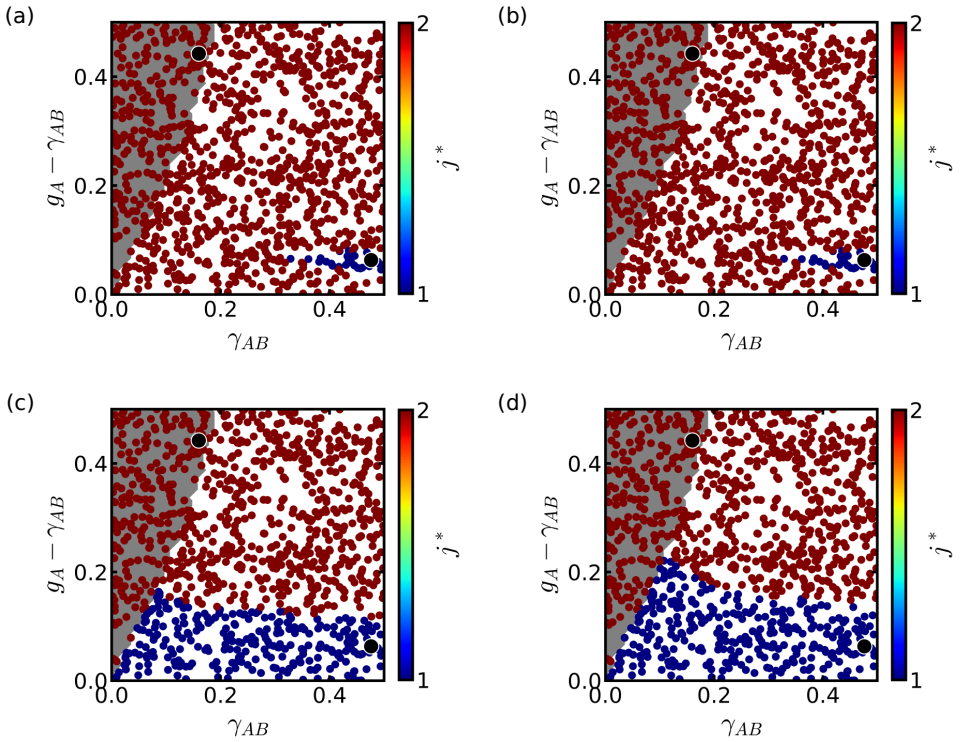

Figure 5.6: Phase diagram obtained from the library composed of two regimes (one non-oscillating and one oscillating), represented by the black dots, from which the bases have been generated using different decomposition methods: (a) POD, (b) DMD, (c) aDMD with $N_w = 5$, (d) aDMD with $N_w = 25$. The grey and white areas are overlays of the referenced phase diagram obtained in Fig. 5.1. The bases have been generated from the time series starting at the 1800-th time step.

where Φ is the basis obtained from the full-state data collection. The library of bases for the J distinct dynamical regimes is similarly re-written as:

$$\mathcal{L} = \{\Theta_1, \ldots, \Theta_J\}. \tag{5.28}$$

Nevertheless, the size of the current SSH lattice is, here, reasonable and allows us to choose the matrix measurement as the identity matrix $C = 1_{N_s}$. We will thus use the full-state instead of sparse measurements, but retain the Θ and $y(t)$ notations to keep the general formalism.

The classification scheme used here has been proposed in Ref. [132], and is based on a simple hierarchical strategy. The regime classification approach is fundamentally a subspace identification problem, where each regime is rep-

resented by a different subspace. Given the measurement $y(t_i)$ at time t_i, the correct regime j^* is identified as the corresponding subspace in the library $\mathcal{L}$ closest to the measurements in the $L2$-norm sense [132]:

$$j^* = \arg \min_{j=1,\dots,J} \left\{ \min_{\beta_j} \|y(t_i) - \Theta_j \beta_j(t_i)\|_2 \right\} \tag{5.29}$$

where the $L2$-norm $\|\cdot\|_2$ of a vector v is given by:

$$\|v\|_2 = \sqrt{\sum_i |v_i|^2}. \tag{5.30}$$

Therefore, the classification algorithm identifies the best matching between the compressed linear combinations $\Theta_j \beta_j$ and the measurement $y(t_i)$. In other words, the classification strategy is to find the subspace that maximises the projection of the measurement onto the regime subspace:

$$j^* = \arg \max_{j=1,\dots,J} \|P_j y(t_i)\|_2, \tag{5.31}$$

where the projection operator P_j is given by:

$$P_j = \Theta_j \Theta_j^+ \tag{5.32}$$

with Θ_j^+ being the pseudo-inverse of Θ_j. Compared to the single snapshot classification scheme, the multiple snapshot classification scheme uses the time-augmented bases and is written as:

$$j^* = \arg \max_{j=1,\dots,J} \|P_j y(t_i : t_{i+N_w})\|_2. \tag{5.33}$$

Figure 5.6 displays the phase diagram obtained from the different decomposition methods reviewed in the previous section. The colours in the plots represent the identified regime j^* [Eq. 5.31] of each sample depicted by the dots in the parameter space. The grey and white areas are overlays of the referenced phase diagram obtained in Fig. 5.1. We observe in Figs. 5.6(a) and 5.6(b) that the phase diagrams fail to correctly predict the distinct dynamical regimes. This is expected since the POD or DMD modes do not contain enough information about the temporal behaviours. Besides, the classification

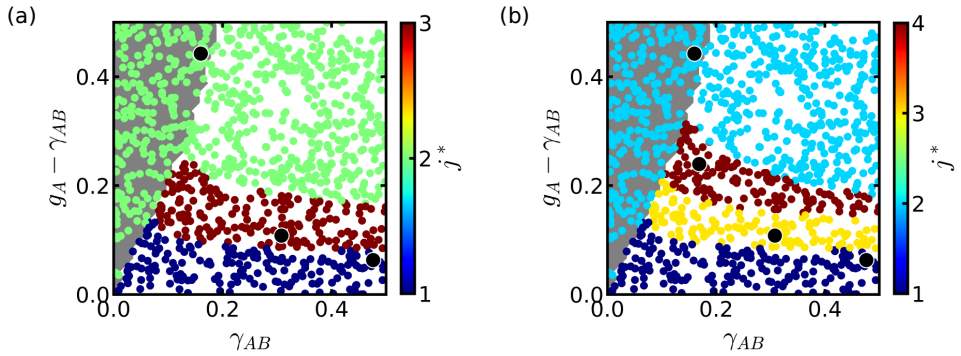

Figure 5.7: Phase diagram obtained from the library composed of (a) three regimes (two non-oscillating and one oscillating) and (b) four regimes (three non-oscillating and one oscillating), represented by the black dots, from which the bases have been generated using the aDMD with $N_w = 25$. The grey and white areas are overlays of the referenced phase diagram obtained in Fig. 5.1. The bases have been generated from the time series starting at the 1800-th time step.

for these diagrams is based on a single snapshot. Thus, it is expected the classification fails to capture the correct dynamics since a single snapshot only relies on the spatial pattern of the regime. On the other hand, we can see in Figs. 5.6(c) and 5.6(d) that the derived phase diagrams have better accuracy when the bases are time-augmented, or equivalently when the classification scheme uses several snapshots. By increasing the time window in the classification, the derived phase diagram is even better as illustrated in Figs. 5.6(c) and 5.6(d) for $N_w = 5$ and $N_w = 25$, respectively. The phase diagram will get improved until the time window is large enough to capture the dynamic behaviour.

Nevertheless, we can see that the phase diagrams, obtained from the aDMD, still fail to correctly predict all the dynamical behaviours [Fig. 5.1]. We observe that many times series are not correctly identified. Yet, using three bases in the library instead of two bases, or equivalent considering three regimes from the given parameter space, Fig. 5.7(a) shows better results. Similarly, four bases in the library [Fig. 5.7(b)] gives slightly better classifications. Therefore, Figure 5.7 reveals that increasing the number of bases in the library $\mathcal{L}$ might help to get closer to the desired phase diagram, though they belong to a distinct regime index j^*.

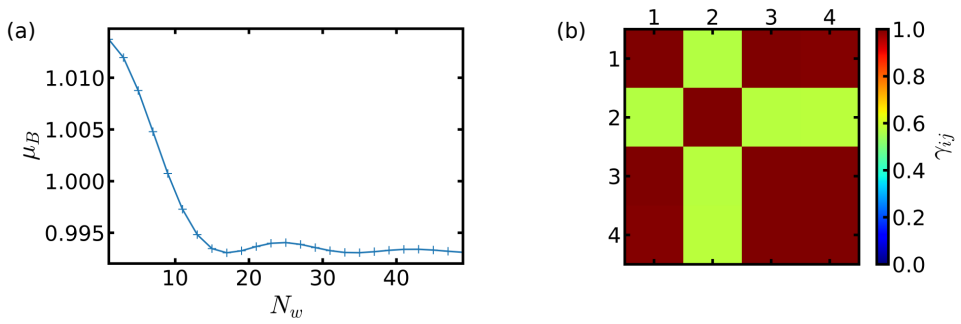

Figure 5.8: (a) Block coherence μ_B against the time window N_w used for generating the aDMD bases. (b) Subspace alignment matrix γ_{ij} for the library composed of four regimes used in Fig. 5.7(b). The bases have been generated from the time series starting at the 1800-th time step.

5.3.4 Classification performance

The classification strategy used here relies on the assumption that each basis in the library $\mathcal{L}$, *i.e.* each representative of the dynamical regimes, spans sufficiently dissimilar subspaces. This means that the projection of the measurement onto one subspace's regime would need to be high enough for the corresponding regime and low enough for another regime. Therefore the accuracy of the classification depends crucially on choosing the correct subspaces and library samples.

To quantify this statement, we can look at how good is a given constructed library for the classification purpose by means of the block coherence of the library. The block coherence μ_B of a library is defined as:

$$\mu_B := \max_{\substack{i,j=1,\dots,J \\ i\neq j}} \frac{1}{r_i} \|\Theta_i^\dagger \Theta_j\|_2 \tag{5.34}$$

where the $L2$-norm $\|\cdot\|_2$ of a matrix M corresponds to its largest singular value:

$$\|M\|_2 = \sqrt{\lambda_{\max}(M^\dagger M)} \tag{5.35}$$

with $\lambda_{\max}(Q)$ being the highest eigenvalues of the matrix Q. Intuitively, μ_B gives the maximum correlation between the eigenvectors in regime i and j, *i.e.* between the subspaces of different regimes. Hence a low μ_B is desirable for better dissimilarity in the subspaces and thus a better classification using the given library. Figure 5.8(a) shows the block coherence of a library composed

of two regimes [Fig. 5.6] against the time window used in the generated time-augmented bases in aDMD. This is consistent with the derived phase diagram shown in Figs. 5.6(b) and 5.6(c) from which the coherence among the regimes is globally decreasing when increasing the time window in aDMD. This shows and quantifies the advantage of using a larger time window for the generation of the bases.

To get more insight into the subspaces of the different regimes, we can also look at their subspace alignment [132]:

$$\gamma_{ij} := \frac{\|P_i P_j\|_F^2}{\|P_i\|_F \|P_j\|_F} \tag{5.36}$$

where the Frobenius norm $\|\cdot\|_F$ of a matrix M is given by:

$$\|M\|_F = \sqrt{\sum_{i,j} |m_{ij}|^2}. \tag{5.37}$$

γ_{ij} indicates the fraction of information that is conserved after projecting the regime j onto the subspace of the regime i. By definition, the γ_{ij} matrix is symmetric and the entries lie in $[0, 1]$ thanks to the normalisation denominator. Figure 5.8(b) plots the γ_{ij} matrix for the library composed of four regimes, as in Fig. 5.7(b). As expected from the known phase diagram, we can see that the three different phases that are located in the non-oscillating region have high projection values onto each other. This is consistent with the fact that they all belong to the same non-oscillating regime and suggests the possibility to construct an adaptive library to fully apprehend the dynamical phase diagram in an automatic way, as we will see in the next section.

5.4 Automatic library construction

So far, the construction of the library $\mathcal{L}$ was a manual process from which we already know the different dynamical regimes. This, however, requires an expertise of the complex system considered. The strategy, here, is to adaptively construct the library based on the given data samples. Two approaches are suggested to achieve this goal. A top-down approach is presented from which we start with too many samples used for the construction of the library, and

then reduce the library size by merging some of them. On the opposite, a bottom-up approach is proposed where we start with only a few samples in the library, and then add samples on the fly if the library is not good enough. Based on some measures in the decision process, this automated construction of the library thus removes the manual construction of the regimes.

5.4.1 Top-down approach

The underlying assumption of the classification scheme is based on the dissimilarity between the subspace of different regimes. We thus propose to consider regimes that are similar as equivalent regimes. This would, for instance, help us to merge the three phases in the non-oscillating region in Fig. 5.7(b), and consider them as a single regime. In other words, the regimes i and j are said to be equivalent, denoted by $i \sim j$, if the fraction of information retained after the projection onto each other is high enough:

$$\gamma_{ij} > \gamma_{th}, \tag{5.38}$$

where $\gamma_{th} \in [0, 1]$ is the hyper-parameter which decides the threshold value for merging different regimes. Importantly, the relation Eq. 5.38 is numerically computed in such a way that the transitivity property of the relation is satisfied, namely that if $i \sim j$ and $j \sim k$ then $i \sim k$. The relation Eq. 5.38 is therefore an equivalence relation since the reflexive ($i \sim i$) and symmetric ($i \sim j \Rightarrow j \sim i$) property of the relation is automatically satisfied from the definition of γ_{ij} [Eq. 5.36].

One should that, compared to standard clustering algorithm which use some metrics to cluster the samples based on some features, the clustering algorithm proposed here simply build, effectively, a connectivity graph from which the number of components of the obtained graph gives us the number of clusters or phases. However, it would be interesting, as a future work, to build upon the distance between regimes defined as γ_{ij} to use in conjunction with standard clustering algorithm such as k-means clustering, spectral clustering, hierarchical clustering, etc [140].

We have seen in Sect. 5.3.3 that the phase diagram was not correctly de-

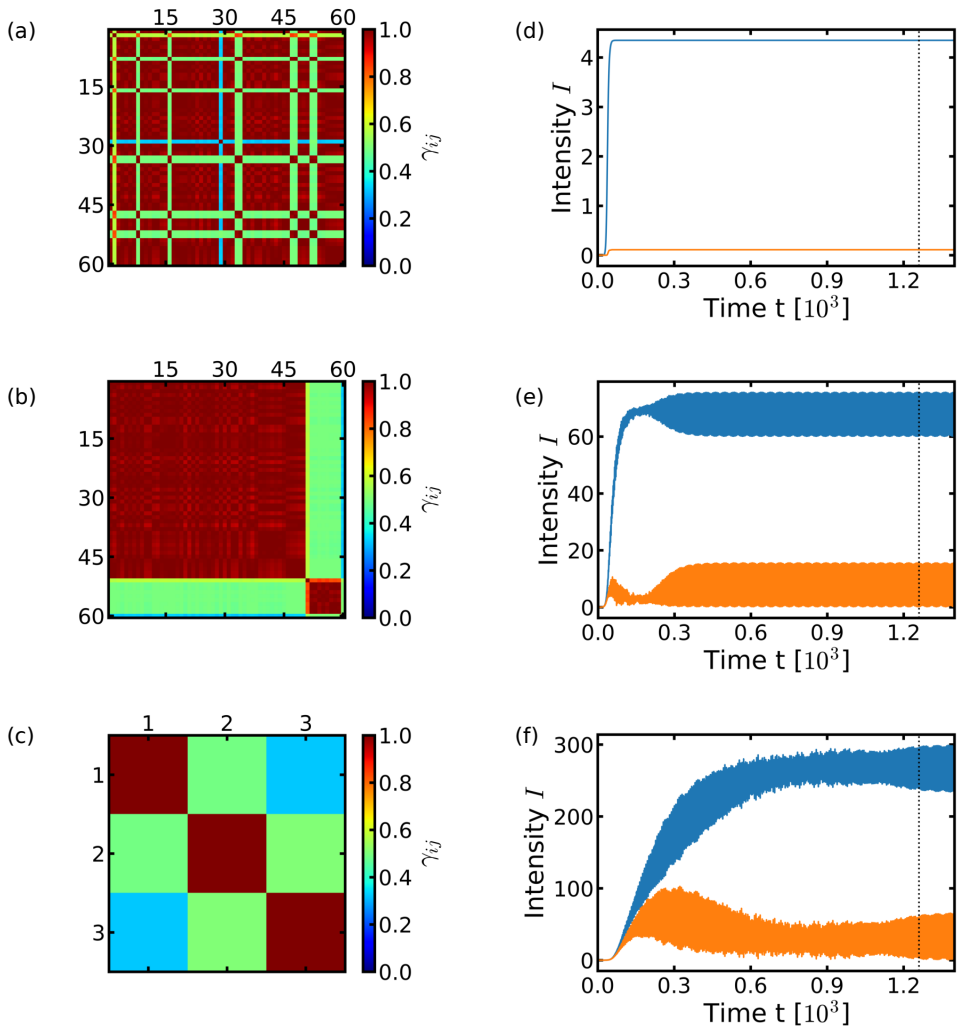

Figure 5.9: (a) Subspace alignment matrix for the initial library composed of $J = 60$ regimes. (b) Subspace alignment matrix from the same library as in (a), grouped into equivalent regimes. (c) Subspace alignment matrix from the reduced library after the equivalent regimes are merged with $\gamma_{th} = 0.75$ in (b). (d)-(f) Total intensity $I_A = \sum_n |a_n|^2$ (and $I_B = \sum_n |b_n|^2$) on the A (and B) sublattice in blue (and orange) for a representative of the first, second and third regime, respectively. The black vertical dotted line indicates the starting time from which the bases are generated. The aDMD bases have been generated with $N_w = 25$ from the time series starting at the 1800-th time step.

rived for two regimes, as well as with four regimes. Therefore, the general idea of the top-down construction of the library is to start with a library made of a high number of bases generated from the time series randomly chosen in the given parameter space region, and then merge them into groups of equivalent regimes. Figure 5.9 illustrates the top-down algorithm. Starting with a library

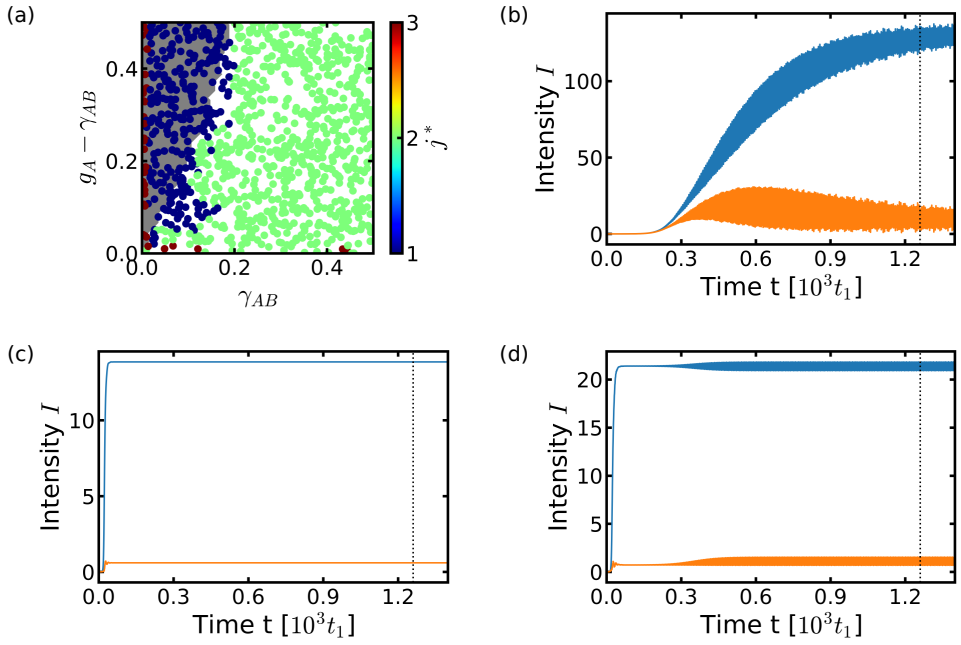

Figure 5.10: (a) Phase diagram obtained using the top-down classification strategy with an initial library composed of $J = 60$ regimes randomly chosen and $\gamma_{th} = 0.75$. The grey and white areas are overlays of the referenced phase diagram obtained in Fig. 5.1. (b)-(d) Total intensity $I_A = \sum_n |a_n|^2$ (and $I_B = \sum_n |b_n|^2$) on the A (and B) sublattice in blue (and orange) for a representative of the transient, non-oscillating and oscillating regime, respectively. The black vertical dotted line indicates the starting time from which the bases are generated. The aDMD bases have been generated with $N_w = 25$ from the time series starting at the 1800-th time step.

composed of $J = 60$ bases, the subspace alignment γ_{ij} is computed [Fig. 5.9(a)] and then grouped into equivalent regimes according to Eq. 5.38 [Fig. 5.9(b)]. Each representative of the regimes is then randomly selected within each group [Fig. 5.9(c)]. We observe in Figs. 5.9(d)-5.9(f) the time series of the representative of each regime. These regimes are the oscillating and non-oscillating regimes, as well as a third regime which may correspond to a transient regime. The vertical dashed line in the time series represents the initial time used for constructing the bases in the library. For convenience, we have plotted only the total intensity on the A ($I_A = \sum_n |a_n|^2$) and B ($I_B = \sum_n |b_n|^2$) sublattices to represent the given regime. Nevertheless, the complex amplitudes at each site are chosen as "observables". We can see that the information measured is not the same compared to the total intensity where, for instance, the relative phase information between sites is lost.

The top-down-based representation classification strategy is to classify the times series according to a large library of bases, and only then merge the equivalent identified regimes via the calculated alignment subspace γ_{ij} and the equivalence relation Eq. 5.38. Figure 5.10 shows the phase diagram obtained from the top-down algorithm started with a library composed of $J = 60$ regimes randomly chosen, along with the representative of each phase. We observe in Fig. 5.10(a) that the derived phase diagram is able to distinguish the non-oscillating [Fig. 5.10(c)] and oscillating regimes [Fig. 5.10(d)]. In addition, a third regime corresponding to a transient regime [Fig. 5.10(b)] is found close to the $\gamma_{AB} = 0$ or $g_A - \gamma_{AB} = 0$ axis. This transient regime indicates that a longer final time in the simulations might be needed to be considered either in the oscillating or non-oscillating regimes.

However, we can see that the derived phase diagram is still failing in the low γ_{AB} and low $g_A - \gamma_{AB}$ region, where some time series are interpreted as oscillating instead of non-oscillating regime. This shows the limitation of this method where the initially constructed library may lack some of the paths that may connect similar bases. For example, regimes i and k might not be similar enough to be considered as equivalent directly [Eq. 5.38] but are both equivalent to the regime j, *i.e.* $i \sim j$ and $j \sim k$, which is missing in the library. The natural workaround would be to increase the initial library size and be sure that the regimes in the library have no missing paths, as we will see in the next section.

The hyper-parameter γ_{th} is an important quantity in the algorithm since it dictates which regimes are equivalent or not. A low threshold γ_{th} will easily merge regimes while a high γ_{th} will barely reduce the size of the library as depicted in Fig. 5.11(a). The threshold is here arbitrarily chosen based on Fig. 5.11, and based on the refinement of the desired library. For example, we can see in Fig. 5.11(b) that the derived phase diagram with $\gamma_{th} = 0.75$ has three different phases corresponding to the oscillating, non-oscillating and transient phases. The distinct regimes are separately plotted in Fig. 5.11(c) for a better visualisation of the regimes' location. On the other hand, with the same library as in Fig. 5.11(b), Figure 5.11(d) displays the obtained phase diagram for a finer threshold value $\gamma_{th} = 0.95$. The plot shows that the algorithm

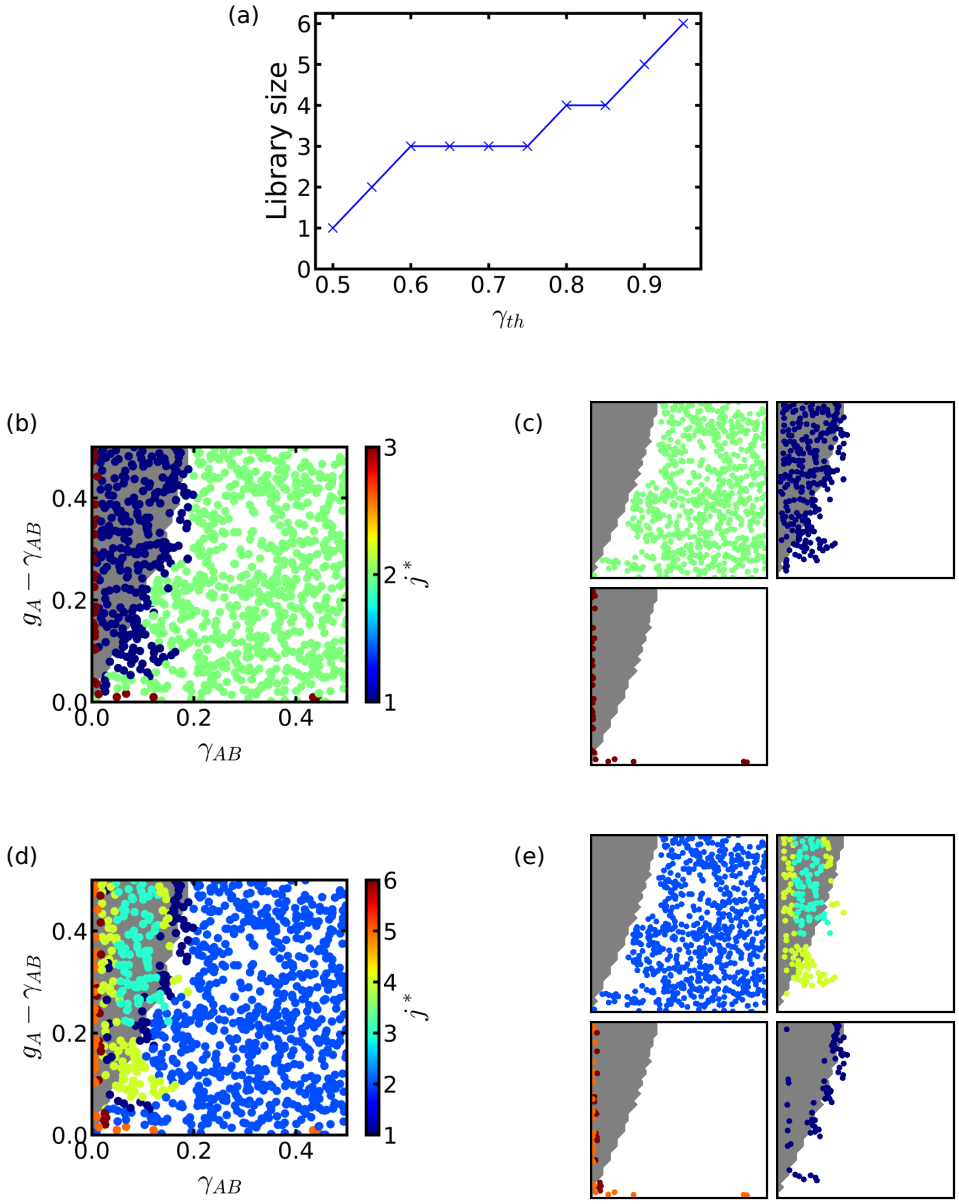

Figure 5.11: (a) Library size against γ_{th}. (b),(c) Phase diagram derived using the top-down classification strategy with $\gamma_{th} = 0.75$, and the location of the regimes in the parameter space. Similarly for (d),(e) but with $\gamma_{th} = 0.95$. The grey and white areas are overlays of the referenced phase diagram obtained in Fig. 5.1. The initial library is composed of $J = 60$ regimes randomly chosen. The aDMD bases have been generated with $N_w = 25$ from the time series starting at the 1800-th time step.

separates the parameter space into several regimes which can be grouped into four main regimes, as displayed in Fig. 5.11(e). In addition to the oscillating, the non-oscillating and the transient regimes that remain present, there is a regime corresponding to the transition between the two topological phases. Besides, this finer description allows us to see distinct sets of modes in the oscillating parameter space region [top-right plot in Fig. 5.11(e)]. The analysis of these distinct oscillating regimes found from the data-driven classification is interesting and is left for a future study. Nevertheless, we observe again that the initial library misclassify some of the non-oscillating time series most likely because of some missing paths, as said previously.

5.4.2 Bottom-up approach

The dual approach, suggested here, is to consider fewer samples in the library. The core idea of the bottom-up approach is then to add samples on the fly during the classification of the samples if the library is not good enough. Here, the library is considered to be good enough if the maximal projection of the measurement onto the regimes' subspace is high enough. In other words, we can look at the worst relative reconstruction error of the library given by:

$$\epsilon := \max_{j=1,\dots,J} \frac{\|P_j y(t) - y(t)\|_2}{\|y(t)\|_2}, \tag{5.39}$$

and say that the library is good enough if the worst relative reconstruction error is low enough:

$$\epsilon < \epsilon_{th}, \tag{5.40}$$

where ϵ_{th} is the hyper-parameter which decides the threshold quality of the library.

Figure 5.12 illustrates the bottom-up methodology proposed. We start with a single sample in the library, randomly chosen in the parameter space region [Fig. 5.12(a)]. The library is then adaptively constructed according to the relative reconstruction error ϵ [Fig. 5.12(b)]. Finally, with the large library at hand, the top-down approach is used to reduce the library size by merging equivalent regimes [Fig. 5.12(c)]. The representative of the regimes is plotted in Figs. 5.12(d)-5.12(f) and corresponds to the non-oscillating, oscillating and

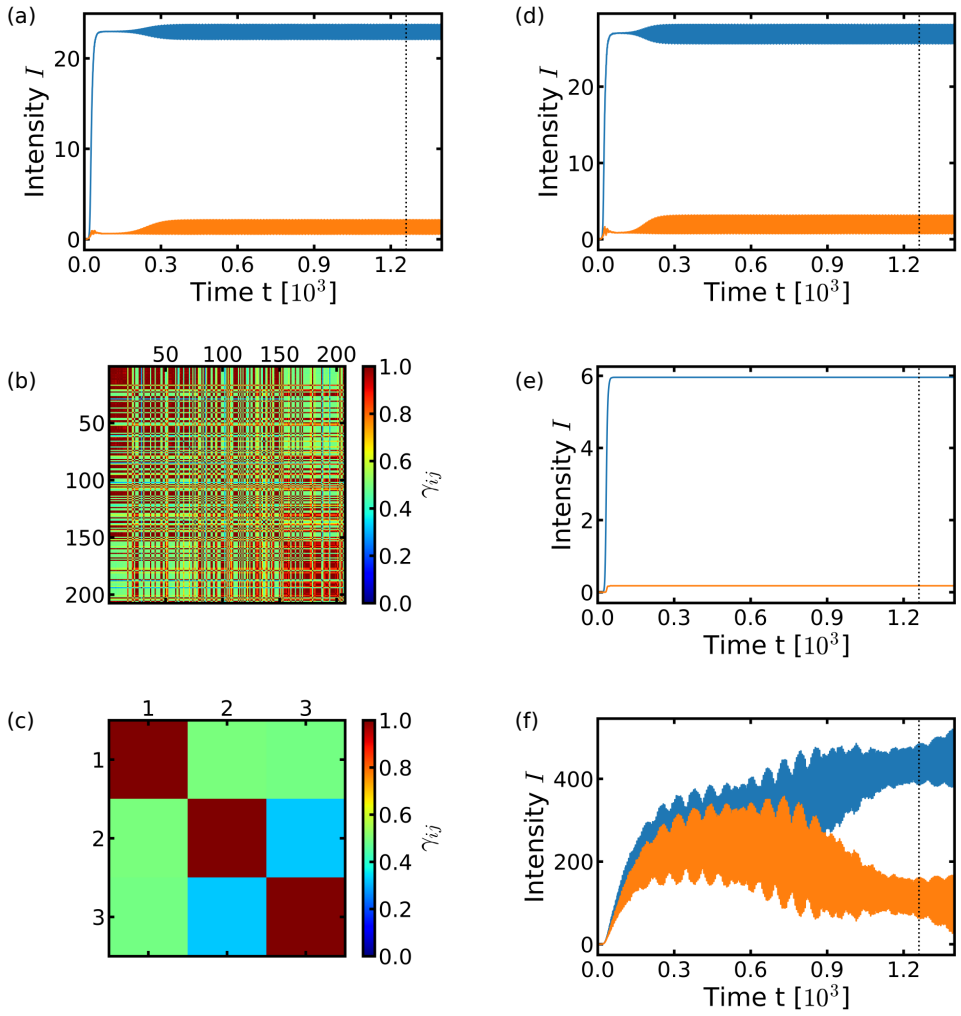

Figure 5.12: (a) Total intensity $I_A = \sum_n |a_n|^2$ (and $I_B = \sum_n |b_n|^2$) on the A (and B) sublattice in blue (and orange) for a single regime in the library. (b) Subspace alignment matrix from the adaptively constructed library with the single initial regime in (a) and with $\epsilon_{th} = 0.01$. (c) Subspace alignment matrix from the reduced library after the equivalent regimes are merged with $\gamma_{th} = 0.75$ in (b). (d)-(f) Total intensity on the A (and B) sublattice in blue (and orange) for a representative of the first, second and third regime. The black vertical dotted line in (a) and (d)-(f) indicates the starting time from which the bases are generated. The aDMD bases have been generated with $N_w = 25$ from the time series starting at the 1800-th time step.

transient regimes, respectively. The advantage of this bottom-up approach is the full exploration of the parameter space region and the automatic construction of a library based on its quality. This method does not suffer from the randomly chosen samples used to construct the library, and the library composition is not restricted to a narrow parameter space region. Using a good enough library quality, the algorithm should therefore be able to sort the

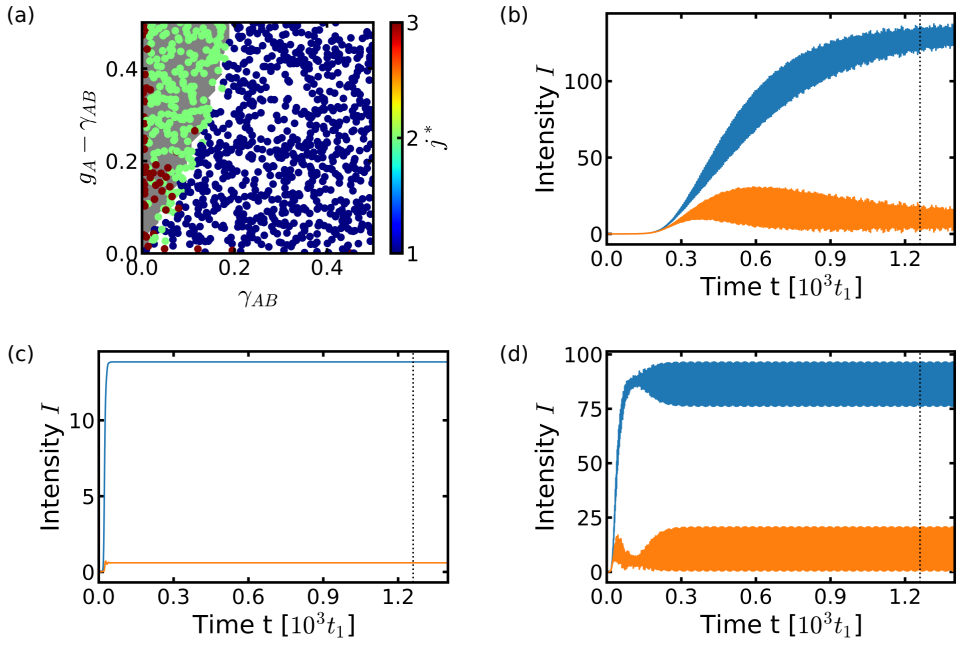

Figure 5.13: (a) Phase diagram obtained using the bottom-up classification strategy with a starting library composed of a single regime randomly chosen, $\epsilon_{th} = 0.005$ and $\gamma_{th} = 0.75$. The grey and white areas are overlays of the referenced phase diagram obtained in Fig. 5.1. (b)-(d) Total intensity $I_A = \sum_n |a_n|^2$ (and $I_B = \sum_n |b_n|^2$) on the A (and B) sublattice in blue (and orange) for a representative of the transient, non-oscillating and oscillating regime, respectively. The black vertical dotted line indicates the starting time from which the bases are generated. The aDMD bases have been generated with $N_w = 25$ from the time series starting at the 1800-th time step.

missing paths issue in the top-down method.

The bottom-up-based representation classification scheme consists of classifying the time series according to a given library or adding this sample into the library if the library is not good enough, and only then merging the different phases obtained into groups of equivalent regimes using the top-down method. Figure 5.13 depicts the phase diagram derived from the bottom-up classification algorithm with a starting library composed of a single regime. Similarly to the top-down approach in Fig. 5.10(a), we observe three distinct regimes corresponding to the non-oscillating, oscillating and transient regimes [Figs. 5.10(b)-5.10(d)]. Nevertheless, the obtained phase diagram now correctly predicts the regimes. We do not have misclassifications of oscillating and non-oscillating regimes which were due to missing paths in the library. Likewise, the transient points are indications of longer simulations needed be-

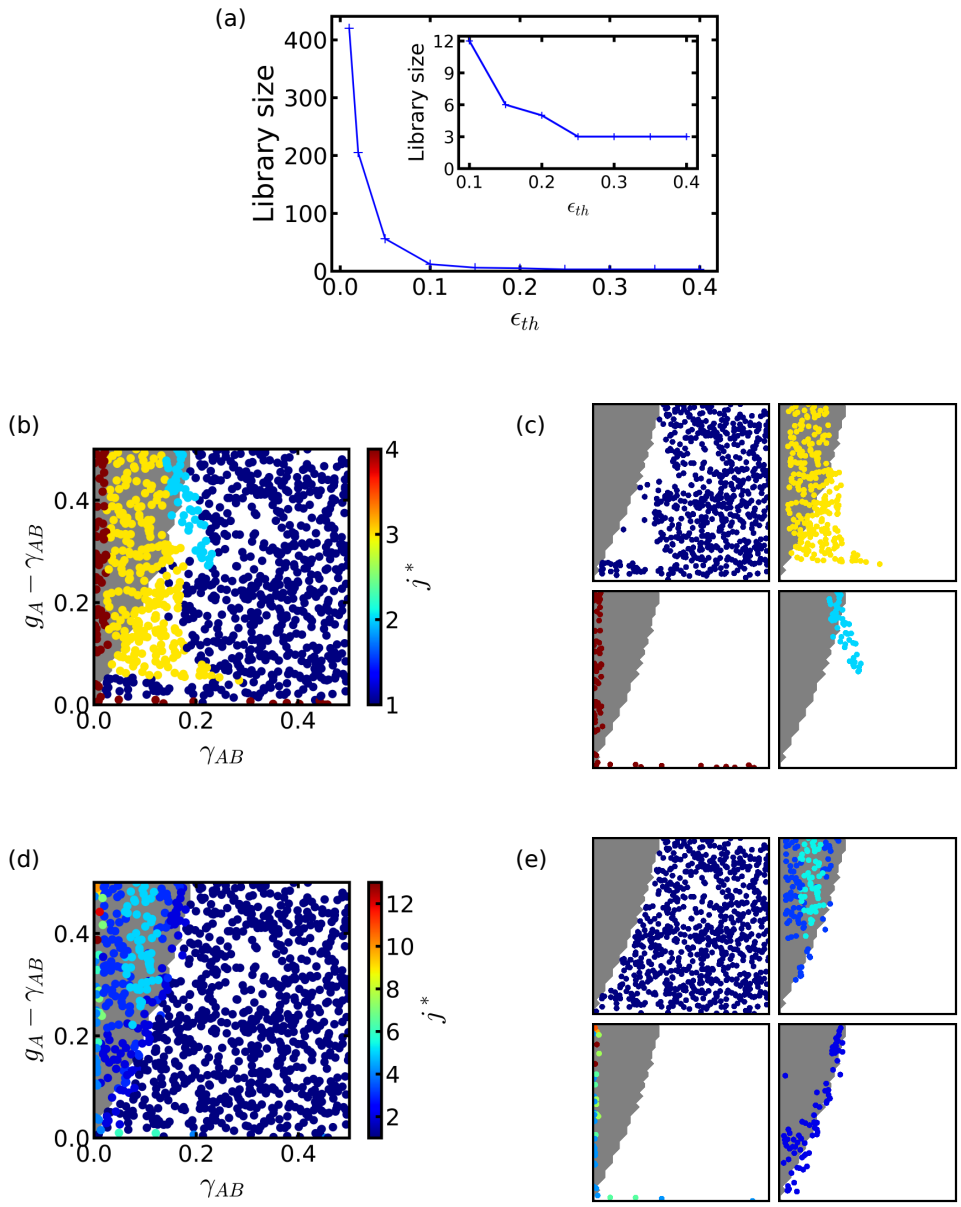

Figure 5.14: (a) Library size against ϵ_{th}. The inset is a zoom-in of the plot. (b),(c) Phase diagram derived using the bottom-up classification strategy with $\epsilon_{th} = 0.01$ and $\gamma_{th} = 0.95$, and the location of the regimes obtained in the parameter space. Similarly for (d),(e) but with $\epsilon_{th} = 0.005$. The grey and white areas are overlays of the referenced phase diagram obtained in Fig. 5.1. The initial library is composed of a single regime randomly chosen. The aDMD bases have been generated with $N_w = 25$ from the time series starting at the 1800-th time step.

cause of the long transient time.

Along with the γ_{th} hyper-parameter, the threshold hyper-parameter ϵ_{th} is an important parameter since it tells us whether we want to add or not a given sample into the library. We observe in Fig. 5.14 that a low threshold ϵ_{th} will

add many samples to the library, whereas a high ϵ_{th} will not add samples to the library at all. The threshold value ϵ_{th} is, again, arbitrarily chosen but with a preference for a high-quality library, *i.e.* low ϵ_{th}, in order to avoid missing paths. For example, we can see in Fig. 5.14(b) the phase diagram derived using $\epsilon_{th} = 0.01$ (and $\gamma_{th} = 0.95$), namely with a library that gives less than 1% of the reconstruction error of the measurement. Figure 5.14(c) displays the four main regimes that seem to correspond to the oscillating, non-oscillating, transition and transient regimes. Yet, there is some misidentification of the two topological phases most likely because of the missing paths of the obtained library. On the other hand, with a better library quality, here $\epsilon_{th} = 0.005$, the missing paths are retrieved and the derived phase diagram correctly predicts the topological phases [Fig. 5.14(d)]. Figure 5.14(e) shows that the different regimes obtained previously with a lower library quality are now better defined. The non-oscillating and oscillating regimes are well located in their respective parameter space region, and the transition points follow the transition boundary between the two topological phases. In addition, the bottom-up-based representation classification is predicting distinct oscillating modes [top-right plot in Fig. 5.14(e)]. Even though the characterisation of these modes is left for a future study, this is an example of new insights given by the data-driven classification method.

5.5 Summary

In summary, we have proposed a data-driven approach in order to explore the dynamics of the topological phases. As an example, we have considered the domain-wall-type SSH lattice with saturable gain from which the results are known. We have utilised the representation classification strategy, based on the aDMD, in order to identify the different topological lasing phases in the parameter space region. Moreover, we proposed an automatic library construction scheme in order to lift the manual labelling requirement. Both top-down and bottom-up approaches have been suggested to merge similar phases in the library or adaptively construct the library based on its quality, respectively. Even though the bottom-up method is desired due to the missing paths issue,

both methods give us the possibility to explore the parameter space without any expert knowledge of the complex non-linear system. This method also provides new insights into the dynamics of the topological lasing mode in the parameter space by a careful examination of the derived phase diagrams. Via reverse engineering, this can be used as a tool to find novel topological lasing modes in more complicated settings. Given the rate equations of a lasing system, such as the kagome lattice in the previous chapter, one would only need to integrate the differential equations in the desired parameter space region and then apply the bottom-up representation classification strategy based on an optimal decomposition method and with a starting library composed of a single chosen regime. Scanning over the hyper-parameters ϵ_{th} and γ_{th} might help finding the optimal values needed for the correct classifications.

Conclusions and future directions

In this thesis, we have explored and studied several designs of topological insulator lasers for improving existing laser devices.

We started, in Chap. 2, with a simple design to achieve topological edge states in an all-dielectric kagome lattice compatible with the current semiconductor technology. Facilitated by the obtained optical valley Hall effect, we have demonstrated broadband suppressed reflection in the presence of sharp corners and shown negligible vertical losses in a semiconductor-based device at telecommunication wavelengths.

In Chap. 3, we proposed an all-dielectric topological laser cavity working in the telecommunication wavelength region based on semiconductor cavities formed by topologically distinct kagome photonic crystals. One of the main advantages of this topological cavity, compared to standard cavities, is its robustness against fabrication defects or bendings. Interestingly, we have shown the topological cavity made of kagome lattices features the coexistence of topological ring-resonator modes and trivial Fabry–Pérot resonator modes. The simplicity of the proposed kagome-lattice-based device and its all-dielectric nature provide a new route to develop integrated topological systems for robust light generation and transport.

From the interplay between non-Hermiticity and PTIs, we have been able to design a topologically robust and temporally stable broad-area, phase-locked laser in a kagome lattice in the rhombus geometry in Chap. 4. The laser, made of a ring-resonator array, is shown to be robust against perturbation thanks to the topological protection of the lasing modes, as well as temporally stable owing to the imaginary gauge field. We believe that our work will provide a new route for achieving robust, stable and high-power

lasers.

Finally, in Chap. 5, we have proposed a data-driven tool in order to further explore new topological lasing modes. These topological lasing modes have no counterpart in the linear-Hermitian setting and are described by different dynamics. The bottom-up representation classification strategy suggested has been proven successful in finding the two topological lasing modes on the toy model given by the SSH lattice with saturable gain.

Several future research directions can be built upon the results presented in this thesis.

Indeed, for the topological cavity laser, the analysis can be carried out further to achieve lasing of only one of the two counter-propagating topological edge mode, from a uniform pumping configuration from above. The parameter space can be explored to find a regime where bifurcations happen and spontaneous symmetry-breakings occur. One of the two counter-propagating mode would then be favoured because of a better mode overlapping with the gain. Lasing of a single topological edge mode might also be achieved when only part of the system is pumped.

Concerning the topological bulk laser, the carrier dynamics can be introduced for the lossy rings as well as for the auxiliary rings that modelled the imaginary gauge field. In addition, the work realised on the topological bulk lasing mode made of ring resonator array can be continued by simulated full-wave simulations thus bridging the gap between the theoretical results and possible experimental implementations. The lattice and material configurations are also not limited to those studied in this thesis. Furthermore, the scope of this novel topologically protected mode is not limited to ring resonator arrays, and metamaterials with smaller scales as well as electronic circuits equivalent can be considered, for instance. Lastly, it might be interesting to consider "topological bulk moving modes", which are the equivalent of the delocalised corner modes but for the topological moving modes.

On the other hand, the data-driven classification tool developed in Chap. 5 was only shown for demonstrative purposes, and can be used to study general non-linear and non-Hermitian PTIs. For instance, the distinct oscillating

modes obtained in the SSH lattice with saturable gain can be characterised. Besides, one can go further in the lattice model by considering the laser rate equation with the carrier dynamics instead of the saturable gain. The tool can also be used for exploring the parameter space of the topological bulk lasing mode obtained in the kagome lattice to get more refined phase diagrams, or to study systems with the Kerr non-linear effect, etc. Furthermore, the decomposition method and/or observables used can be tailored for a suitable need with respect to the system's pattern. The clustering algorithm proposed can also be extended to use standard clustering methods such as k-means clustering, spectral clustering, hierarchical clustering, etc. Complementary to the data-driven classification approach, the interplay between the topologically protected modes and the non-linear modes can be analysed via numerical continuations of the fixed points [141]. Bifurcation behaviours can then be uncovered as in Ref. [142].

Bibliography

[1] J. D. Joannopoulos, S. G. Johnson, J. N. Winn, and R. D. Meade, *Photonic crystals: Molding the flow of light.* Princeton University Press, 2011.

[2] F. D. M. Haldane and S. Raghu, "Possible realization of directional optical waveguides in photonic crystals with broken time-reversal symmetry," *Phys. Rev. Lett.*, vol. 100, no. 1, p. 013904, 2008.

[3] L. Lu, J. D. Joannopoulos, and M. Soljačić, "Topological photonics," *Nat. Photonics*, vol. 8, no. 11, pp. 821–829, 2014.

[4] T. Ozawa, H. M. Price, A. Amo, N. Goldman, M. Hafezi, L. Lu, M. C. Rechtsman, D. Schuster, J. Simon, O. Zilberberg, and I. Carusotto, "Topological photonics," *Rev. Mod. Phys.*, vol. 91, no. 1, p. 015006, 2019.

[5] C.-K. Chiu, J. C. Teo, A. P. Schnyder, and S. Ryu, "Classification of topological quantum matter with symmetries," *Rev. Mod. Phys.*, vol. 88, no. 3, p. 035005, 2016.

[6] Z. Wang, Y. Chong, J. D. Joannopoulos, and M. Soljačić, "Observation of unidirectional backscattering-immune topological electromagnetic states," *Nature*, vol. 461, no. 7265, pp. 772–775, 2009.

[7] M. C. Rechtsman, J. M. Zeuner, Y. Plotnik, Y. Lumer, D. Podolsky, F. Dreisow, S. Nolte, M. Segev, and A. Szameit, "Photonic Floquet topological insulators," *Nature*, vol. 496, no. 7444, pp. 196–200, 2013.

[8] M. Hafezi, S. Mittal, J. Fan, A. Migdall, and J. M. Taylor, "Imaging topological edge states in silicon photonics," *Nat. Photonics*, vol. 7, no. 12, pp. 1001–1005, 2013.

[9] S. Mittal, J. Fan, S. Faez, A. Migdall, J. M. Taylor, and M. Hafezi, "Topologically robust transport of photons in a synthetic gauge field," *Phys. Rev. Lett.*, vol. 113, no. 8, p. 087403, 2014.

[10] R. O. Umucalılar and I. Carusotto, "Artificial gauge field for photons in coupled cavity arrays," *Phys. Rev. A*, vol. 84, no. 4, p. 043804, 2011.

[11] L.-H. Wu and X. Hu, "Scheme for achieving a topological photonic crystal by using dielectric material," *Phys. Rev. Lett.*, vol. 114, no. 22, p. 223901, 2015.

[12] S. Peng, N. J. Schilder, X. Ni, J. van de Groep, M. L. Brongersma, A. Alù, A. B. Khanikaev, H. A. Atwater, and A. Polman, "Probing the band structure of topological silicon photonic lattices in the visible spectrum," *Phys. Rev. Lett.*, vol. 122, no. 11, p. 117401, 2019.

[13] Y. Yang, Y. F. Xu, T. Xu, H.-X. Wang, J.-H. Jiang, X. Hu, and Z. H. Hang, "Visualization of a unidirectional electromagnetic waveguide using topological photonic crystals made of dielectric materials," *Phys. Rev. Lett.*, vol. 120, no. 21, p. 217401, 2018.

[14] S. Barik, A. Karasahin, C. Flower, T. Cai, H. Miyake, W. DeGottardi, M. Hafezi, and E. Waks, "A topological quantum optics interface," *Science*, vol. 359, no. 6376, pp. 666–668, 2018.

[15] M. A. Gorlach, X. Ni, D. A. Smirnova, D. Korobkin, D. Zhirihin, A. P. Slobozhanyuk, P. A. Belov, A. Alù, and A. B. Khanikaev, "Far-field probing of leaky topological states in all-dielectric metasurfaces," *Nat. Commun.*, vol. 9, no. 1, p. 909, 2018.

[16] M. Jalali Mehrabad, A. P. Foster, R. Dost, E. Clarke, P. K. Patil, I. Farrer, J. Heffernan, M. S. Skolnick, and L. R. Wilson, "A semiconductor topological photonic ring resonator," *Appl. Phys. Lett.*, vol. 116, no. 6, p. 061102, 2020.

[17] T. Ma and G. Shvets, "All-Si valley-Hall photonic topological insulator," *New J. Phys.*, vol. 18, no. 2, p. 025012, 2016.

[18] J.-W. Dong, X.-D. Chen, H. Zhu, Y. Wang, and X. Zhang, "Valley photonic crystals for control of spin and topology," *Nat. Mater.*, vol. 16, no. 3, pp. 298–302, 2017.

[19] X.-D. Chen, F.-L. Zhao, M. Chen, and J.-W. Dong, "Valley-contrasting physics in all-dielectric photonic crystals: Orbital angular momentum and topological propagation," *Phys. Rev. B*, vol. 96, no. 2, p. 020202, 2017.

[20] F. Gao, H. Xue, Z. Yang, K. Lai, Y. Yu, X. Lin, Y. Chong, G. Shvets, and B. Zhang, "Topologically protected refraction of robust kink states in valley photonic crystals," *Nat. Phys.*, vol. 14, no. 2, pp. 140–144, 2018.

[21] X. Wu, Y. Meng, J. Tian, Y. Huang, H. Xiang, D. Han, and W. Wen, "Direct observation of valley-polarized topological edge states in designer surface plasmon crystals," *Nat. Commun.*, vol. 8, no. 1, p. 1304, 2017.

[22] J. Noh, S. Huang, K. P. Chen, and M. C. Rechtsman, "Observation of photonic topological valley Hall edge states," *Phys. Rev. Lett.*, vol. 120, no. 6, p. 063902, 2018.

[23] Y. Kang, X. Ni, X. Cheng, A. B. Khanikaev, and A. Z. Genack, "Pseudo-spin–valley coupled edge states in a photonic topological insulator," *Nat. Commun.*, vol. 9, no. 1, p. 3029, 2018.

[24] M. I. Shalaev, W. Walasik, A. Tsukernik, Y. Xu, and N. M. Litchinitser, "Robust topologically protected transport in photonic crystals at telecommunication wavelengths," *Nat. Nanotechnol.*, vol. 14, no. 1, pp. 31–34, 2019.

[25] X.-T. He, E.-t. Liang, J.-j. Yuan, H.-Y. Qiu, X.-d. Chen, F.-L. Zhao, and J.-W. Dong, "A silicon-on-insulator slab for topological valley transport," *Nat. Commun.*, vol. 10, no. 1, p. 872, 2019.

[26] W.-M. Deng, X.-D. Chen, W.-J. Chen, F.-L. Zhao, and J.-W. Dong, "Vortex index identification and unidirectional propagation in kagome photonic crystals," *Nanophotonics*, vol. 8, no. 5, pp. 833–840, 2019.

[27] Y. Xiong, "Why does bulk boundary correspondence fail in some non-Hermitian topological models," *J. Phys. Commun.*, vol. 2, no. 3, p. 035043, 2018.

[28] K. Kawabata, K. Shiozaki, M. Ueda, and M. Sato, "Symmetry and topology in non-Hermitian physics," *Phys. Rev. X*, vol. 9, no. 4, p. 041015, 2019.

[29] D. Leykam, K. Y. Bliokh, C. Huang, Y. D. Chong, and F. Nori, "Edge modes, degeneracies, and topological numbers in non-Hermitian systems," *Phys. Rev. Lett.*, vol. 118, no. 4, pp. 28–30, 2017.

[30] S. Lieu, "Topological phases in the non-Hermitian Su-Schrieffer-Heeger model," *Phys. Rev. B*, vol. 97, no. 4, p. 045106, 2018.

[31] B. Bahari, A. Ndao, F. Vallini, A. El Amili, Y. Fainman, and B. Kanté, "Nonreciprocal lasing in topological cavities of arbitrary geometries," *Science*, vol. 358, no. 6363, pp. 636–640, 2017.

[32] W. P. Su, J. R. Schrieffer, and A. J. Heeger, "Solitons in polyacetylene," *Phys. Rev. Lett.*, vol. 42, no. 25, pp. 1698–1701, 1979.

[33] H. Schomerus, "Topologically protected midgap states in complex photonic lattices," *Opt. Lett.*, vol. 38, no. 11, p. 1912, 2013.

[34] M. Parto, S. Wittek, H. Hodaei, G. Harari, M. A. Bandres, J. Ren, M. C. Rechtsman, M. Segev, D. N. Christodoulides, and M. Khajavikhan, "Edge-mode lasing in 1D topological active arrays," *Phys. Rev. Lett.*, vol. 120, no. 11, p. 113901, 2018.

[35] H. Zhao, P. Miao, M. H. Teimourpour, S. Malzard, R. El-Ganainy, H. Schomerus, and L. Feng, "Topological hybrid silicon microlasers," *Nat. Commun.*, vol. 9, no. 1, p. 981, 2018.

[36] M. A. Bandres, S. Wittek, G. Harari, M. Parto, J. Ren, M. Segev, D. N. Christodoulides, and M. Khajavikhan, "Topological insulator laser: Experiments," *Science*, vol. 359, no. 6381, p. eaar4005, 2018.

[37] G. Harari, M. A. Bandres, Y. Lumer, M. C. Rechtsman, Y. D. Chong, M. Khajavikhan, D. N. Christodoulides, and M. Segev, "Topological insulator laser: Theory," *Science*, vol. 359, no. 6381, p. eaar4003, 2018.

[38] Z.-K. Shao, H.-Z. Chen, S. Wang, X.-R. Mao, Z.-Q. Yang, S.-L. Wang, X.-X. Wang, X. Hu, and R.-M. Ma, "A high-performance topological bulk laser based on band-inversion-induced reflection," *Nat. Nanotechnol.*, vol. 15, no. 1, pp. 67–72, 2020.

[39] S. Longhi, "Non-Hermitian gauged topological laser arrays," *Ann. Phys.*, vol. 530, no. 7, p. 1800023, 2018.

[40] S. Malzard, E. Cancellieri, and H. Schomerus, "Topological dynamics and excitations in lasers and condensates with saturable gain or loss," *Opt. Express*, vol. 26, no. 17, p. 22506, 2018.

[41] S. Malzard and H. Schomerus, "Nonlinear mode competition and symmetry-protected power oscillations in topological lasers," *New J. Phys.*, vol. 20, no. 6, p. 063044, 2018.

[42] S. Longhi, Y. Kominis, and V. Kovanis, "Presence of temporal dynamical instabilities in topological insulator lasers," *EPL*, vol. 122, no. 1, p. 14004, 2018.

[43] H. Araki, T. Mizoguchi, and Y. Hatsugai, "Phase diagram of a disordered higher-order topological insulator: A machine learning study," *Phys. Rev. B*, vol. 99, no. 8, p. 085406, 2019.

[44] P. Zhang, H. Shen, and H. Zhai, "Machine learning topological invariants with neural networks," *Phys. Rev. Lett.*, vol. 120, no. 6, p. 066401, 2018.

[45] V. Peano, F. Sapper, and F. Marquardt, "Rapid exploration of topological band structures using deep learning," *Phys. Rev. X*, vol. 11, no. 2, p. 021052, 2021.

[46] A. P. Schnyder, S. Ryu, A. Furusaki, and A. W. W. Ludwig, "Classification of topological insulators and superconductors in three spatial dimensions," *Phys. Rev. B*, vol. 78, no. 19, p. 195125, 2008.

[47] B. Bradlyn, L. Elcoro, J. Cano, M. G. Vergniory, Z. Wang, C. Felser, M. I. Aroyo, and B. A. Bernevig, "Topological quantum chemistry," *Nature*, vol. 547, no. 7663, pp. 298–305, 2017.

[48] H. C. Po, A. Vishwanath, and H. Watanabe, "Symmetry-based indicators of band topology in the 230 space groups," *Nat. Commun.*, vol. 8, no. 1, p. 50, 2017.

[49] K. Shiozaki, M. Sato, and K. Gomi, "Topological crystalline materials: General formulation, module structure, and wallpaper groups," *Phys. Rev. B*, vol. 95, no. 23, p. 235425, 2017.

[50] A. Yariv, Y. Xu, R. K. Lee, and A. Scherer, "Coupled-resonator optical waveguide: a proposal and analysis," *Opt. Lett.*, vol. 24, no. 11, p. 711, 1999.

[51] J. Poon, J. Scheuer, S. Mookherjea, G. T. Paloczi, Y. Huang, and A. Yariv, "Matrix analysis of microring coupled-resonator optical waveguides," *Opt. Express*, vol. 12, no. 1, p. 90, 2004.

[52] H. G. Winful and L. Rahman, "Synchronized chaos and spatiotemporal chaos in arrays of coupled lasers," *Phys. Rev. Lett.*, vol. 65, no. 13, pp. 1575–1578, 1990.

[53] G. P. Agrawal and N. K. Dutta, *Semiconductor Lasers*. Boston, MA: Springer US, 1995.

[54] C. Henry, "Theory of the linewidth of semiconductor lasers," *IEEE J. Quantum Electron.*, vol. 18, no. 2, pp. 259–264, 1982.

[55] L. Lu, J. D. Joannopoulos, and M. Soljačić, "Topological states in photonic systems," *Nat. Phys.*, vol. 12, no. 7, pp. 626–629, 2016.

[56] Y. Hatsugai, "Chern number and edge states in the integer quantum Hall effect," *Phys. Rev. Lett.*, vol. 71, no. 22, pp. 3697–3700, 1993.

[57] A. B. Khanikaev, S. Hossein Mousavi, W.-K. Tse, M. Kargarian, A. H. MacDonald, and G. Shvets, "Photonic topological insulators," *Nat. Mater.*, vol. 12, no. 3, pp. 233–239, 2013.

[58] M. Hafezi, E. A. Demler, M. D. Lukin, and J. M. Taylor, "Robust optical delay lines with topological protection," *Nat. Phys.*, vol. 7, no. 11, pp. 907–912, 2011.

[59] K. Fang, Z. Yu, and S. Fan, "Realizing effective magnetic field for photons by controlling the phase of dynamic modulation," *Nat. Photonics*, vol. 6, no. 11, pp. 782–787, 2012.

[60] C. L. Kane and E. J. Mele, "Z2 Topological order and the quantum spin Hall effect," *Phys. Rev. Lett.*, vol. 95, no. 14, p. 146802, 2005.

[61] H. Chen, H. Nassar, A. N. Norris, G. K. Hu, and G. L. Huang, "Elastic quantum spin Hall effect in kagome lattices," *Phys. Rev. B*, vol. 98, no. 9, p. 094302, 2018.

[62] M. Saba, S. Wong, M. Elman, S. S. Oh, and O. Hess, "Nature of topological protection in photonic spin and valley Hall insulators," *Phys. Rev. B*, vol. 101, no. 5, p. 054307, 2020.

[63] Y. Kim, K. Choi, J. Ihm, and H. Jin, "Topological domain walls and quantum valley Hall effects in silicene," *Phys. Rev. B*, vol. 89, no. 8, p. 085429, 2014.

[64] O. Bleu, D. D. Solnyshkov, and G. Malpuech, "Quantum valley Hall effect and perfect valley filter based on photonic analogs of transitional metal dichalcogenides," *Phys. Rev. B*, vol. 95, no. 23, p. 235431, 2017.

[65] X.-D. Chen, F.-L. Shi, H. Liu, J.-C. Lu, W.-M. Deng, J.-Y. Dai, Q. Cheng, and J.-W. Dong, "Tunable electromagnetic flow control in valley photonic crystal waveguides," *Phys. Rev. Appl.*, vol. 10, no. 4, p. 044002, 2018.

[66] Z. Gao, Z. Yang, F. Gao, H. Xue, Y. Yang, J. Dong, and B. Zhang, "Valley surface-wave photonic crystal and its bulk/edge transport," *Phys. Rev. B*, vol. 96, no. 20, p. 201402, 2017.

[67] R. K. Pal and M. Ruzzene, "Edge waves in plates with resonators: an elastic analogue of the quantum valley Hall effect," *New J. Phys.*, vol. 19, no. 2, p. 025001, 2017.

[68] T.-W. Liu and F. Semperlotti, "Experimental evidence of robust acoustic valley Hall edge states in a nonresonant topological elastic waveguide," *Phys. Rev. Appl.*, vol. 11, no. 1, p. 014040, 2019.

[69] K. Qian, D. J. Apigo, C. Prodan, Y. Barlas, and E. Prodan, "Topology of the valley-Chern effect," *Phys. Rev. B*, vol. 98, no. 15, p. 155138, 2018.

[70] I. Syozi, "Statistics of kagome lattice," *Prog. Theor. Phys.*, vol. 6, no. 3, pp. 306–308, 1951.

[71] H. Kim, A. C. Farrell, P. Senanayake, W. J. Lee, and D. L. Huffaker, "Monolithically integrated InGaAs nanowires on 3D structured silicon-on-insulator as a new platform for full optical links," *Nano Lett.*, vol. 16, no. 3, pp. 1833–1839, 2016.

[72] S. Johnson and J. Joannopoulos, "Block-iterative frequency-domain methods for Maxwell's equations in a planewave basis," *Opt. Express*, vol. 8, no. 3, p. 173, 2001.

[73] C. J. Bradley and A. P. Cracknell, *The mathematical theory of symmetry in solids : representation theory for point groups and space groups.* Oxford University Press, U.S.A, 2010.

[74] D. J. Thouless, M. Kohmoto, M. P. Nightingale, and M. den Nijs, "Quantized Hall conductance in a two-dimensional periodic potential," *Phys. Rev. Lett.*, vol. 49, no. 6, pp. 405–408, 1982.

[75] H. Xue, Y. Yang, and B. Zhang, "Topological valley photonics: Physics and device applications," *Adv. Photonics Res.*, vol. 2, no. 8, p. 2100013, 2021.

[76] M. V. Berry, "Quantal phase factors accompanying adiabatic changes," *Proc. R. Soc. London. A. Math. Phys. Sci.*, vol. 392, no. 1802, pp. 45–57, 1984.

[77] P. Lodahl, S. Mahmoodian, S. Stobbe, A. Rauschenbeutel, P. Schneeweiss, J. Volz, H. Pichler, and P. Zoller, "Chiral quantum optics," *Nature*, vol. 541, no. 7638, pp. 473–480, 2017.

[78] S. S. Oh, B. Lang, D. M. Beggs, D. L. Huffaker, M. Saba, and O. Hess, "Chiral light-matter interaction in dielectric photonic topological insulators," in *CLEO Pacific Rim Conf.* Washington, D.C.: OSA, 2018, p. Th4H.5.

[79] Oskooi, A. F., E. al., A. F. Oskooi, D. Roundy, M. Ibanescu, P. Bermel, J. D. Joannopoulos, and S. G. Johnson, "meep: A flexible free-software package for electromagnetic simulations by the fdtd method," *Comput. Phys. Commun.*, no. 3, pp. 687–702.

[80] J. Petersen, J. Volz, and A. Rauschenbeutel, "Chiral nanophotonic waveguide interface based on spin-orbit interaction of light," *Science*, vol. 346, no. 6205, pp. 67–71, 2014.

[81] R. J. Coles, D. M. Price, J. E. Dixon, B. Royall, E. Clarke, P. Kok, M. S. Skolnick, A. M. Fox, and M. N. Makhonin, "Chirality of nanophotonic waveguide with embedded quantum emitter for unidirectional spin transfer," *Nat. Commun.*, vol. 7, no. 1, p. 11183, 2016.

[82] Lumerical, https://www.lumerical.com/products/fdtd/.

[83] X. Ni, M. A. Gorlach, A. Alu, and A. B. Khanikaev, "Topological edge states in acoustic kagome lattices," *New J. Phys.*, vol. 19, no. 5, p. 055002, 2017.

[84] H. Zhong, Y. Li, D. Song, Y. V. Kartashov, Y. Zhang, Y. Zhang, and Z. Chen, "Topological valley Hall edge state lasing," *Laser Photon. Rev.*, vol. 14, no. 7, p. 2000001, 2020.

[85] S. Kruk, A. Poddubny, D. Smirnova, L. Wang, A. Slobozhanyuk, A. Shorokhov, I. Kravchenko, B. Luther-Davies, and Y. Kivshar, "Nonlinear light generation in topological nanostructures," *Nat. Nanotechnol.*, vol. 14, no. 2, pp. 126–130, 2019.

[86] H. Zhao, X. Qiao, T. Wu, B. Midya, S. Longhi, and L. Feng, "Non-Hermitian topological light steering," *Science*, vol. 365, no. 6458, pp. 1163–1166, 2019.

[87] X. Cheng, C. Jouvaud, X. Ni, S. H. Mousavi, A. Z. Genack, and A. B. Khanikaev, "Robust reconfigurable electromagnetic pathways within a photonic topological insulator," *Nat. Mater.*, vol. 15, no. 5, pp. 542–548, 2016.

[88] P. St-Jean, V. Goblot, E. Galopin, A. Lemaître, T. Ozawa, L. Le Gratiet, I. Sagnes, J. Bloch, and A. Amo, "Lasing in topological edge states of a one-dimensional lattice," *Nat. Photonics*, vol. 11, no. 10, pp. 651–656, 2017.

[89] C. Han, M. Lee, S. Callard, C. Seassal, and H. Jeon, "Lasing at topological edge states in a photonic crystal L3 nanocavity dimer array," *Light Sci. Appl.*, vol. 8, no. 1, p. 40, 2019.

[90] Y. Ota, R. Katsumi, K. Watanabe, S. Iwamoto, and Y. Arakawa, "Topological photonic crystal nanocavity laser," *Commun. Phys.*, vol. 1, no. 1, p. 86, 2018.

[91] Y. Zeng, U. Chattopadhyay, B. Zhu, B. Qiang, J. Li, Y. Jin, L. Li, A. G. Davies, E. H. Linfield, B. Zhang, Y. Chong, and Q. J. Wang, "Electrically pumped topological laser with valley edge modes," *Nature*, vol. 578, no. 7794, pp. 246–250, 2020.

[92] S. Wong, M. Saba, O. Hess, and S. S. Oh, "Gapless unidirectional photonic transport using all-dielectric kagome lattices," *Phys. Rev. Res.*, vol. 2, no. 1, p. 012011, 2020.

[93] X.-C. Sun and X. Hu, "Topological ring-cavity laser formed by honeycomb photonic crystals," *Phys. Rev. B*, vol. 103, no. 24, p. 245305, 2021.

[94] P. Rabiei, W. Steier, Cheng Zhang, and L. Dalton, "Polymer micro-ring filters and modulators," *J. Light. Technol.*, vol. 20, no. 11, pp. 1968–1975, 2002.

[95] A. Griffith, J. Cardenas, C. B. Poitras, and M. Lipson, "High quality factor and high confinement silicon resonators using etchless process," *Opt. Express*, vol. 20, no. 19, p. 21341, 2012.

[96] S.-H. Chang and A. Taflove, "Finite-difference time-domain model of lasing action in a four-level two-electron atomic system," *Opt. Express*, vol. 12, no. 16, p. 3827, 2004.

[97] S. V. Zhukovsky, D. N. Chigrin, A. V. Lavrinenko, and J. Kroha, "Switchable lasing in multimode microcavities," *Phys. Rev. Lett.*, vol. 99, no. 7, p. 073902, 2007.

[98] M. C. Rechtsman, Y. Lumer, Y. Plotnik, A. Perez-Leija, A. Szameit, and M. Segev, "Topological protection of photonic path entanglement," *Optica*, vol. 3, no. 9, p. 925, 2016.

[99] S. Mittal, V. V. Orre, and M. Hafezi, "Topologically robust transport of entangled photons in a 2D photonic system," *Opt. Express*, vol. 24, no. 14, p. 15631, 2016.

[100] T. W. Hughes, M. Minkov, Y. Shi, and S. Fan, "Training of photonic neural networks through in situ backpropagation and gradient measurement," *Optica*, vol. 5, no. 7, p. 864, 2018.

[101] I. Liberal and N. Engheta, "Near-zero refractive index photonics," *Nat. Photonics*, vol. 11, no. 3, pp. 149–158, 2017.

[102] X. Huang, Y. Lai, Z. H. Hang, H. Zheng, and C. T. Chan, "Dirac cones induced by accidental degeneracy in photonic crystals and zero-refractive-index materials," *Nat. Mater.*, vol. 10, no. 8, pp. 582–586, 2011.

[103] M. Saba, J. M. Hamm, J. J. Baumberg, and O. Hess, "Group theoretical route to deterministic Weyl points in chiral photonic lattices," *Phys. Rev. Lett.*, vol. 119, no. 22, p. 227401, 2017.

[104] C. Poli, M. Bellec, U. Kuhl, F. Mortessagne, and H. Schomerus, "Selective enhancement of topologically induced interface states in a dielectric resonator chain," *Nat. Commun.*, vol. 6, no. 1, p. 6710, 2015.

[105] K. Takata and M. Notomi, "Photonic topological insulating phase induced solely by gain and loss," *Phys. Rev. Lett.*, vol. 121, no. 21, p. 213902, 2018.

[106] Y. Gong, S. Wong, A. J. Bennett, D. L. Huffaker, and S. S. Oh, "Topological insulator laser using valley-Hall photonic crystals," *ACS Photonics*, vol. 7, no. 8, pp. 2089–2097, 2020.

[107] S. Bittner, S. Guazzotti, Y. Zeng, X. Hu, H. Yılmaz, K. Kim, S. S. Oh, Q. J. Wang, O. Hess, and H. Cao, "Suppressing spatiotemporal lasing instabilities with wave-chaotic microcavities," *Science*, vol. 361, no. 6408, pp. 1225–1231, 2018.

[108] N. Hatano and D. R. Nelson, "Localization transitions in non-Hermitian quantum mechanics," *Phys. Rev. Lett.*, vol. 77, no. 3, pp. 570–573, 1996.

[109] F. K. Kunst, M. Trescher, and E. J. Bergholtz, "Anatomy of topological surface states: Exact solutions from destructive interference on frustrated lattices," *Phys. Rev. B*, vol. 96, no. 8, p. 085443, 2017.

[110] F. K. Kunst, G. van Miert, and E. J. Bergholtz, "Boundaries of boundaries: A systematic approach to lattice models with solvable boundary states of arbitrary codimension," *Phys. Rev. B*, vol. 99, no. 8, p. 085426, 2019.

[111] S. Mao, Y. Kuramoto, K.-I. Imura, and A. Yamakage, "Analytic theory of edge modes in topological insulators," *J. Phys. Soc. Japan*, vol. 79, no. 12, p. 124709, 2010.

[112] G. van Miert and C. Ortix, "On the topological immunity of corner states in two-dimensional crystalline insulators," *npj Quantum Mater.*, vol. 5, no. 1, p. 63, 2020.

[113] M. Ezawa, "Higher-order topological insulators and semimetals on the breathing kagome and pyrochlore lattices," *Phys. Rev. Lett.*, vol. 120, no. 2, p. 026801, 2018.

[114] A. El Hassan, F. K. Kunst, A. Moritz, G. Andler, E. J. Bergholtz, and M. Bourennane, "Corner states of light in photonic waveguides," *Nat. Photonics*, vol. 13, no. 10, pp. 697–700, 2019.

[115] M. A. J. Herrera, S. N. Kempkes, M. B. de Paz, A. García-Etxarri, I. Swart, C. M. Smith, and D. Bercioux, "Corner modes of the breathing kagome lattice: Origin and robustness," *Phys. Rev. B*, vol. 105, no. 8, p. 085411, 2022.

[116] L. Feng, Z. J. Wong, R.-M. Ma, Y. Wang, and X. Zhang, "Single-mode laser by parity-time symmetry breaking," *Science*, vol. 346, no. 6212, pp. 972–975, 2014.

[117] H. Schomerus, "Nonreciprocal response theory of non-Hermitian mechanical metamaterials: Response phase transition from the skin effect of zero modes," *Phys. Rev. Res.*, vol. 2, no. 1, p. 013058, 2020.

[118] R.-d. Li and T. Erneux, "Preferential instability in arrays of coupled lasers," *Phys. Rev. A*, vol. 46, no. 7, pp. 4252–4260, 1992.

[119] J. Ding, I. Belykh, A. Marandi, and M.-A. Miri, "Dispersive versus dissipative coupling for frequency synchronization in lasers," *Phys. Rev. Appl.*, vol. 12, no. 5, p. 054039, 2019.

[120] C. Poli, H. Schomerus, M. Bellec, U. Kuhl, and F. Mortessagne, "Partial chiral symmetry-breaking as a route to spectrally isolated topological defect states in two-dimensional artificial materials," *2D Mater.*, vol. 4, no. 2, p. 025008, 2017.

[121] F. Liu and K. Wakabayashi, "Novel topological phase with a zero Berry curvature," *Phys. Rev. Lett.*, vol. 118, no. 7, p. 076803, 2017.

[122] S. Longhi, D. Gatti, and G. D. Valle, "Robust light transport in non-Hermitian photonic lattices," *Sci. Rep.*, vol. 5, no. 1, p. 13376, 2015.

[123] L. Wang, "Discovering phase transitions with unsupervised learning," *Phys. Rev. B*, vol. 94, no. 19, p. 195105, 2016.

[124] M. S. Scheurer and R.-J. Slager, "Unsupervised machine learning and band topology," *Phys. Rev. Lett.*, vol. 124, no. 22, p. 226401, 2020.

[125] I. Jolliffe, "Principal component analysis," in *Encycl. Stat. Behav. Sci.* Chichester, UK: John Wiley & Sons, Ltd, 2005.

[126] J. Wright, A. Yang, A. Ganesh, S. Sastry, and Yi Ma, "Robust face recognition via sparse representation," *IEEE Trans. Pattern Anal. Mach. Intell.*, vol. 31, no. 2, pp. 210–227, 2009.

[127] S. L. Brunton, J. H. Tu, I. Bright, and J. N. Kutz, "Compressive sensing and low-rank libraries for classification of bifurcation regimes in nonlinear dynamical systems," *SIAM J. Appl. Dyn. Syst.*, vol. 13, no. 4, pp. 1716–1732, 2014.

[128] J. L. Proctor, S. L. Brunton, B. W. Brunton, and J. N. Kutz, "Exploiting sparsity and equation-free architectures in complex systems," *Eur. Phys. J. Spec. Top.*, vol. 223, no. 13, pp. 2665–2684, 2014.

[129] X. Fu, S. L. Brunton, and J. Nathan Kutz, "Classification of birefringence in mode-locked fiber lasers using machine learning and sparse representation," *Opt. Express*, vol. 22, no. 7, p. 8585, 2014.

[130] B. W. Brunton, L. A. Johnson, J. G. Ojemann, and J. N. Kutz, "Extracting spatial-temporal coherent patterns in large-scale neural recordings using dynamic mode decomposition," *J. Neurosci. Methods*, vol. 258, pp. 1–15, 2016.

[131] I. Bright, G. Lin, and J. N. Kutz, "Classification of spatiotemporal data via asynchronous sparse sampling: Application to flow around a cylinder," *Multiscale Model. Simul.*, vol. 14, no. 2, pp. 823–838, 2016.

[132] B. Kramer, P. Grover, P. Boufounos, S. Nabi, and M. Benosman, "Sparse sensing and dmd-based identification of flow regimes and bifurcations in complex flows," *SIAM J. Appl. Dyn. Syst.*, vol. 16, no. 2, pp. 1164–1196, 2017.

[133] D. E. Ozan, A. Iannelli, M. Yin, and R. S. Smith, "Regularized classification and simulation of bifurcation regimes in nonlinear systems," *IFAC-PapersOnLine*, vol. 54, no. 14, pp. 352–357, 2021.

[134] M. C. Cross and P. C. Hohenberg, "Pattern formation outside of equilibrium," *Rev. Mod. Phys.*, vol. 65, no. 3, pp. 851–1112, 1993.

[135] M. Gavish and D. L. Donoho, "The optimal hard threshold for singular values is $4/\sqrt{3}$," *IEEE Trans. Inf. Theory*, vol. 60, no. 8, pp. 5040–5053, 2014.

[136] P. J. Schmid, "Dynamic mode decomposition of numerical and experimental data," *J. Fluid Mech.*, vol. 656, pp. 5–28, 2010.

[137] J. H. Tu, C. W. Rowley, D. M. Luchtenburg, S. L. Brunton, and J. N. Kutz, "On dynamic mode decomposition: Theory and applications," *J. Comput. Dyn.*, vol. 1, no. 2, pp. 391–421, 2014.

[138] J.-N. Juang and R. S. Pappa, "An eigensystem realization algorithm for modal parameter identification and model reduction," *J. Guid. Control. Dyn.*, vol. 8, no. 5, pp. 620–627, 1985.

[139] E. J. Candès, "Compressive sampling," *Proc. Int. Congr. Math. Madrid*, pp. 1433–1452, 2006.

[140] Fabian Pedregosa, Ga{{\"e}}l Varoquaux, Alexandre Gramfort, Vincent Michel, Bertrand Thirion, Olivier Grisel, Mathieu Blondel, Peter Prettenhofer, Ron Weiss, Vincent Dubourg, Jake Vanderplas, Alexandre Passos, David Cournapeau, Matthieu Brucher, Matthieu Perrot, and {{\'E}}douard Duchesnay, "Scikit-learn: Machine learning in Python," *J. Mach. Learn. Res.*, vol. 12, pp. 2825–2830, 2011.

[141] E. J. Doedel, E. J. Doedel, T. F. Fairgrieve, B. Sandstede, A. R. Champneys, Y. A. Kuznetsov, and X. Wang, *AUTO-07P: Continuation and bifurcation software for ordinary differential equations.* Technical Report, 2007.

[142] T. G. Seidel, A. M. Perego, J. Javaloyes, and S. V. Gurevich, "Discrete light bullets in passively mode-locked semiconductor lasers," *Chaos An Interdiscip. J. Nonlinear Sci.*, vol. 30, no. 6, p. 063102, 2020.